Pericytes in Early Vascular Development

Jordan Alexandra Darden

Dissertation submitted to the faculty of
the Virginia Polytechnic Institute and State University
in partial fulfillment of the requirements for the degree of

Doctor of Philosophy
In
Translational Biology, Medicine, and Health

John C. Chappell, Chair
Sarah McDonald
Harald Sontheimer
Robert Gourdie

March 22, 2019
Roanoke, Virginia

Keywords: vascular development, pericyte recruitment, heterogeneity, developmental pathogenesis

Pericytes in Early Vascular Development

Jordan Alexandra Darden

ACADEMIC ABSTRACT

Blood vessels are critical for the delivery of oxygen and nutrients to all cells in the body. To properly function, blood vessels and their primary components must develop and mature into a healthy network, capable of dynamic alterations to meet new needs of the body. The early genetic and molecular programs that “push” the vasculature to develop are the same programs that reactivate when there are normal changes to the body such as injury, muscle growth or decline, or aging; and when pathologies arise like cancer, stroke, and diabetes. Therefore, it is crucial to understand how the vasculature develops into a healthy system by studying all components as they mature.

Endothelial cells that comprise the vessels themselves are joined by specialized partner cells called pericytes that help guide and mature vessel growth. Pericytes lie elongated along endothelial cells and have multiple points of contact with the endothelium. In this position, pericytes assist in cell-cell communication and even blood flow regulation in the microvasculature. To study the relationship between endothelial cells and pericytes during development, we observed vascular morphology in three and four dimensions, as well as the genetic and molecular mechanisms underlying how these cells are recruited and interact in several experimental models. Thus, to thoroughly analyze the morphology of these vessels, we developed a rigorous methodology using a MATLAB program to determine the colocalization and coverage of pericytes associated with vessels in large image sets. After developing analytical methods to investigate all the components of the

blood vessel wall, we expanded our investigation of how pericytes and other aspects of microvasculature develop in animal models, specifically a more commonly used murine model for vascular development and for treatment of human diseases. Our findings of vascular development in mice suggest that there are important differences in how human and mouse brain blood vessels form. Therefore, studies using mice must be carefully designed to account for these discrepancies. Additionally, research into why human and mouse neurovascular development and maturation are different can aid in the development of improved experimental models to better treat human pathologies.

Pericytes in Early Vascular Development

Jordan Alexandra Darden

GENERAL AUDIENCE ABSTRACT

Blood vessels have the crucial job of delivering oxygen and nutrients to all the cells in the body. To perform this duty, blood vessels- and the components that make them- must develop and mature into a healthy network, capable of altering itself to meet new needs of the body. The early programs that “push” the vessel system to develop are the same programs that reactivate when there are normal changes to the body such as injury, muscle growth or decline, or aging; and when abnormal diseases arise like cancer, stroke, and diabetes. Therefore, it is critical to understand how blood vessels develop into healthy systems by studying all of their components as they mature.

Endothelial cells that comprise the vessels themselves are joined by specialized partner cells called pericytes that help guide and mature vessel growth. Pericytes lie elongated along endothelial cells and have multiple points of contact with the endothelium. In this position, pericytes assist in cell-cell communication and even blood flow regulation in smaller vessels called capillaries. To study the relationship between endothelial cells and pericytes during development, we observed vascular anatomy in three and four dimensions, as well as mechanisms underlying how these cells come together and interact in several experimental models. Thus, to thoroughly analyze the morphology of these vessels, we developed a rigorous methodology using a MATLAB program to determine the colocalization and coverage of pericytes associated with vessels in large image sets. After developing analytical method to investigate all the components of the

blood vessel wall, we expanded our investigation of how pericytes and other aspects of blood vessels develop in animal models, specifically a more commonly used animal model for vascular development and for treatment of human diseases. Our findings of vascular development in mice suggest that there are important differences in how human and mouse brain blood vessels form. Therefore, studies using mice must be carefully designed to account for these discrepancies. Additionally, research into why human and mouse neurovascular development and maturation are different can aid in the development of improved experimental models to better treat human illness and injury.

DEDICATION

I would like to dedicate this dissertation to my family and friends for their unconditional support during this journey. I would also like to dedicate it to my grandfather, Dr. Bruton Darden (*in memoriam*), for inspiring me to embrace my curiosity and learn new things every day.

ACKNOWLEDGEMENTS

The greatest and most heart-felt gratitude to my advisor, mentor, and cheerleader, Dr. John Chappell. You were willing to take a chance on a starry-eyed psychology student that knew nothing of molecular biology. With you, I have learned many lessons, at the bench, and in life. Your optimism and joy for research is truly inspiring. It has been a fun-filled and interesting journey with you, and I am ever so glad you took a chance on me. I would also like to give thanks to all the members of my committee, Dr. Chappell, Dr. Sarah McDonald, Dr. Rob Gourdie, and Dr. Harald Sontheimer, for their expertise, guidance and dedication to my education. I will be forever grateful for the time and challenges you presented to grow as a professional.

I would also like to give a special thanks to my friends and fellow graduate students in TBMH and at the VTCRI. We have supported and encouraged one another over the past five years. Thank you for allowing me to pick your brains and test some of your reagents. The medical students, fellow lab members, and volunteers, working with you has been a pleasure.

This dissertation was supported by the National Institute of Health grant numbers R56HL133826 and R00HL105779**,** as well as the National Science Foundation CAREER Award 1752339. The Translational Biology, Medicine, and Health Graduate Program and the Virginia Tech Carilion Research Institute funds also provided funding for this work.

ATTRIBUTIONS

The work described within this dissertation would not have been possible without help from my colleagues. A list and brief description of their contributions are included below:

Chapter 2 and Appendix

Harsh Patolia was a third year medical student at the Virginia Tech Carilion School of Medicine and is a co-author on this manuscript. We identified the need, developed the concepts, and tested the MATLAB program now used in lab analysis, however none of which would have been possible without Harsh's coding ability (InSite Code in Appendix).

Chapter 3

Clifton Jenkins-Houk was a fourth year medical student at the Virginia Tech Carilion School of Medicine and is a co-author on this manuscript. Cliff assisted in nearly all stages of project development; including data collection, analysis, and manuscript writing.

Chapters 2, 3, & 4

John C. Chappell was an Assistant Professor at the Virginia Tech Fralin Biomedical Research Institute and is the corresponding author on these manuscripts. He contributed to the writing and editing of these manuscripts, as well as assisted in experimental designs and data collection.

TABLE OF CONTENTS

LIST OF FIGURES

INTRODUCTION

Cardiovascular health has emerged as an important issue in today's society given the global trends in poor dietary habits and an increase in sedentary lifestyle. Adverse cardiovascular events (i.e. myocardial infarction and cerebrovascular stroke) persist as the leading causes of death globally for the past 15 years [1]. These traumatic events, as well as other vascular pathologies such as peripheral artery disease, decrease the quality of life for surviving individuals. To develop better therapeutic targets for combatting vascular disease, we must deepen our understanding of how healthy vasculature develops and maintains proper functionality. Complex networks of blood vessels must (i) develop within all tissues and organ systems to sustain life by maintaining blood flow, and (ii) adapt to acute and chronic metabolic and structural changes within various tissues.

To sustain life, blood vessel development must begin in the earliest stages of embryogenesis. As development moves into the maturation stages of adulthood, many mechanisms underlying initial vascular development can re-emerge to enable the vasculature to adapt in response to various pathologies, injuries, and even aging (e.g. hypoxic tissue secretes VEGF-A to initiate new vessel sprouting) [2, 3]. The cardiovascular system is one of the first functional organ systems to develop in vertebrates, as mutations in cardiovascular-related genes often lead to embryonic lethality [4, 5]. In addition to providing essential functions such as oxygen/gas exchange and supplying nutrients, blood vessels provide critical regulation and guidance cues to

support the development of other systems (e.g. nervous system, liver, and pancreas [6-11]).

To sustain the health and homeostasis of these and other developing organ systems, the vasculature develops as a hierarchy of channels to optimize delivery for each level of tissue and cells. The blood vascular system is composed of three main types of vessels: (i) arteries and arterioles, (ii) veins and venules, and (iii) capillaries also referred to as the microvasculature or microcirculation [12, 13]. The vessels themselves are composed of multiple cell types. Endothelial cells compose the innermost lining that interfaces with the blood. Vascular smooth muscle cells (vSMCs) surround larger diameter vessels (i.e. arteries and veins) as well as smaller pre-capillary vessels (i.e. arterioles and venules). Pericytes are specialized perivascular cells that stabilize microvessels and may even regulate blood flow via contractile cues. Vessels also consist of connective tissues including extracellular matrix (ECM) components such as collagens and elastic fibers in the outermost layers and vascular basement membrane [2, 12]. These cells and structures facilitate dynamic changes in vessel diameter and wall composition to meet the metabolic needs of surrounding tissues. In this way, the composition of the vessel wall regulates vascular permeability and overall functionality of microvascular beds. Although the functionality of all vessels is critical for overall health, endothelial cells and pericytes within the microvasculature play uniquely important roles in capillary stabilization, maturation, and function that must be considered when developing new therapeutics.

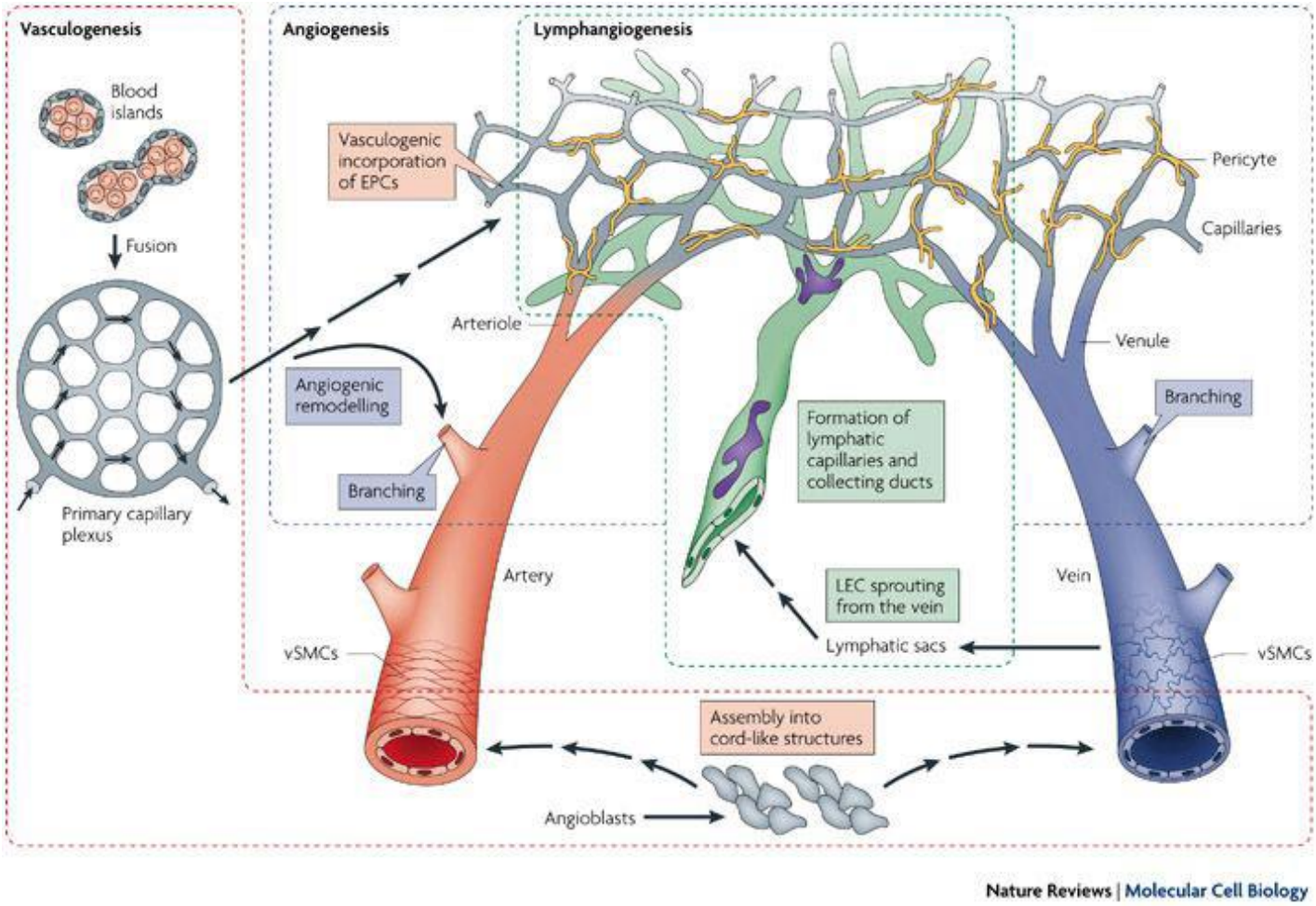

Figure 1: Representative illustration of stages of vascular development. Embryonic mesodermal cells differentiate into endothelial precursor cells (EPCs and angioblasts), that coalesce into blood islands. Fusion of these blood islands form a primitive vascular plexus in the yolk sac and embryo. This primitive plexus is remodeled into a hierarchical network of arteries/ arterioles (red), capillaries (grey), and vein/venules (blue. Vascular smooth muscle cells (vSMCs) encircle higher width vessels, arteries and veins, whereas, pericytes (yellow) cover capillaries. Figure taken from R. Adams and K Alitalo (2007) Molecular regulation of angiogenesis and lymphangiogenesis. *Nature Reviews Molecular Cell Biology* 8:464-478 doi: 10.1038/nm2183 with permission.

Stages of Vascular Development

Development of the microvasculature begins with the initiation and progression of several concurrent morphogenetic programs. The *de novo* formation of primitive vessels occurs through aggregation and organization of newly differentiated endothelial cells, a process known as vasculogenesis [14, 15]. The next phase in vascular development is the formation of new vessels from existing vasculature called angiogenesis [16-18]. Angiogenesis can be divided into two sub-types of remodeling: (1) intussusceptive or splitting angiogenesis whereby larger vessels divide into smaller vessels, and (2) sprouting angiogenesis where a nascent vessel emerges and extends from an existing vessel in response to guidance cues [2]. As a basic vascular network forms, additional remodeling occurs to generate new vessels via sprouting but also to remove unnecessary vessels via regression/rarefaction to “fine-tune” the network [19]. These same programs for vessel remodeling can emerge at different stages in life to adapt to metabolic changes in tissues or to new structural remodeling such as with adipose gain/loss, muscle atrophy/expansion, cyclic programming of the female reproductive system, wound repair, and in pathological conditions such as diabetes, cancer, or hemangiomas [20-30].

As vascular morphogenesis and the remodeling stages of development near completion, blood vessel maturation programs continue to stabilize the network and promote overall tissue homeostasis [31]. This maturation phase, which likely occurs in close succession with vessel formation, includes (i) the recruitment of pericytes within the microvasculature and vSMCs on larger vessels, and (ii) the deposition of ECM components into the vascular basement membrane, forming a selectively permeable yet

exclusive barrier and thus a highly regulated exchange platform [2, 3]. Vasculogenesis, angiogenesis, and vessel maturation are all critical stages for the development, quiescence, and functionality of newly formed vasculature.

Vasculogenesis

Vascular development begins at the earliest stages of embryo development where mesodermal cells differentiate into hemangioblasts, a multipotent precursor cell capable of giving rise to endothelial or hematopoietic cells. These hemangioblasts in turn differentiate into angioblasts, which compose “blood islands”. Vasculogenesis is typically described as the formation of vessels via the cell aggregation into a cord-like structure and tube formation of angioblasts (endothelial precursors), leading to the fusion of blood islands into a primordial vessel network [15, 16]. Vasculogenesis gives rise to a number of vascular beds and larger-diameter vessels including the primordia major blood vessels such as the dorsal aorta from the heart and endocardium [2, 15, 32], as well as the capillary networks found in the amniote yolk sac, which will eventually be remodeled into a more hierarchical and mature vascular network [15, 18, 32]. The earliest blood islands arise from the yolk sac. During gastrulation, undifferentiated hemangioblasts from the blood vessels in the umbilical vesicle, allantois, and chorion coalesce and form a capillary plexus. These plexus vessels will continue to grow and eventually fuse with the simultaneously developing embryo vasculature[33, 34]. The process of vasculogenesis encompasses a finely-coordinated series of steps, including differentiation, migration, adhesion and maturation of

endothelial precursors and blood islands, which together coalesce into a continuous tubular network that will remodel and mature into healthy functional vessels [2, 32, 33].

Angiogenic Vessel Remodeling of the Microvasculature

After the initial phase of vasculogenesis, the primordial network of vessels will need to remodel and mature to perform its critical functions. A key feature of proper vessel formation is the growth of the vasculature into a hierarchical network capable of facilitating oxygen and nutrient delivery to all cells in the body [18]. An essential process for accomplishing this outcome is the formation of new vessels from pre-existing vessels, a phenomenon known as angiogenesis [2, 17]. The two types of angiogenesis, sprouting and splitting, are necessary for the expansion of a viable vessel network. Splitting angiogenesis entails endothelial cells within larger vessels extending their cell wall into the lumen (often called “tissue pillars”) to split the vessel into two, creating a bifurcation [35, 36]. This process involves the structural reorganization of existing endothelial cells but not necessarily their proliferation to increase endothelial cell number [2, 31, 36]. Intussusception, or splitting angiogenesis, is a critical mode of network formation, particularly in early embryonic and extraembryonic tissue development (e.g. in the yolk sac) where cellular resources may be limited for creating an extensive microvascular bed quickly, which would require rapid cell proliferation each time new vessel development is needed.

While intussusception is a documented mode of vascular expansion, sprouting angiogenesis is thought to be the primary method of vessel growth in the developmental context. From vessel networks arising during vasculogenesis, endothelial cells continue

responding to angiogenic stimuli to form new vessels. Dynamic competition among endothelial cells leads to the emergence of a leading cell, or “tip cell” [37, 38]. This “tip cell” sustains communication signals to neighboring endothelial cells to limit the formation of any additional “tip cells” in response to the angiogenic cues [37, 39, 40], as multiple “tip cells” could lead to severe vascular dysmorphogenesis [41, 42]. As the “tip cell” migrates away from the parent vessel, neighboring endothelial cells remain adherent and trail behind it to form a “stalk” portion of the emerging vessel sprout [37, 38]. The stalk cells are thought to proliferate more frequently and rapidly reorganize to maintain the sprouting structure, as the length and caliber of the new vessel continues to expand [43]. Parent vessels are often lumenized, and as the sprout continues to elongate, the stalk acquires a lumen that will eventually connect with that of the parent vessel, ultimately extending toward the new connection point[44-46]{Kamei, 2006 #1813}. The “tip cell” itself does not contain a lumen [2, 40]. Instead active filopodial extensions facilitate efficient guidance of the “tip cell” [38, 43] toward necessary hypoxic/pro-angiogenic areas by sampling the environment for morphogenetic cues to establish a new vessel branch. The “tip cell” will eventually contact a new vessel (either another emerging sprout or a nearby, intact vessel), and cell-cell communication will facilitate fusion of the two structures into a fully connected vessel segment [2]. This nascent vessel may in turn become a parent vessel for additional sprouting events to further enhance the complexity of the target vascular bed.

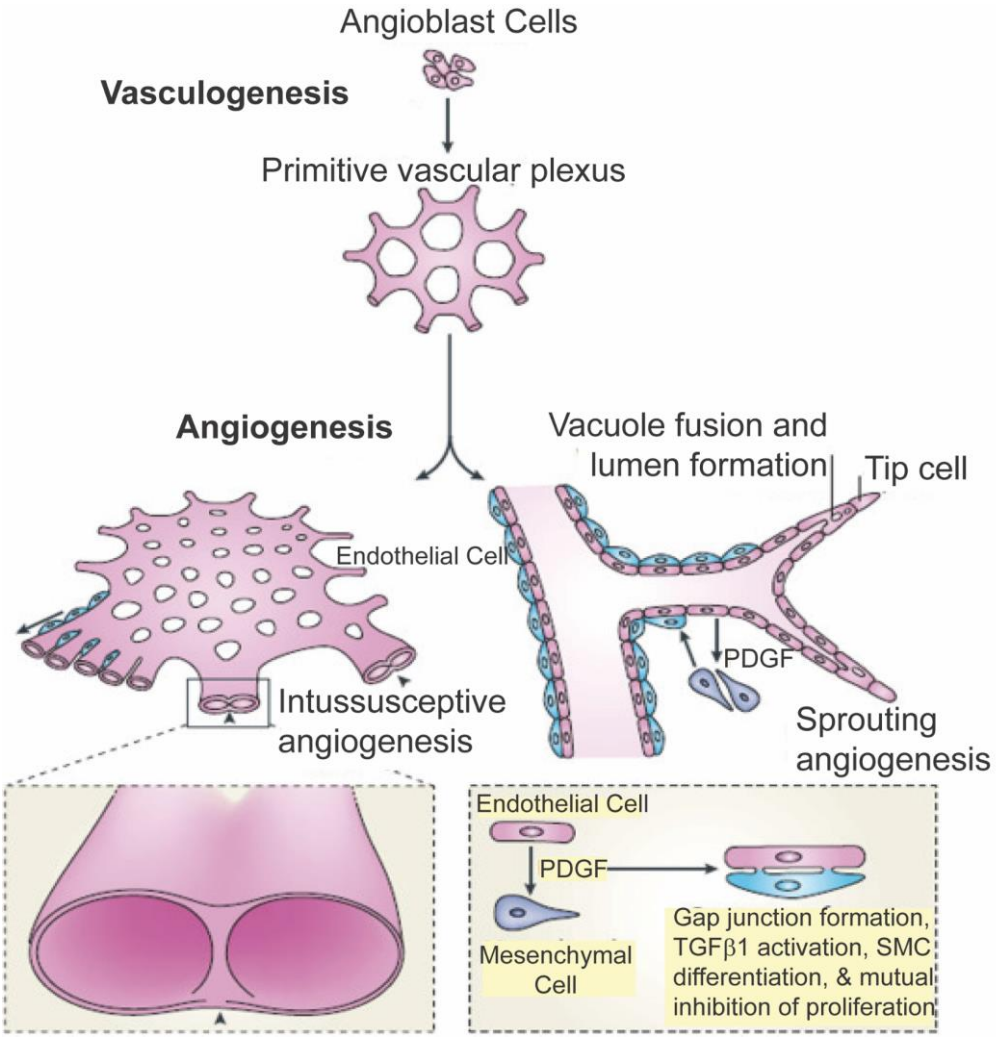

Figure 2: Schematic of vasculogenesis versus angiogenesis. Vessel remodeling is illustrated by two types of angiogenesis; sprouting and intussusceptive. Intussusceptive or splitting angiogenesis occurs when endothelial cells extend into the lumen of a larger diameter vessel, thus creating two smaller, separate vessels. Sprouting angiogenesis occurs when an endothelial tip cell followed by proliferating stalk cells migrate forming a sprouting vessel. This sprout will fuse with another stable vessel or active sprout to form a novel vascular connection. To complete the connection within the network, endothelial vacuoles fuse to form lumens for blood flow. Endothelial cells release multiple signaling ligands to stabilize the vessel, including recruitment of mesenchymal cells or pericytes. Image modified for clarity and size of text with permission from Kolte, D, McClung, J.A. & Aronow, W.S. (2016) Chapter 6- Vasculogenesis and Angiogenesis. Translational Research in Coronary Artery Disease. Boston: Academic Press. http://doi.org/https://doi.org/10.1016/B978-0-12-802385-3.00006-1

Signaling Mechanisms Underlying Endothelial Cell Sprouting

VEGF Signaling

Vessel sprouting occurs when stimuli such as vascular endothelial growth factor (VEGF) ligands bind cognate receptors on endothelial cells within established or newly-formed vessels [37, 38, 43]. The VEGF family of ligands includes five isoforms that can bind distinct receptors and act as agonists; however, we focus on the isoform that is considered the most potent signaling molecule for several vascular remodeling, specifically VEGF-A. VEGF-A binds several receptors on the endothelium including VEGF Receptor 1 [VEGFR1 in humans, or FMS-like tyrosine kinase receptor-1 (Flt-1) in mice] and the primary intracellular signaling receptor, VEGF Receptor-2 [VEGFR2 in humans, or Fetal liver kinase-1 (Flk-1) in mice] [47, 48]. An additional VEGF receptor, VEGF Receptor-3 (VEGFR3), does not bind VEGF-A; instead VEGFR3 binds to VEGF-C and VEGF-D isoforms and primarily mediates formation of the lymphatic vascular system [49, 50]. Vessel sprout initiation begins when VEGF-A secreted from hypoxic cells binds to VEGFR2/Flk-1 on nearby vascular endothelium. Activated endothelial cells establish a “tip cell” to lead the formation of a new vessel, as discussed above [43]. As a “tip cell” engages the surrounding VEGF-A signals and migrates outward from the parent vessel, several downstream signaling pathways are engaged to assist in sustaining and guiding the emergence of this new vessel sprout. One of these guidance cues is VEGFR1/Flt-1 and particularly the soluble form of VEGFR1/Flt-1 (sFlt-1), which acts as a negative regulator of VEGF-A signaling. Soluble VEGFR1/Flt-1 binds VEGF-A ligand to spatially limit its availability for signaling, thereby providing a “braking system” for VEGF-A signaling [42, 51-53]. With increases in both membrane and soluble

isoforms of VEGFR1/Flt-1, oncoming VEGF-A molecules bind to this ligand sink and cannot engage with VEGFR2/Flk-1 receptors [51, 52], which further reinforces phenotypic heterogeneity in endothelial “tip” and “stalk” cells.

NOTCH Signaling

The “tip cell” itself engages in cell-cell signaling with neighboring cells as previously mentioned through lateral inhibition [39, 54]. This lateral inhibition mechanism is critical for the phenotypic heterogeneity in the endothelial cells within an emerging vessel, leading to only one “tip cell” guiding the sprout followed by “stalk cells” that compose and lengthen the elongating sprout. Lateral inhibition is cell-cell contact dependent and determination of endothelial phenotype is achieved in large part through NOTCH signaling. NOTCH is a highly conserved developmental signaling pathway responsible for numerous critical functions in cellular organization throughout the body [54]. This signaling cascade regulates many biological processes in development in which cells [12, 54]. NOTCH signaling within the vascular system, and particularly among endothelial cells, is facilitated primarily by two of the five NOTCH ligands, Delta Like-4 (Dll4), and Jagged-1 (Jag-1) [40, 55, 56]. Briefly, these NOTCH ligands bind to one of two NOTCH transmembrane receptors (Notch1 and Notch4) and initiate proteolytic cleavage and release of the NOTCH intracellular domain (NICD). The NICD translocates to the nucleus, co-activating downstream transcriptional targets such as Hairy/Enhancer of Split (Hes) and Hes-related proteins (Hey) [57].

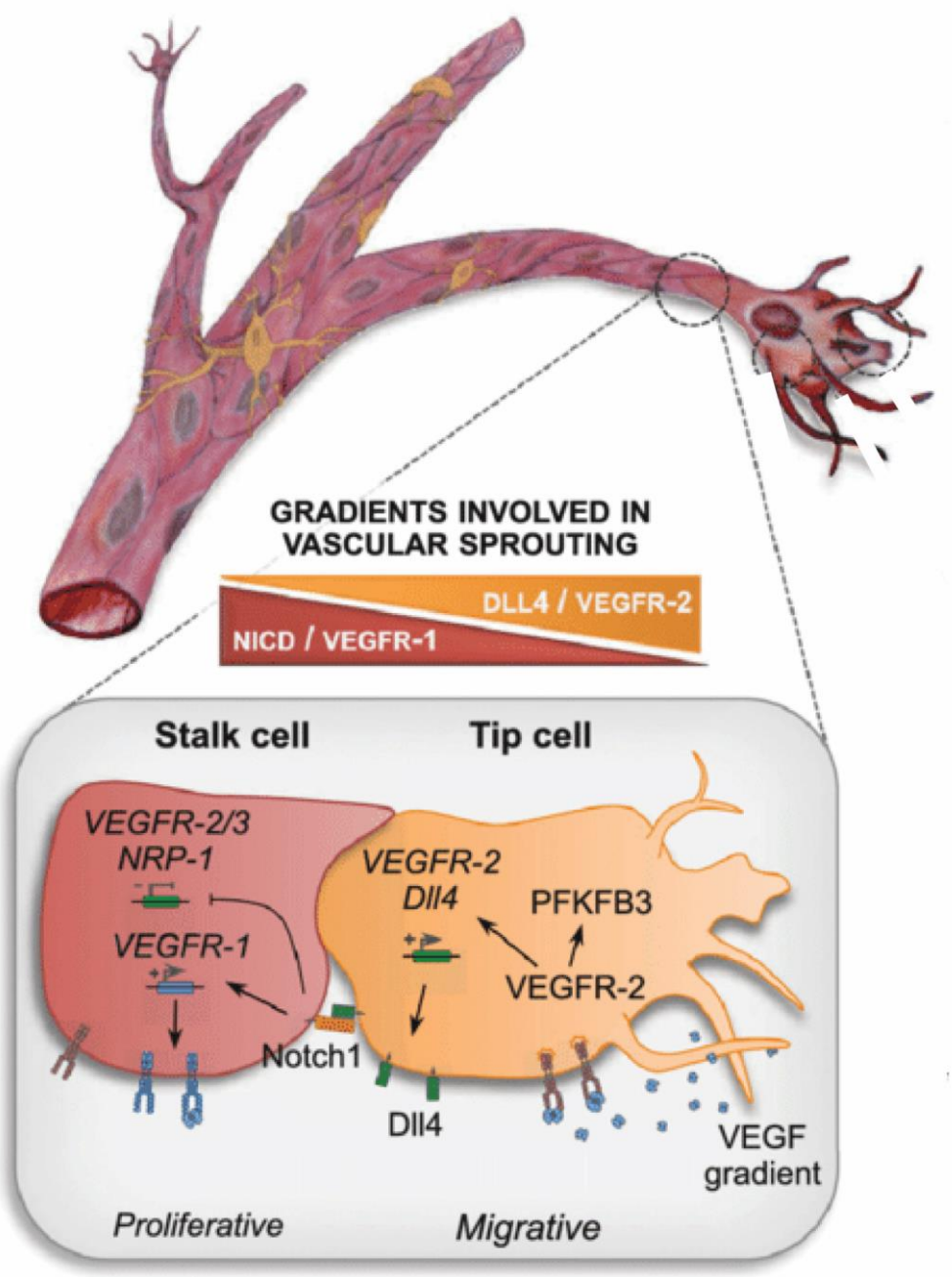

Figure 3: Endothelial cells signaling during sprouting angiogenesis. Sprouting vessel tip cell in response to VEGF-A binding to VEGFR2 (Flk-1). Flk-1 induces Notch ligand Dll4, leading to Notch receptor activation in adjacent endothelial cells. Once activated, the Notch intracellular domain (NICD) and downstream signaling cascade represses proangiogenic receptors Flk-1 and neuropilin-1 (NRP-1) while promoting VEGR1 (Flt-1), a negative regulator of VEGF and ligand sink. Image modified for relevance with permission from Treps, L, Conradi, L, Harjes, U, and Carmeliet, P (2016) Manipulating angiogenesis by targeting endothelial metabolism: Hitting the engine rather than the drivers- A new perspective?. *Pharmacological Reviews* 68: 872-887 doi: 10.1124/pr.116.012492.

During angiogenesis, lateral inhibition establishes distinct positioning of endothelial cells during sprouting initiation and elongation [40]. In this case, the endothelial cell that becomes the “tip cell” maintains its position as lead cell using lateral inhibition to suppress signaling activity within neighboring “stalk cells”, thereby facilitating the emergence of a productive sprout [40, 41, 55]. Whether in developmental stages or in the remodeling of established vasculature, these key signaling cues and endothelial cell behaviors are critical for establishing a healthy microvasculature.

Maturation of the Microvasculature

After microvascular remodeling occurs via angiogenic sprouting and vessel regression/pruning comes the final stage of vascular development—stabilization and maturation of the nascent vasculature [31]. Blood vessel maturation includes recruitment and investment of perivascular cells into the vessel wall. Depending on their morphology, location, and marker expression, perivascular cells are generally divided into two classes: VSMCs or pericytes [58, 59]. In larger diameter vessels, hemodynamic forces integrate with other mechanical and chemical cues to induce VSMC investment [59-61]. Higher levels of sheer stress contribute to VSMCs being recruited to arteries and arterioles where they concentrically wrap around the vascular tube [62, 63]. Vascular smooth muscle cells, or perhaps pericytes with contractile properties, are also found along terminal arterioles that precede the downstream capillary bed. NOTCH signaling also plays a role in perivascular cell differentiation and localization along the vasculature [64-66]. Although hemodynamics and NOTCH signaling can affect the locale and differentiation of these perivascular cells, VSMCs or pericytes, the hierarchy

of vessels is the main indicator of mural cell position. Arteries and arterioles mainly contain VSMCs, while the flow into capillaries sees the emergence of pericytes.

Basics of Pericyte Biology

Pericytes are typically found on smaller diameter vessels (less than 10 microns in diameter) and are embedded within the basement membrane in specific locations within a given network i.e. along vessel stalks or at vessel branch points [63, 67-69]. Pericyte morphology and their overall density on vessels may differs depending on the specific tissue of interest [68, 70, 71]. Canonical pericyte morphology is described as elongated cellular processes that extend along the abluminal side of capillary endothelium and form cell-cell contacts with endothelial cells through “peg-and-socket” connections surrounded by ECM. It is suggested that connexin-mediated gap junctions (e.g. Connexin43) and adheren junctions (e.g. N-cadherin) are crucial components of these “peg-and-socket” contact points, facilitating direct cross-talk between endothelial cells and pericytes [72-75].

Pericytes are proposed to have several key roles in blood vessel stabilization and maturation processes [76, 77]. They have been implicated in dynamically regulating capillary diameter and blood flow via contractility [78, 79], as well as in phagocytosis and removal of toxic factors [62]. Pericytes have been suggested to modulate tight and adherens junctions between endothelial cells in the vessel wall, thereby regulating vessel permeability, fluid movement, and transcytosis across the vessel wall [62, 77]. In the vasculature, these critical cell-cell adhesions are important for the integrity of the vessel wall. For example, anchoring or adherens junctions play a vital role in regulating

vessel permeability, such as VE-cadherin between endothelial cells and N-cadherin within the “peg-and-socket” connections between endothelial cells and pericytes. Tight junctions in vertebrates are necessary for the selective permeability between cells, such as ZO-1, Claudin5 and Occludin found in between endothelial cells. These junctions maintain a tightly regulated blood-tissue barrier that allows oxygen and nutrient delivery from the blood stream through diffusion and transcytosis but not overt leakage of blood components between endothelial cells. Finally, cell-cell communication junctions, such as gap junctions that form direct channels between cells or signal relaying junctions that transmit messages at points of anchoring junctions are key for all multicellular organization and function. While pericytes have been implicated in regulating endothelial cell junctions, another main function of pericytes is to promote vessel stability, in part through ECM deposition into the vascular basement membrane [58, 62, 80, 81].

The Role of the ECM in Blood Vessel Integrity

The primary function of the ECM within multicellular organisms is maintaining structural and mechanical integrity of tissues and organs. As with cell-cell adhesion molecules that can couple neighboring cell cytoskeletons together mechanically, ECM components also allow individual cells to “sense” mechanical stresses across a multicellular structure. The complex network of secreted ECM proteins and polysaccharide chains can be engaged by cells via integrins [12], another type of cell adhesion protein, which binds the cell to the ECM. The sub-micron-thick layer of ECM surrounding cells within the vessel wall is often referred to as the basement membrane or basal lamina. This

thin “sheet” of ECM molecules is flexible, mechanically robust, and an essential feature of nearly all epithelial structures [12, 82]. The basal laminae are typically between 40-120 nm thick and are essential for not only structural and filtering roles, but also for cell polarity and protein organization in adjacent cells. The basal lamina has also been implicated in regulation of cell metabolism, promoting cell proliferation, survival and differentiation, as well as facilitating cell migration [12]. Like all ECM-based structures, the basal lamina is composed of two main classes of macromolecules: (1) fibrillar proteins (typically glycoproteins such as laminins, Type IV collagen, and nidogen), and (2) proteoglycans (e.g. perlecan or heparin sulfate proteoglycan-2, Hspg2). Laminins are believed to be a primary component of the vascular basal lamina sheet structure [12, 82]. Early in development, the basal laminae consist mainly of laminin molecules of various but specific isoforms [12, 82]. The second main component of a mature basal laminae is Type IV collagen [12], which provides both tensile strength and anchoring motifs for various growth factors. Both laminin and Type IV collagen bind to perlecan and nidogen, additional components of the vascular basal lamina. Nidogen and perlecan serve predominantly as linkers to connect Type IV collagen and laminin into relatively stationary structures [12, 83]. Networks of laminins can then conceivably coordinate the assembly of other basal lamina components. Although the precise composition of a mature vascular basal lamina varies from tissue-to-tissue (and even region-to-region in some tissues), together these components are closely associated with other important structural such as Type XVII collagen and fibronectin, a fibrous protein that is critical for the adhesion of cells to connective tissue ECM. Additionally,

the basal lamina is critical for the anchoring of signaling molecules for the interactions between endothelial cells and perivascular cells.

Endothelial Cell–Pericyte Signaling Interactions

Many pathways converge to coordinate endothelial-pericyte interactions as well as the impact of those crucial interactions on the vascular system and on surrounding tissues. In embryonic development, for example, several key pathways are critical for the initial recruitment and investment of pericytes within the microvasculature [58]. Transforming growth factor-β (TGFβ) signaling promotes the differentiation of mural cells (vSMCs and pericytes), potentially downstream of gap junction formation between pericytes and endothelial cells [84]. Sphingosine-1-phosphate (S1P) signaling has been implicated in promoting the trafficking of N-cadherin in both endothelial cells and pericytes to support the formation of peg-and-socket contacts between these cells [85]. The Angiopoietin (Angpt)-Tie signaling pathway has also been described as an important mediator of pericyte-endothelial cell interactions. Angiopoietin 1 is an agonistic ligand that binds to Tie2 on endothelial cells. Angiopoietin 1 (Angpt1) is shown to be a mural cell specific ligand, indicating pericyte derived- paracrine signaling to endothelial cells [86]. Genetic studies in mice demonstrate the importance of Angpt1 in vessel maturation and quiescence. *Angpt1* null mice die at mid-gestation of cardiovascular failure- showing defective vasculature having poorly organized basement membrane and reduced coverage and detachment of pericytes [86-88]. Other studies indicate that overexpression of Angpt1 leads to expanded, stabilized, leakage resistant vasculature [87, 89]. While these and other pathways have emerged as modulators of pericyte-

endothelial cross-talk, I will focus on two of the more relevant signaling mechanisms, the PDGF-BB and NOTCH pathways.

PDGF-BB Signaling

One of the most important signaling cascades for the recruitment, migration, and proliferation of pericytes is the PDGF pathway [69, 80, 90]. The PDGF system consists of several proteins that combine into dimers to become a functional ligand capable of binding cognate receptors. These proteins can become hetero- or homodimers composed of A, B or C isoform subunits[91, 92]. The primary ligand for pericyte recruitment is the PDGF-BB homodimer (sometimes referred to as PDGF-B), though some studies have also implicated a heterodimer with the A and B subunits (PDGF-AB) [91-93]. PDGF-BB is synthesized and released by endothelial cells, specifically upregulated in endothelial “tip cells”, presumably to create a migration gradient for pericyte recruitment [94, 95]. PDGF-BB can become anchored to perlecan/HSPG-2 within the ECM to be presented to pericytes for binding PDGF Receptor-β (PDGFRβ) on their cell surface [95]. Genetic perturbation of PDGF-BB/PDGFRβ interactions can undermine pericyte recruitment and investment, leading to embryonic lethality in mutant mice owing to vascular abnormalities. In *Pdgfb* and *Pdgfrβ* knockout studies, insufficient pericyte coverage of developing vessels causes endothelial hyperplasia as well as an upregulation of VEGF-A, which in turn contributes to additional complications including vessel leakage and even hemorrhage [94, 96]. Pericyte differentiation can be induced in the absence of PDGF-BB signaling [90], but the lack of this signaling ligand impairs their

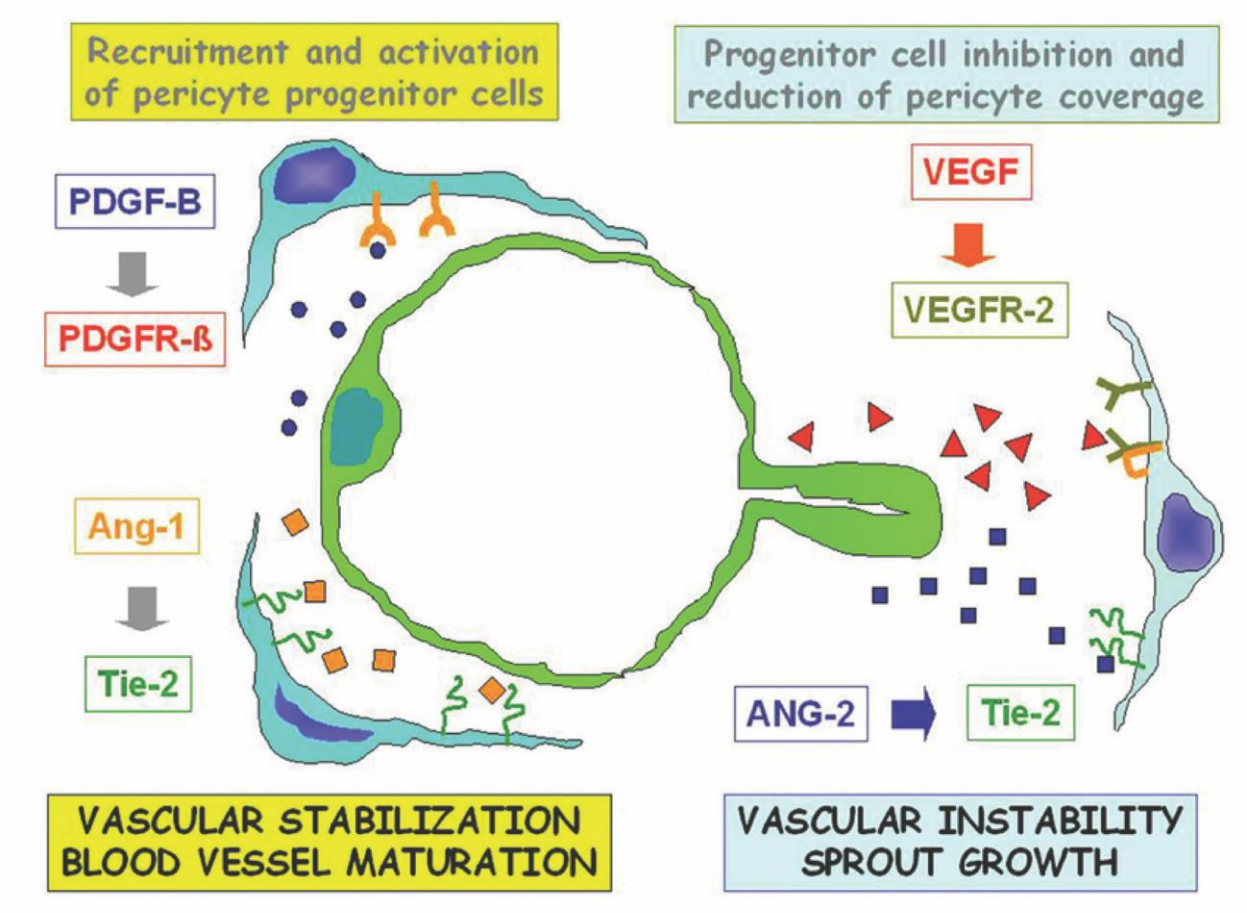

Figure 4: Schematic of paracrine signaling interactions between endothelial cells and pericytes in angiogenesis. Endothelial cells secrete PDGF-BB that recruits pericytes through PDGFRβ binding. Angiopoietin (Angpt) signaling has both agonistic and antagonistic effects of vessel stabilization and maturation. Angpt 1 released from endothelial cells binds to Tie-2 receptor on pericytes to surround and induce vessel investment, as well as other stabilization cues. Conversely, endothelial release of Angpt 2 binding causes a loss of pericytes from the vessel and vessel instability for new sprouting to occur or regression of vessels. Figure taken from Ribatti, D, Nico, B, and Crivellato, E (2011) The role of pericytes in angiogenesis. *International Journal of Developmental Biology.* 55:261-268. doi:10.1387/ijdb.103167dr under fair use.

migration and expansion along the vasculature, underscoring how critical this pathway is in pericyte proliferation and migration and ultimately coverage of microvessels. While PDGF-BB signaling is crucial for pericyte migration and locale, other pathways play key roles in interactions between endothelial cells and pericytes, such as the NOTCH pathway.

NOTCH Signaling

The NOTCH pathway has also been suggested to mediate endothelial cell-pericyte interactions for a variety of purposes [97, 98]. NOTCH signals have been implicated in the differentiation of pericytes into arterial or venous VSMCs. Data also exists suggesting the necessity for Jag1-NOTCH3 signaling in VSMC retention in the vasculature [58, 99]. Studies focused on NOTCH signaling in pericytes have yielded contradictory evidence, with data both supporting and opposing the requirement for NOTCH cues in pericyte differentiation, recruitment and maintenance in the microvasculature system [98, 100-103]. In Wang et al (2014), genetic mutation studies of notch3 in zebrafish resulted in an apparent decrease in the number of pericytes in brain microvasculature [97]. Through loss- and gain-of-function studies, the authors concluded pericyte number, via proliferation, was regulated by NOTCH3 signaling. Alternatively, Henshall et al (2015) found that in *Notch3* $^{-/-}$ mice, arterial VSMCs were the only cell type to be affected, despite pericytes also expressing *Notch3* [102]. A study by Volz et al (2015) also found that while NOTCH3 signaling was necessary for cells to differentiate into coronary artery VSMCs, pericytes within coronary microvasculature did not require *Notch3* for differentiation [104]. It is clear more research is needed into the

differences between perivascular cells and the signaling pathway for necessary for vessel formation and maturation, ushering in more insight into the complexities of a healthy, functional vascular system.

Pericytes: Contributions to Vascular Development Gone Awry?

A healthy and functioning vascular system arises from the precise spatial and temporal regulation of molecular cues during all stages of development. These signals coordinate the cellular interactions within similar and different cell types. Defects within any of these vital signaling pathways can have pathological or lethal consequences. In particular, tissue environments with excessive or unregulated VEGF-A signaling can impact multiple downstream pathways in both endothelial cells (directly) and pericytes (indirectly) [39, 42, 51, 96, 100, 101, 105]. Numerous pathologies arise in part from abnormal or higher VEGF-A signaling, including cancer progression and metastasis [106-109], proliferative diabetic retinopathy [110-112], and neonatal intraventricular hemorrhage [105, 113, 114]. A broad range of studies have described the functional consequences of a gain-of-function for VEGF-A signaling in endothelial cells, the impact on other components of the vasculature, such as pericytes and the basal lamina, are not as well understood. Pericytes in particular are known to be involved in certain vascular-related pathologies, in which the loss or lack of pericyte coverage leads to decreased vessel stability and increased leakage. Questions remain however about exactly which molecular mechanisms cause this loss or lack of pericytes? Is the initial insult to only endothelial cells, or are additional elements within the vasculature affected? Further understanding of how all components of the vessel wall may be

involved in these VEGF-A gain-of-function environments will shed light on developing more effective and precise therapies.

REFERENCES

1. *The top 10 causes of death*. Global Health Estimates 2018 24 May 2018; Available from: https://www.who.int/news-room/fact-sheets/detail/the-top-10-causes-of-death.
2. Udan, R.S., J.C. Culver, and M.E. Dickinson, *Understanding vascular development.* Wiley Interdiscip Rev Dev Biol, 2013. **2**(3): p. 327-46.
3. Beck, L., Jr. and P.A. D'Amore, *Vascular development: cellular and molecular regulation.* FASEB J, 1997. **11**(5): p. 365-73.
4. Carmeliet, P., *Angiogenesis in health and disease.* Nat Med, 2003. **9**(6): p. 653-60.
5. Carmeliet, P., *Angiogenesis in life, disease and medicine.* Nature, 2005. **438**(7070): p. 932-6.
6. Weinstein, B.M., *Vessels and nerves: marching to the same tune.* Cell, 2005. **120**(3): p. 299-302.
7. Matsumoto, K., et al., *Liver organogenesis promoted by endothelial cells prior to vascular function.* Science, 2001. **294**(5542): p. 559-63.
8. Collardeau-Frachon, S. and J.Y. Scoazec, *Vascular development and differentiation during human liver organogenesis.* Anat Rec (Hoboken), 2008. **291**(6): p. 614-27.
9. Magenheim, J., et al., *Blood vessels restrain pancreas branching, differentiation and growth.* Development, 2011. **138**(21): p. 4743-52.
10. Serini, G. and F. Bussolino, *Common cues in vascular and axon guidance.* Physiology (Bethesda), 2004. **19**: p. 348-54.
11. Yebra, M., et al., *Endothelium-derived Netrin-4 supports pancreatic epithelial cell adhesion and differentiation through integrins alpha2beta1 and alpha3beta1.* PLoS One, 2011. **6**(7): p. e22750.
12. Bruce Alberts, A.J., Julian Lewis, Martin Raff, Keith Roberts, Peter Walter, *Molecular Biology of the Cell, 5th Edition*. 5 ed. 2007: Garland Science 5th edition. 1392.
13. Hall, J.E., *Guyton and Hall Textbook of Medical Physiology, 13th Edition*. Guyton Physiology. 2016: Saunders, 13 edition.
14. Drake, C.J. and P.A. Fleming, *Vasculogenesis in the day 6.5 to 9.5 mouse embryo.* Blood, 2000. **95**(5): p. 1671-9.
15. Risau, W. and I. Flamme, *Vasculogenesis.* Annu Rev Cell Dev Biol, 1995. **11**: p. 73-91.
16. Flamme, I., T. Frolich, and W. Risau, *Molecular mechanisms of vasculogenesis and embryonic angiogenesis.* J Cell Physiol, 1997. **173**(2): p. 206-10.
17. Risau, W., *Mechanisms of angiogenesis.* Nature, 1997. **386**(6626): p. 671-4.

18. Poole, T.J. and J.D. Coffin, *Vasculogenesis and angiogenesis: two distinct morphogenetic mechanisms establish embryonic vascular pattern.* J Exp Zool, 1989. **251**(2): p. 224-31.
19. Korn, C. and H.G. Augustin, *Mechanisms of Vessel Pruning and Regression.* Dev Cell, 2015. **34**(1): p. 5-17.
20. Fischer, C., M. Schneider, and P. Carmeliet, *Principles and therapeutic implications of angiogenesis, vasculogenesis and arteriogenesis.* Handb Exp Pharmacol, 2006(176 Pt 2): p. 157-212.
21. Augustin, H.G., et al., *Ovarian angiogenesis. Phenotypic characterization of endothelial cells in a physiological model of blood vessel growth and regression.* Am J Pathol, 1995. **147**(2): p. 339-51.
22. Breier, G., et al., *Angiogenesis in embryos and ischemic diseases.* Thromb Haemost, 1997. **78**(1): p. 678-83.
23. Carmeliet, P., et al., *Impaired myocardial angiogenesis and ischemic cardiomyopathy in mice lacking the vascular endothelial growth factor isoforms VEGF164 and VEGF188.* Nat Med, 1999. **5**(5): p. 495-502.
24. Holash, J., et al., *Vessel cooption, regression, and growth in tumors mediated by angiopoietins and VEGF.* Science, 1999. **284**(5422): p. 1994-8.
25. Marti, H.H. and W. Risau, *Angiogenesis in ischemic disease.* Thromb Haemost, 1999. **82 Suppl 1**: p. 44-52.
26. Tsuzuki, Y., et al., *Pancreas microenvironment promotes VEGF expression and tumor growth: novel window models for pancreatic tumor angiogenesis and microcirculation.* Lab Invest, 2001. **81**(10): p. 1439-51.
27. Fraser, H.M. and W.C. Duncan, *Vascular morphogenesis in the primate ovary.* Angiogenesis, 2005. **8**(2): p. 101-16.
28. Goveia, J., P. Stapor, and P. Carmeliet, *Principles of targeting endothelial cell metabolism to treat angiogenesis and endothelial cell dysfunction in disease.* EMBO Mol Med, 2014. **6**(9): p. 1105-20.
29. Olfert, I.M., et al., *Myocyte vascular endothelial growth factor is required for exercise-induced skeletal muscle angiogenesis.* Am J Physiol Regul Integr Comp Physiol, 2010. **299**(4): p. R1059-67.
30. Folkman, J., *Seminars in Medicine of the Beth Israel Hospital, Boston. Clinical applications of research on angiogenesis.* N Engl J Med, 1995. **333**(26): p. 1757-63.
31. Jain, R.K., *Molecular regulation of vessel maturation.* Nat Med, 2003. **9**(6): p. 685-93.
32. Ondine Cleaver, P.A.K., *Vascular Development*, in *Heart Development and Regeneration*. 2010. p. 487-528.
33. Goldie, L.C., M.K. Nix, and K.K. Hirschi, *Embryonic vasculogenesis and hematopoietic specification.* Organogenesis, 2008. **4**(4): p. 257-63.
34. Arora, R. and V.E. Papaioannou, *The murine allantois: a model system for the study of blood vessel formation.* Blood, 2012. **120**(13): p. 2562-72.
35. Djonov, V.G., A.B. Galli, and P.H. Burri, *Intussusceptive arborization contributes to vascular tree formation in the chick chorio-allantoic membrane.* Anat Embryol (Berl), 2000. **202**(5): p. 347-57.

36. Djonov, V., et al., *Intussusceptive angiogenesis: its role in embryonic vascular network formation.* Circ Res, 2000. **86**(3): p. 286-92.
37. Jakobsson, L., et al., *Endothelial cells dynamically compete for the tip cell position during angiogenic sprouting.* Nat Cell Biol, 2010. **12**(10): p. 943-53.
38. Gerhardt, H., *VEGF and endothelial guidance in angiogenic sprouting.* Organogenesis, 2008. **4**(4): p. 241-6.
39. Hellstrom, M., L.K. Phng, and H. Gerhardt, *VEGF and Notch signaling: the yin and yang of angiogenic sprouting.* Cell Adh Migr, 2007. **1**(3): p. 133-6.
40. Hellstrom, M., et al., *Dll4 signalling through Notch1 regulates formation of tip cells during angiogenesis.* Nature, 2007. **445**(7129): p. 776-80.
41. Chappell, J.C., K.P. Mouillesseaux, and V.L. Bautch, *Flt-1 (vascular endothelial growth factor receptor-1) is essential for the vascular endothelial growth factor-Notch feedback loop during angiogenesis.* Arterioscler Thromb Vasc Biol, 2013. **33**(8): p. 1952-9.
42. Kappas, N.C., et al., *The VEGF receptor Flt-1 spatially modulates Flk-1 signaling and blood vessel branching.* J Cell Biol, 2008. **181**(5): p. 847-58.
43. Gerhardt, H., et al., *VEGF guides angiogenic sprouting utilizing endothelial tip cell filopodia.* J Cell Biol, 2003. **161**(6): p. 1163-77.
44. Strilic, B., et al., *Electrostatic cell-surface repulsion initiates lumen formation in developing blood vessels.* Curr Biol, 2010. **20**(22): p. 2003-9.
45. Strilic, B., T. Kucera, and E. Lammert, *Formation of cardiovascular tubes in invertebrates and vertebrates.* Cell Mol Life Sci, 2010. **67**(19): p. 3209-18.
46. Iruela-Arispe, M.L. and G.E. Davis, *Cellular and molecular mechanisms of vascular lumen formation.* Dev Cell, 2009. **16**(2): p. 222-31.
47. Shibuya, M. and L. Claesson-Welsh, *Signal transduction by VEGF receptors in regulation of angiogenesis and lymphangiogenesis.* Exp Cell Res, 2006. **312**(5): p. 549-60.
48. Shibuya, M., *Vascular endothelial growth factor (VEGF)-Receptor2: its biological functions, major signaling pathway, and specific ligand VEGF-E.* Endothelium, 2006. **13**(2): p. 63-9.
49. Veikkola, T., et al., *Signalling via vascular endothelial growth factor receptor-3 is sufficient for lymphangiogenesis in transgenic mice.* EMBO J, 2001. **20**(6): p. 1223-31.
50. Stacker, S.A., et al., *VEGF-D promotes the metastatic spread of tumor cells via the lymphatics.* Nat Med, 2001. **7**(2): p. 186-91.
51. Chappell, J.C., et al., *Flt-1 (VEGFR-1) coordinates discrete stages of blood vessel formation.* Cardiovasc Res, 2016. **111**(1): p. 84-93.
52. Krueger, J., et al., *Flt1 acts as a negative regulator of tip cell formation and branching morphogenesis in the zebrafish embryo.* Development, 2011. **138**(10): p. 2111-20.
53. Roberts, D.M., et al., *The vascular endothelial growth factor (VEGF) receptor Flt-1 (VEGFR-1) modulates Flk-1 (VEGFR-2) signaling during blood vessel formation.* Am J Pathol, 2004. **164**(5): p. 1531-5.
54. Alva, J.A. and M.L. Iruela-Arispe, *Notch signaling in vascular morphogenesis.* Curr Opin Hematol, 2004. **11**(4): p. 278-83.

55. Funahashi, Y., et al., *Notch regulates the angiogenic response via induction of VEGFR-1.* J Angiogenes Res, 2010. **2**(1): p. 3.
56. Kangsamaksin, T., et al., *NOTCH decoys that selectively block DLL/NOTCH or JAG/NOTCH disrupt angiogenesis by unique mechanisms to inhibit tumor growth.* Cancer Discov, 2015. **5**(2): p. 182-97.
57. Iso, T., L. Kedes, and Y. Hamamori, *HES and HERP families: multiple effectors of the Notch signaling pathway.* J Cell Physiol, 2003. **194**(3): p. 237-55.
58. Armulik, A., A. Abramsson, and C. Betsholtz, *Endothelial/pericyte interactions.* Circ Res, 2005. **97**(6): p. 512-23.
59. van Dijk, C.G., et al., *The complex mural cell: pericyte function in health and disease.* Int J Cardiol, 2015. **190**: p. 75-89.
60. Mitsumata, M., et al., *Fluid shear stress stimulates platelet-derived growth factor expression in endothelial cells.* Am J Physiol, 1993. **265**(1 Pt 2): p. H3-8.
61. Hsieh, H.J., N.Q. Li, and J.A. Frangos, *Shear stress increases endothelial platelet-derived growth factor mRNA levels.* Am J Physiol, 1991. **260**(2 Pt 2): p. H642-6.
62. Bell, R.D., et al., *Pericytes control key neurovascular functions and neuronal phenotype in the adult brain and during brain aging.* Neuron, 2010. **68**(3): p. 409-27.
63. Ando, K., et al., *Clarification of mural cell coverage of vascular endothelial cells by live imaging of zebrafish.* Development, 2016. **143**(8): p. 1328-39.
64. Liu, H., et al., *Notch3 is critical for proper angiogenesis and mural cell investment.* Circ Res, 2010. **107**(7): p. 860-70.
65. Liu, H., S. Kennard, and B. Lilly, *NOTCH3 expression is induced in mural cells through an autoregulatory loop that requires endothelial-expressed JAGGED1.* Circ Res, 2009. **104**(4): p. 466-75.
66. Tang, Y., et al., *Notch and transforming growth factor-beta (TGFbeta) signaling pathways cooperatively regulate vascular smooth muscle cell differentiation.* J Biol Chem, 2010. **285**(23): p. 17556-63.
67. Attwell, D., et al., *What is a pericyte?* J Cereb Blood Flow Metab, 2016. **36**(2): p. 451-5.
68. Berthiaume, A.A., et al., *Dynamic Remodeling of Pericytes In Vivo Maintains Capillary Coverage in the Adult Mouse Brain.* Cell Rep, 2018. **22**(1): p. 8-16.
69. Benjamin, L.E., I. Hemo, and E. Keshet, *A plasticity window for blood vessel remodelling is defined by pericyte coverage of the preformed endothelial network and is regulated by PDGF-B and VEGF.* Development, 1998. **125**(9): p. 1591-8.
70. Mathiisen, T.M., et al., *The perivascular astroglial sheath provides a complete covering of the brain microvessels: an electron microscopic 3D reconstruction.* Glia, 2010. **58**(9): p. 1094-103.
71. Sims, D.E., *The pericyte--a review.* Tissue Cell, 1986. **18**(2): p. 153-74.
72. Hirschi, K.K. and P.A. D'Amore, *Pericytes in the microvasculature.* Cardiovasc Res, 1996. **32**(4): p. 687-98.
73. Li, A.F., et al., *High glucose alters connexin 43 expression and gap junction intercellular communication activity in retinal pericytes.* Invest Ophthalmol Vis Sci, 2003. **44**(12): p. 5376-82.

74. Gerhardt, H., H. Wolburg, and C. Redies, *N-cadherin mediates pericytic-endothelial interaction during brain angiogenesis in the chicken.* Dev Dyn, 2000. **218**(3): p. 472-9.
75. Cuevas, P., et al., *Pericyte endothelial gap junctions in human cerebral capillaries.* Anat Embryol (Berl), 1984. **170**(2): p. 155-9.
76. Diaz-Flores, L., et al., *Pericytes. Morphofunction, interactions and pathology in a quiescent and activated mesenchymal cell niche.* Histol Histopathol, 2009. **24**(7): p. 909-69.
77. Daneman, R., et al., *Pericytes are required for blood-brain barrier integrity during embryogenesis.* Nature, 2010. **468**(7323): p. 562-6.
78. Hill, R.A., et al., *Regional Blood Flow in the Normal and Ischemic Brain Is Controlled by Arteriolar Smooth Muscle Cell Contractility and Not by Capillary Pericytes.* Neuron, 2015. **87**(1): p. 95-110.
79. Hamilton, N.B., D. Attwell, and C.N. Hall, *Pericyte-mediated regulation of capillary diameter: a component of neurovascular coupling in health and disease.* Front Neuroenergetics, 2010. **2**.
80. Gaengel, K., et al., *Endothelial-mural cell signaling in vascular development and angiogenesis.* Arterioscler Thromb Vasc Biol, 2009. **29**(5): p. 630-8.
81. Stratman, A.N., et al., *Pericyte recruitment during vasculogenic tube assembly stimulates endothelial basement membrane matrix formation.* Blood, 2009. **114**(24): p. 5091-101.
82. Hamill, K.J., et al., *Laminin deposition in the extracellular matrix: a complex picture emerges.* J Cell Sci, 2009. **122**(Pt 24): p. 4409-17.
83. Frantz, C., K.M. Stewart, and V.M. Weaver, *The extracellular matrix at a glance.* J Cell Sci, 2010. **123**(Pt 24): p. 4195-200.
84. Hirschi, K.K., et al., *Gap junction communication mediates transforming growth factor-beta activation and endothelial-induced mural cell differentiation.* Circ Res, 2003. **93**(5): p. 429-37.
85. Paik, J.H., et al., *Sphingosine 1-phosphate receptor regulation of N-cadherin mediates vascular stabilization.* Genes Dev, 2004. **18**(19): p. 2392-403.
86. Suri, C., et al., *Requisite role of angiopoietin-1, a ligand for the TIE2 receptor, during embryonic angiogenesis.* Cell, 1996. **87**(7): p. 1171-80.
87. Suri, C., et al., *Increased vascularization in mice overexpressing angiopoietin-1.* Science, 1998. **282**(5388): p. 468-71.
88. Dumont, D.J., et al., *Dominant-negative and targeted null mutations in the endothelial receptor tyrosine kinase, tek, reveal a critical role in vasculogenesis of the embryo.* Genes Dev, 1994. **8**(16): p. 1897-909.
89. Thurston, G., et al., *Leakage-resistant blood vessels in mice transgenically overexpressing angiopoietin-1.* Science, 1999. **286**(5449): p. 2511-4.
90. Hellstrom, M., et al., *Role of PDGF-B and PDGFR-beta in recruitment of vascular smooth muscle cells and pericytes during embryonic blood vessel formation in the mouse.* Development, 1999. **126**(14): p. 3047-55.
91. Fredriksson, L., H. Li, and U. Eriksson, *The PDGF family: four gene products form five dimeric isoforms.* Cytokine Growth Factor Rev, 2004. **15**(4): p. 197-204.
92. Andrae, J., R. Gallini, and C. Betsholtz, *Role of platelet-derived growth factors in physiology and medicine.* Genes Dev, 2008. **22**(10): p. 1276-312.

93. Chandrakanthan, V., et al., *PDGF-AB and 5-Azacytidine induce conversion of somatic cells into tissue-regenerative multipotent stem cells.* Proc Natl Acad Sci U S A, 2016. **113**(16): p. E2306-15.
94. Abramsson, A., P. Lindblom, and C. Betsholtz, *Endothelial and nonendothelial sources of PDGF-B regulate pericyte recruitment and influence vascular pattern formation in tumors.* J Clin Invest, 2003. **112**(8): p. 1142-51.
95. Lindblom, P., et al., *Endothelial PDGF-B retention is required for proper investment of pericytes in the microvessel wall.* Genes Dev, 2003. **17**(15): p. 1835-40.
96. Hellstrom, M., et al., *Lack of pericytes leads to endothelial hyperplasia and abnormal vascular morphogenesis.* J Cell Biol, 2001. **153**(3): p. 543-53.
97. Wang, Y., et al., *Notch3 establishes brain vascular integrity by regulating pericyte number.* Development, 2014. **141**(2): p. 307-17.
98. Ji, Y., et al., *Jagged1/Notch3 Signaling Modulates Hemangioma-Derived Pericyte Proliferation and Maturation.* Cell Physiol Biochem, 2016. **40**(5): p. 895-907.
99. Winkler, E.A., R.D. Bell, and B.V. Zlokovic, *Lack of Smad or Notch leads to a fatal game of brain pericyte hopscotch.* Dev Cell, 2011. **20**(3): p. 279-80.
100. Darden, J., et al., *Excess vascular endothelial growth factor-A disrupts pericyte recruitment during blood vessel formation.* Angiogenesis, 2018.
101. Jin, S., et al., *Notch signaling regulates platelet-derived growth factor receptor-beta expression in vascular smooth muscle cells.* Circ Res, 2008. **102**(12): p. 1483-91.
102. Henshall, T.L., et al., *Notch3 is necessary for blood vessel integrity in the central nervous system.* Arterioscler Thromb Vasc Biol, 2015. **35**(2): p. 409-20.
103. Kofler, N.M., et al., *Combined deficiency of Notch1 and Notch3 causes pericyte dysfunction, models CADASIL, and results in arteriovenous malformations.* Sci Rep, 2015. **5**: p. 16449.
104. Volz, K.S., et al., *Pericytes are progenitors for coronary artery smooth muscle.* Elife, 2015. **4**.
105. Ballabh, P., et al., *Angiogenic inhibition reduces germinal matrix hemorrhage.* Nat Med, 2007. **13**(4): p. 477-85.
106. Buysschaert, I., P. Carmeliet, and M. Dewerchin, *Clinical and fundamental aspects of angiogenesis and anti-angiogenesis.* Acta Clin Belg, 2007. **62**(3): p. 162-9.
107. Potente, M., H. Gerhardt, and P. Carmeliet, *Basic and therapeutic aspects of angiogenesis.* Cell, 2011. **146**(6): p. 873-87.
108. Belting, M., et al., *Regulation of angiogenesis by tissue factor cytoplasmic domain signaling.* Nat Med, 2004. **10**(5): p. 502-9.
109. Bono, F., et al., *Inhibition of tumor angiogenesis and growth by a small-molecule multi-FGF receptor blocker with allosteric properties.* Cancer Cell, 2013. **23**(4): p. 477-88.
110. Arboleda-Velasquez, J.F., et al., *Notch signaling functions in retinal pericyte survival.* Invest Ophthalmol Vis Sci, 2014. **55**(8): p. 5191-9.
111. Hammes, H.P., et al., *Pericytes and the pathogenesis of diabetic retinopathy.* Diabetes, 2002. **51**(10): p. 3107-12.

112. Hammes, H.P., et al., *Angiopoietin-2 causes pericyte dropout in the normal retina: evidence for involvement in diabetic retinopathy.* Diabetes, 2004. **53**(4): p. 1104-10.
113. Ballabh, P., *Pathogenesis and prevention of intraventricular hemorrhage.* Clin Perinatol, 2014. **41**(1): p. 47-67.
114. Yang, D., et al., *Overexpression of vascular endothelial growth factor in the germinal matrix induces neurovascular proteases and intraventricular hemorrhage.* Sci Transl Med, 2013. **5**(193): p. 193ra90.

CHAPTER 2

Excess Vascular Endothelial Growth Factor-A Disrupts Pericyte Recruitment during Blood Vessel Formation

Jordan Darden[1,2], Laura Beth Payne[1], Huaning Zhao[1,3], John C. Chappell[1,2,3,4]

[1]Center for Heart and Regenerative Medicine, Virginia Tech Carilion Research Institute, Roanoke, VA 24016, USA

[2]Graduate Program in Translational Biology, Medicine, and Health, [3]Department of Biomedical Engineering and Mechanics, Virginia Polytechnic Institute and State University, Blacksburg, VA 24061, USA

[4]Department of Basic Science Education, Virginia Tech Carilion School of Medicine, Roanoke, VA 24016, USA

ABSTRACT

Pericyte investment into new blood vessels is essential for vascular development such that mis-regulation within this phase of vessel formation can contribute to numerous pathologies including arteriovenous and cerebrovascular malformations. It is critical therefore to illuminate how angiogenic signaling pathways intersect to regulate pericyte migration and investment. Here, we disrupted vascular endothelial growth factor-A (VEGF-A) signaling in *ex vivo* and *in vitro* models of sprouting angiogenesis, and found pericyte coverage to be compromised during VEGF-A perturbations. Pericytes had little to no expression of VEGF receptors, suggesting VEGF-A signaling defects affect endothelial cells directly but pericyte indirectly. Live imaging of *ex vivo* angiogenesis in mouse embryonic skin revealed limited pericyte migration during exposure to exogenous VEGF-A. During VEGF-A gain-of-function conditions, pericytes and endothelial cells

displayed abnormal transcriptional changes within the platelet-derived growth factor-B (PDGF-B) and Notch pathways. To further test potential crosstalk between these pathways in pericytes, we stimulated embryonic pericytes with Notch ligands Delta-like 4 (Dll4) and Jagged-1 (Jag1) and found induction of Notch pathway activity but no changes in PDGF Receptor-β (*Pdgfrβ*) expression. In contrast, PDGFRβ protein levels decreased with mis-regulated VEGF-A activity, observed in the effects on full-length PDGFRβ and a truncated PDGFRβ isoform generated by proteolytic cleavage or potentially by mRNA splicing. Overall, these observations support a model in which, during the initial stages of vascular development, pericyte distribution and coverage are indirectly affected by endothelial cell VEGF-A signaling and the downstream regulation of PDGF-B-PDGFRβ dynamics, without substantial involvement of pericyte Notch signaling during these early stages.

INTRODUCTION

Each year, millions of patients are afflicted by pathological conditions that arise from structural abnormalities within the vascular system [1]. In particular, defective blood vessel formation within neurological tissues can increase patient risk for sudden, life-threatening events such as a stroke or aneurysm. Notable examples of these cerebrovascular disorders include arteriovenous malformations (AVMs), cerebral cavernous malformations (CCMs), and cerebral autosomal dominant arteriopathy with subcortical infarcts and leukoencephalopathy (CADASIL) [2-4]. In addition to these pathologies, vascular anomalies can pose severe health risks to pediatric patients, as poorly formed cerebrovasculature can lead to a hemorrhagic stroke and numerous related health consequences, particularly in premature infants [5]. Development of these blood

vessels depends heavily on the precise integration of spatio-temporal cues and cellular responses to achieve proper vessel structure and patterning for adequate oxygen delivery and nutrient exchange.

Of the molecular signals that initiate and pattern new vessel formation, vascular endothelial growth factor-A (VEGF-A) is one of most potent, eliciting numerous downstream effects in vascular endothelial cells [6,7]. Inputs from additional signaling networks therefore modulate the pleiotropic effects of VEGF-A to coordinate endothelial cell migration [8], proliferation [9], and shape change [10], among other key behaviors. Crosstalk between the VEGF-A and Notch pathways, for example, is critical for a subset of endothelial cells to adopt a sprouting phenotype (i.e. an endothelial “tip” cell), while other endothelial cells trail behind these leading cells and proliferate to elongate the nascent vessel branch [11-13]. Disrupting this intersection between VEGF-A and Notch signaling not only undermines endothelial sprouting, but also compromises downstream regulation of other pathways including the platelet-derived growth factor-B (PDGF-B) pathway [14,15]. PDGF-B signals are critical for promoting vascular network progression through the recruitment and expansion of mural cells i.e. vascular smooth muscle cells and pericytes [16]. These unique signaling interactions therefore orchestrate each stage of vessel formation, from mechanisms governing angiogenic sprouting and remodeling to those underlying vessel stabilization and maturation by mural cells.

Pericytes contribute to the development of mature vascular beds by maintaining endothelial cell junction integrity [17,18] and synthesizing extracellular matrix (ECM) components of the surrounding vessel basement membrane [19]. In addition to these more established roles, unique pericyte functions are still being discovered in normal and

disease settings. For instance, pericytes in neural tissue may play a physiological role in blood flow distribution through vasocontractility [20,21], but this function may also go awry in certain pathological scenarios by contributing to limited tissue reperfusion following ischemia [22,23]. To perform these and other critical functions in sustaining tissue health, pericytes must establish sufficient coverage along the vasculature through their migration along and investment into the vessel wall [24]. These important cellular processes that promote pericyte coverage are also mediated, in part, by the intricate interplay between the signaling cascades described briefly above, that is, the VEGF-A, Notch, and PDGF-B pathways.

Notch and VEGF-A signaling have also been implicated in regulating pericyte behaviors directly [25,26], but evidence suggesting a context-dependence for these pathways in pericytes [27-33], as well as their crosstalk with the PDGF-B pathway [4,34-39], highlights the need for further clarification of these signaling relationships. Pericytes express PDGF Receptor-β (PDGFRβ) on their surface to bind PDGF-B ligands and facilitate downstream intracellular signaling events [40]. Pericyte coverage therefore depends on competent PDGF-B signaling, as targeted disruption of this pathway leads to compromised pericyte investment within the vessel wall across many tissue beds [16,41-43]. Given the sensitivity of pericytes to PDGF-B signals, it is perhaps not surprising that soluble isoforms of PDGFRβ have recently been identified [44-47]. These observations suggest the existence of a negative feedback loop that modulates PDGF-B signaling to "fine-tune" pericyte behaviors in certain contexts, though this potential mechanism remains relatively unexplored.

In the present study, we utilized *in vitro* and *ex vivo* models of sprouting angiogenesis in which pericytes migrated along and expanded their coverage of developing blood vessels. Because of its critical role in vessel formation, we targeted VEGF-A signaling directly by manipulating Flt1 (VEGF Receptor-1), a negative regulator of VEGF-A that acts primarily as a "decoy" or ligand sink during vessel development [9,11]. Although Flt1 also binds Placental Growth Factor (PlGF) and VEGF-B, the intracellular tyrosine kinase domain of Flt1 is dispensable for normal vascular development [48], again supporting its function as a ligand trap. In addition, while VEGF-A signals through Flk1/Kdr (VEGF Receptor-2) on endothelial cells, Flt1 binds VEGF-A with a 10-fold higher affinity than Flk1/Kdr [49], consistent with a role in regulating available VEGF-A ligand. Genetic loss of *Flt1* in fact leads to excessive and aberrant Flk1 activation via increased receptor phosphorylation, as observed in ESC-derived vessels and the developing postnatal mouse retina [8,9,50-54]. Disrupting VEGF-A activity genetically (*flt1*$^{-/-}$) or pharmacologically (exogenous VEGF-A) impaired pericyte distribution and coverage on the developing vasculature, with pericyte migration being restricted during exposure to elevated VEGF-A levels. These VEGF-A gain-of-function scenarios [9,50-53] led to abnormal transcriptional changes within the Notch and PDGF-B pathways in both pericytes and endothelial cells. Although these transcriptional irregularities suggested potential connections between these two pathways, we found that stimulating embryonic pericytes with Notch ligands [Delta-like 4 (Dll4) and Jagged-1 (Jag1)] did not alter *Pdgfr*β expression. We did however observe a decrease in PDGFRβ protein levels during disrupted VEGF-A activity and specifically in the levels of a truncated PDGFRβ isoform. These PDGFRβ isoforms have been detected in a number of settings [44-47,55], and their relative amounts appear to vary with corresponding PDGF-B levels

and potentially with proteolytic cleavage events [45], though mRNA splice variants cannot be ruled out. Overall, these data demonstrate that, in early developmental blood vessel formation, pericyte distribution and coverage depend on proper VEGF-A activity and its downstream impact on PDGF-B-PDGFRβ dynamics, without substantial involvement of the Notch pathway during these initial stages.

MATERIALS AND METHODS

Cell Culture and In Vitro Differentiation

WT and *flt1*$^{-/-}$ mouse embryonic stem cells (ESCs) were a gift of V.L. Bautch (University of North Carolina at Chapel Hill) and Guo-Hua Fong (University of Connecticut). Undifferentiated cells were maintained through leukemia inhibitory factor (LIF) exposure as described previously [56]. After undifferentiated WT and *flt1*$^{-/-}$ ESCs gave rise to spherical embryoid bodies (EBs) (i.e. over 3-4 days in culture), these EBs were released from the culture plate and collected using 1x dispase (Gibco, Cat #17105-041) in PBS (i.e. experimental Day 0). EBs were washed twice with PBS and re-plated in differentiation media (see Online Resource 1 – Supplemental Materials and Methods) in 10 cm^2 petri dishes (i.e. non-tissue culture treated plastic). The cell suspension in media was added at 5 mls per plate and cultured at 37ºC and 5% CO_2. On experimental Day 3 (i.e. 3 days after dispase), EBs were transferred to slide flasks (ThermoFisher, Cat #170920) using sterile wide-tip transfer pipets. Differentiating EBs were cultured for a 5-7 additional days, feeding at Days 5 and 8, for a total of 8-10 days. Differentiated cells were washed twice with PBS and processed for (i) immunocytochemistry (ICC) and confocal imaging or (ii)

cell-type enrichment and transcriptional profiling by quantitative Real-Time PCR (qRT-PCR).

Immunocytochemistry and Quantitative Image Analysis

Differentiated ESCs were fixed at designated end-points with either (i) 50:50 solution of methanol and acetone for 6 mins, or (ii) 4% paraformaldehyde (PFA) for 5 mins. Samples were stored in PBS at 4°C until further processing. Immunostaining of differentiated ESCs in slide flasks was performed with the following primary antibodies: rabbit anti-neural glial antigen-2 (Ng2, EMD Millipore, Cat #AB5320), rat anti-platelet-endothelial cell adhesion molecule-1 (Pecam1/CD31, BD Pharminogen, Cat #553370), and mouse anti-β-Galactosidase (β-Gal, ThermoFisher, Cat #MA1-152). Secondary antibodies included: donkey anti-rat AlexaFluor 488 (Jackson Immunoresearch, Cat #705-545-147), donkey anti-rabbit AlexaFluor 568 (Invitrogen, Cat #A10042), and donkey anti-mouse AlexaFluor 647 (Abcam, Cat #ab150107). Cell nuclei were labeled with 4′,6-Diamidino-2-phenylindole dihydrochloride (DAPI, Sigma, Cat #D9542). All antibodies were used at a 1:1000 concentration. Fixed ESCs were washed twice with PBS, and non-specific antigens were blocked with a 3% bovine serum albumin (BSA, Sigma, A2153-100G) solution in PBS (with 0.01% sodium azide as a preservative) at room temperature for 1 hour. Samples were incubated in primary antibody solutions overnight at 4°C followed by PBS washes (3x with 10 mins per wash). Secondary antibodies plus DAPI were incubated for 4 hours at room temperature followed by 3 more PBS washes. After PBS was aspirated, slide flask chambers were removed, and a line of Vectashield mounting media

(Vector Labs, Cat #H-1000) was applied on the culture area. A cover slip was applied (22 mm x 60 mm – 1.5 thickness, ThermoFisher, Cat #12-544G), and slides were sealed with clear nail polish (Electron Microscopy Sciences, Cat #72180).

Differentiated ESCs were imaged with a Zeiss LSM880 confocal microscope using a 40x water objective. Images were collected in 5-30 confocal scans through the z-axis and flattened. Image analysis was conducted with ImageJ/FIJI software available for download at https://fiji.sc/ [57]. Ng2+ cells were assessed visually in three dimensions to confirm direct association with Pecam1+ endothelial cells, and those not clearly associated with developing vessels were excluded from pericyte coverage analysis. Color channels were separated, and Pecam1+ endothelial cell area was determined through application of a pixel intensity threshold value. Regions of overlaps between Ng2+ signal and Pecam1+ endothelial cells were established, and pixel areas of these overlapping regions were measured. Percent of pericyte coverage was calculated by dividing the area of Ng2+ overlap with Pecam1+ cells by the total Pecam1+ vessel area. FIJI plugin cell counter and fixed diameter macros were used to analyze the distribution of Ng2+ pericytes throughout the ESC-derived vasculature. Ng2+ pericyte distributions were measured relative to (i) vessel morphological features (i.e. vessel stalks, branch points, or thicker areas) and (ii) other Ng2+ cells in close proximity (i.e. within a 50-micron radius).

Endothelial Cell and Pericyte Enrichment

Mouse WT and *flt1*$^{-/-}$ ESCs were differentiated for 10 days on tissue culture-treated 10 cm^2 plates (Corning, Cat #430167) per cell type. Pericytes and endothelial cells were enriched from ESC cultures using magnet-assisted cell sorting (MACS) (Miltenyi Biotec),

as described previously [11]. Briefly, cells were dissociated through incubation in 7 mL of a 50:50 solution of dispase (2x) and type 1 collagenase (Fisher, Cat #NC9633623) at 37°C for 40 minutes. Cultures were also mechanically dissociated by pipetting until in suspension. The resultant cell suspension was then filtered (70-micron bucket filter) to yield single cells, which were centrifuged and dissociation enzymes aspirated. Cells were resuspended in autoMACS® running buffer (Miltenyi Biotec, Cat #130-091-221). Fc-Receptor blocking reagent (Miltenyi Biotech, Cat #130-092-575) was added per manufacturer instructions and incubated for 20 mins at 4°C, agitating each tube every 5 mins. After centrifugation and supernatant aspiration, cells were resuspended in autoMACS® buffer containing anti-An2 microbeads (Miltenyi Biotec, Cat #130-097-170). An2 is a homologue of Ng2 [58]. Additionally, microbeads were 50-nm superparamagnetic particles, avoiding cell stimulation. Following centrifugation, aspiration of microbead solution, and resuspension in autoMACS® buffer, labeled cells were manually passed through QuadroMACS separator LS columns (Miltenyi Biotec, Cat #130-091-051, 30-micron pre-separation filters) per manufacturer recommendations. Cells flowing through the column but not isolated by the magnetic field were collected for secondary selection of endothelial cells. After centrifugation of these “flow-through” cells, sorting buffer was aspirated, and cells were resuspended in MACS® buffer. Following incubation with Pecam1/CD31 primary antibodies conjugated to R-phycoerythrin (PE) (BD Pharminogen, Cat #553373), cells were then incubated with anti-PE microbeads, as described above. After each MACS column separation, target populations were collected, as well as the final “flow through” cells, all of which were centrifuged and resuspended in

buffers formulated for additional analysis of mRNA transcripts (TRIzol, Invitrogen, Cat #15596018) or protein [radioimmunoprecipitation assay (RIPA) buffer].

Transcription Analysis by Quantitative RT-PCR

We chose day 10 for our transcriptional analysis with the prediction that gene expression changes might be more pronounced and potentially cumulative, reflecting the decrease in pericyte coverage. Endothelial cell and pericyte-enriched mRNA samples were extracted and purified using Quick-RNA MiniPrep kits (Zymo Research, Cat #R1055) following manufacturer instructions. Reverse transcription of mRNA to cDNA was achieved using SuperScript® VILO™ and RNase H reagents (Invitrogen Cat #11754-050 and #18021-071, respectively) and following manufacturer instructions. Quantitative RT-PCR was conducted in triplicate utilizing Taqman® Universal Master Mix II, with UNG (Life Technologies, Cat #4440038). "Best Coverage" murine Taqman® probes for gene expression analysis (Applied Biosystems, ThermoFisher) included primers for TATA binding protein (*Tbp*, for expression normalization) and the following targets: *Flt1*, *Dll4, Jag1, Notch1, Notch3, Hes1, Hey1, Hey2, HeyL, Pdgf-b, Perlecan/Hspg2,* and *Pdgfr*β. Samples were run in Standard 96-well plates on a QuantStudio6 Flex (Applied Biosystems, ThermoFisher), and results processed with QuantStudio Expression qRT-PCR software applying comparative ΔΔT method to determine expression changes.

Live Imaging of Ex Vivo Angiogenesis and Quantitative Movie Analysis

All animal experiments were conducted with review and approval from the Virginia Tech IACUC. All protocols were reviewed and approved by IACUC boards. The Virginia Tech

NIH/PHS Animal Welfare Assurance Number is A-32081-01 (expires 7/31/2021). Embryonic tissue culture assay (ETCA) experiments were conducted as previously described [50]. Briefly, following mating with *Flk1-eGFP; Ng2-DsRed* males, pregnant C57BL/6 female mice were sacrificed at embryonic day 14.5 (E14.5) by CO_2 inhalation and cervical dislocation. Embryos were retrieved from the uterus in 4ºC dissection media, and genotype was evaluated by fluorescence microscopy. Embryos positive for both *Ng2-DsRed* (i.e. pericyte signal) and *Flk1-eGFP* (i.e. endothelial cell signal) were selected for micro-dissection to isolate dorsal skin (i.e. tissue absent of Ng2+ glia). Dermal tissues were placed in single wells of a glass-bottom 6-well plate and embedded in a fibrin matrix with the hypodermis (subcutaneous layer) facing the glass. Basic culture media was added at 3 mL per well. The following day, spent media was replaced with culture media containing PBS (vehicle control) or VEGF-A (50 ng/ml, Peprotech, Cat #450-32). Plates were then transferred to an incubation chamber (37ºC, 5% CO_2, humidity controlled) mounted on a Zeiss LSM880 confocal microscope for live imaging. Multi-position, time-lapse confocal scans were acquired through each sample thickness (z-stacks: 6-8 images with 4-6 microns between planes) at 10-25 minute intervals for a minimum of 12 hours using a 20x objective. Each time point was compressed from the raw z-stack and exported as a video file in RGB channel format. Representative movie sequences shown are from non-consecutive images.

Movies of ex vivo blood vessel development in the ETCA experiments were analyzed for pericyte migration during control and VEGF-A-treated conditions. Pericyte migration was classified as persistent in a particular direction (“Directional Persistence”) or static without movement in a clear direction (“Static Movement”). In addition, *Ng2-*

DsRed+ pericyte distribution was evaluated at the beginning and end of each movie sequence by quantifying the number of neighboring pericytes within a 50-micron radius.

Embryonic Pericyte Culture on Immobilized Notch Ligands

In a separate study, Ng2-DsRed+ pericytes were isolated from embryonic mice at E12.5 and validated by standard approaches as well as in functional assays (see Online Resource 1 – Supplemental Materials and Methods) [59]. These cells were grown to confluence before enzymatic release and cultured on Notch ligand-coated plates. Ligand-coated plates were prepared by applying AffiniPure mouse anti-human IgG (Fcγ fragment specific, Jackson ImmunoResearch, Cat #209-005-098) to 10 cm^2 cell culture dishes (Corning, Cat #430167) overnight at 37°C. Plates were washed twice with PBS (10 mins / wash), and non-specific epitopes were blocked with 10% FBS (Gibco) in PBS for 2 hours at room temperature in a cell culture hood. This blocking solution was aspirated, and each plate was treated overnight at 37°C with PBS (control), 10% FBS in PBS blocking solution (serum block control), or 50 nM of one of the following: Human IgG only control (Fc fragment, Jackson ImmunoResearch, Cat #009-000-008), Recombinant rat Jagged-1-human IgG Fc chimera protein (R&D Systems, Cat #599-JG-100), or Recombinant mouse Dll4-human IgG Fc chimera protein (Adipogen, Cat #AG-40A-0145-C050). Plates were then washed twice with PBS (10 mins / wash), and pericytes were added to each plate condition in pericyte media. Media was replenished 3 days after plating, and mRNA was collected in lysis buffer after 2 more days (i.e. cultured in each condition for 5 days total). RNA isolation, reverse transcription, and qRT-PCR was conducted as described above,

applying the TaqMan probes (gene expression analysis) for: *Tbp*, *Hes1*, *Hey1, Hey2, HeyL, Notch1, Notch3,* and *Pdgfrβ.*

Protein Analysis

Western blot analysis was performed on cell lysates from MACS-enriched cell populations from ESC cultures differentiated for 10 days. Protein from ESC-derived endothelial cells and pericytes was collected in RIPA buffer. DC Protein Assay with Reagents A, S, and B (Bio-Rad) facilitated quantification of protein concentrations for each sample. Protein samples of equivalent concentration were separated by SDS-PAGE in standard running buffer (Bio-Rad) on 4-15% Mini PROTEAN® Pre-cast TGX gels (Bio-Rad, Cat # 456-1086). Separated proteins were transferred to Immobilon-FL PVDF Membrane for fluorescent and chemifluorescence (EMD Millipore, Cat # IPFL00010). Blocking solution [5% BSA in Tris-buffered solution with 0.1% Tween 20 (TBS-T)] was applied to membranes overnight at 4°C. Primary antibodies were incubated overnight at 4°C on a rotator. After washing 4x with TBS-T, secondary antibodies were incubated for 2 hours at room temperature. Following 4 washes with TBS-T, membranes were imaged on a ChemiDoc system (BioRad). Primary antibodies included: goat anti-Pdgfrβ (R&D Systems, Cat #AF1042) and rabbit anti-GAPDH (Abcam, Cat #ab9485). Recombinant Pdgfrβ (R&D Systems, Cat #1042-PR-100) was also run on a gel, transferred, and immunostained to validate primary antibody specificity. Secondary antibodies used were: donkey anti-goat AlexaFluor 488 (Jackson ImmunoResearch Cat #705-545-003), and donkey anti-rabbit AlexaFluor 647 (Jackson ImmunoResearch Cat #711-605-152) at

recommended dilutions. Relative protein levels were evaluated using BioRad Image Lab 5.1.

Pdgfrβ Isoform Characterization by PCR and Gel Electrophoresis

Targeted regions of cDNA derived from MACS-enriched An2+ pericyte samples were amplified via PCR using Taq Core Kit (Qiagen, Cat #201225). Amplicons were separated by gel electrophoresis using 2% agarose in Tris-acetate-EDTA buffer with SYBR Safe DNA gel stain (Invitrogen, Cat #S33102). Fragment bands were visualized by UV excitation. Primer sequences were designed using PrimerQuest, mapped in LaserGene, to target short fragments (<850bp) of mouse Pdgfrβ (*Mus musculus,* accession number NM_001146268).

	Forward	Reverse
Exons 1-5	5'- ACATCAGAAGCCATCTGTAGC-3'	5'-CGGATGGTGATGCTCTCG-3'
Exons 5-10	5'- GCAATGATGTGGTGAACTTCC-3'	5'- CGTTTCTAGCTGGCTCTCC3'
Exons 10-16	5'-TGGGAGGAAGATCAGGAATACG-3'	5'- CTCCTTTCATGTCCAACATGGG-3'
Exons 16-21	5'- CAAATACGCAGACATTGAGTCC-3'	5'- ATAGCCTTCACCCAGAAGC3'
Exons 21-23	5'- GAGGCTTCTGGGTGAAGG-3'	5'- GTAGAGCAATCCAGCTGAGG-3'

Statistics

Using GraphPad Prism 6 software, statistical analysis by Student's two-tailed t-test was applied to pericyte coverage and distribution measurements as well as to pericyte migration and distribution measurements from ETCA live imaging observations. Relative changes in gene expression (as quantified by qRT-PCR) were analyzed statistically using pair-wise Student's two-tailed t-tests. P-values less than or equal to 0.05 were considered significant.

RESULTS

Pericyte coverage and distribution depend on *Flt1* expression during early blood vessel formation.

Flt1 provides essential regulation of VEGF-A signaling to coordinate a range of endothelial cell behaviors during discrete stages of blood vessel branching [11,50,60,61]. Recent studies have suggested that, in addition to its unique roles in a variety of angiogenic contexts [62-65], Flt1 may directly or indirectly impact vascular mural cells during blood vessel maturation [27,28,66-68]. Here, we hypothesized that a VEGF-A gain-of-function, through genetic loss of *Flt1*, disrupts mechanisms facilitating pericyte-endothelial crosstalk such that early pericyte coverage and distribution along newly forming vessels are also impaired. Mouse embryonic stem cells (ESCs) give rise to numerous cell types when differentiated in the absence of specific cues to induce a particular lineage [56]. Endothelial cells organize into primitive vessel-like structures and ramify into larger networks through initial vasculogenic coalescence, subsequent angiogenic sprouting and anastomosis, and ultimately lumen formation, comparable to the progression of vascular development seen *in vivo* [69]. We observed ESC-derived vessels

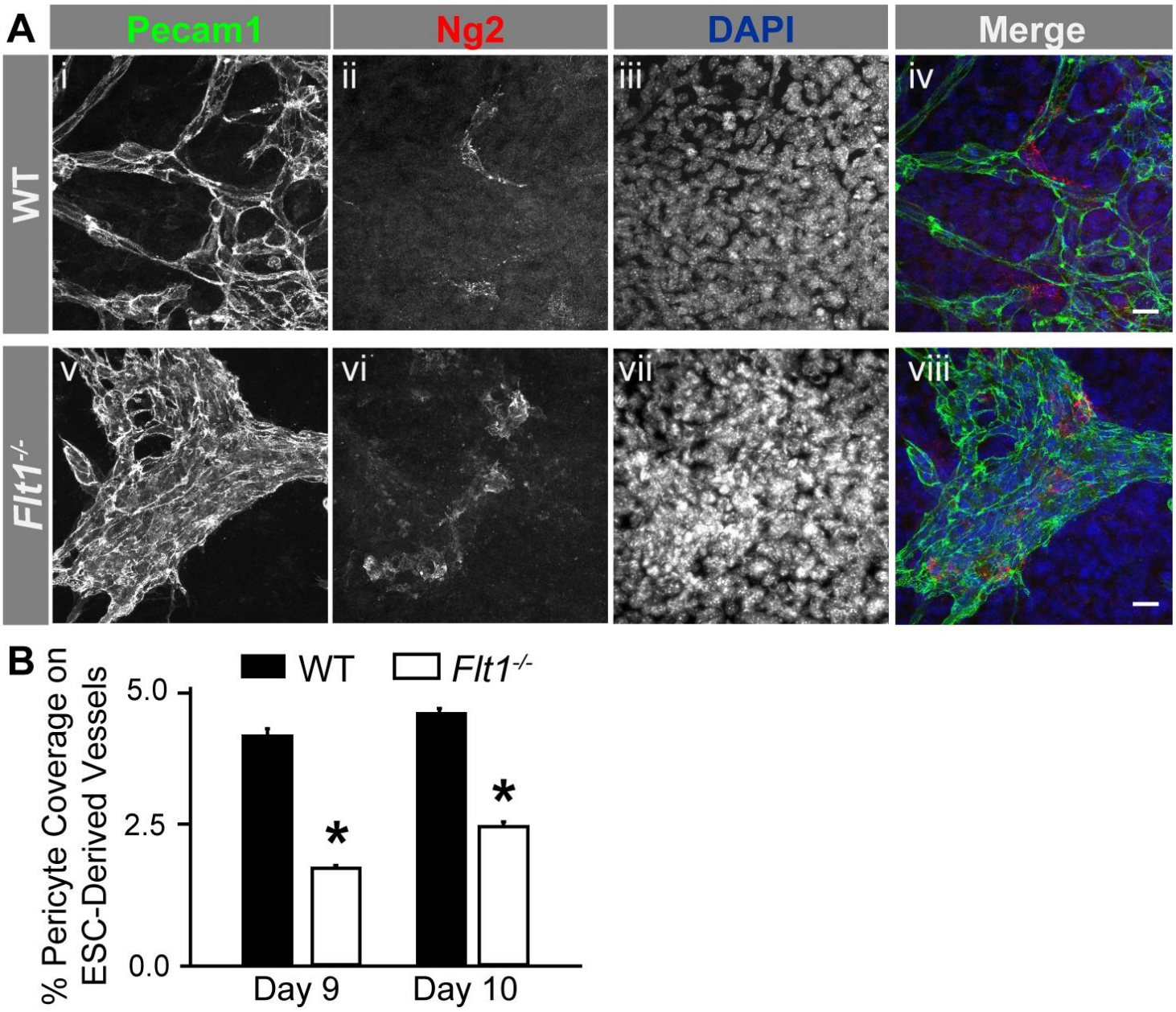

Fig. 1 Genetic loss of *Flt1* impairs Ng2+ pericyte coverage of ESC-derived blood vessels. **A** Representative images of WT (i-iv) and *Flt1*$^{-/-}$ (v-viii) Day 9 ESC-derived blood vessels labeled for endothelial cells (Pecam1: i and v, green in iv and viii), pericytes (Ng2: ii and vi, red in iv and viii), and cell nuclei (DAPI: iii and vii, blue in iv and viii). Scale bars, 50 μm. **B** Average percentages of Ng2+ pericyte coverage on Days 9 (n=6 of biological replicates) and 10 (n=10 of biological replicates) ESC derived vessels for WT (black bars) and *Flt1*$^{-/-}$ (white bars) conditions. Values are averages + Standard Error of the Mean (SEM). *P≤0.05 vs. WT at the same time point

in WT and *Flt1*$^{-/-}$ cultures via immunostaining for platelet-endothelial cell adhesion molecule-1 (Pecam1) 8-10 days after the start of differentiation. *Flt1*$^{-/-}$ ESC-derived vessels were overgrown and poorly branched as compared to WT vessels (Figure 1), consistent with previous observations from this model [9,11,50,61]. *Flt1*$^{-/-}$ ESC-derived vessels also suffer from elevated and aberrant Flk1 phosphorylation and activation, as previously shown [9,50-53]. To identify vascular pericytes within these networks, we selected neural glial antigen-2 (Ng2; chondroitin sulfate proteoglycan-4, Cspg4) as our target for immunolabeling (Figure 1). This molecule is a well-accepted marker for pericytes [70], is only expressed by other cell types such as oligodendrocyte precursors (OPCs) at later stages of development [71], and poses fewer challenges in cell type identification as compared to labels such as alpha-smooth muscle actin (aSMA; Acta2) and Desmin (Des) [70]. In WT vessels, Ng2+ pericytes were prevalent at vessel branch points, as often observed *in vivo* [72], as well as along vessel lengths and thicker vessels (Figures 1 and 2). In contrast, pericytes on *Flt1*$^{-/-}$ vessels were less numerous, exhibiting a significant reduction in overall vessel coverage and particularly at branch point and vessel length locations (see Online Resource 2 – Supplemental Figure 1 for additional representative images of distinct morphological locations for each genotype). Pericytes in the WT context steadily became more widespread over time (Figures 1 and 2), as their density within a 50-micron radius of one another steadily decreased. This shift in pericyte distribution may reflect recent observations of pericytes establishing their own unique “domains” of vessel coverage and avoiding spatial overlap [73]. Changes in pericyte density along *Flt1*$^{-/-}$ vessels were however more variable over time and displayed a later-stage trend towards increased accumulation i.e. more pericytes within a 50-micron radius of each other (Figure 2). To exclude the potential involvement of Placental Growth Factor

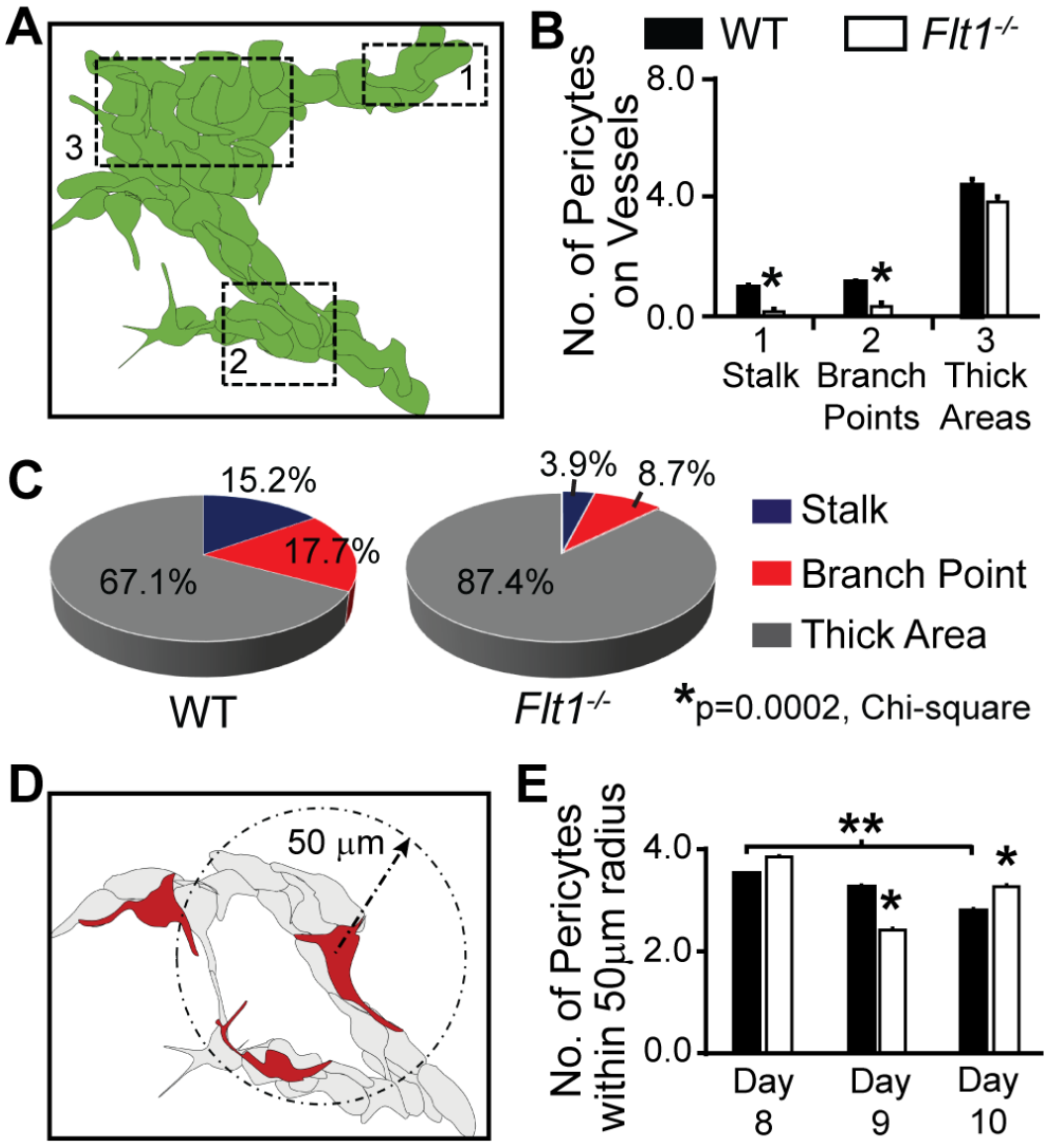

Fig. 2 *Flt1*$^{-/-}$ ESC-derived vessels display defects in pericyte distribution. **A** Schematic of ESC-derived vasculature with specific morphological locations denoted with dotted boxes: 1- vessel stalks, 2- branch points, and 3- thick areas. **B** Average number of Ng2+ pericytes at the indicated vessel locations within Day 9 WT (black bars, n=23 cells) and *Flt1*$^{-/-}$ (white bars, n=28 cells) ESC-derived vasculature. Values are averages + SEM. *P≤0.05 vs. WT at the same vessel location. **C** Percent distribution of pericytes at each vessel location (stalk: blue, branch point: red, thick area: gray) for Day 9 WT and *Flt1*$^{-/-}$ vessels (WT: n=158 cells, and *Flt1*$^{-/-}$: n=127 cells). *P=0.0002, Chi-square test of WT and *Flt1*$^{-/-}$ distributions. **D** Schematic of approach to quantifying pericyte density, specifically pericytes within a 50 μm radius of one another (dashed arrow and circle). **E** Average number of Ng2+ pericytes within a 50 μm radius of one another on Day 8-10 WT (black bars, Day 8: n=7, Day 9: n=23, Day 10: n=56) and *Flt1*$^{-/-}$ (white bars, Day 8: n=18, Day 9: n=28, Day 10: n=53) ESC-derived vessels. Values are averages + SEM. *P≤0.05 vs. WT at Day 9 and Day 10, and **P≤0.05 for Day 8 WT vs. Day 10 WT.

(PlGF) and VEGF-B, which can also bind to Flt1 [74], we exposed WT ESC-derived vessels to ectopic VEGF-A and found a similar reduction in pericyte coverage (Online Resource 1 for experimental details, and Online Resource 3 – Supplemental Figure 2 for results). Taken together, these observations suggest that the loss of Flt1 activity and a gain-of-function for VEGF-A impairs pericyte distribution along nascent vessels such that pericyte coverage cannot match new vessel growth, likely due to direct effects on endothelial cell signaling that lead to a disconnect in mechanisms underlying pericyte-endothelial crosstalk.

Pericytes along nascent ESC-derived vessels lack *Flt1* expression.

Based on our observation of disrupted pericyte coverage and distribution on *Flt1*$^{-/-}$ vessels, we then tested the hypothesis that, in addition to endothelial cells [61], pericytes might also express *Flt1*, and their behavior may be directly affected by this genetic deletion. *Flt1* expression by vascular pericytes and mural cells remains an open question in the field, with contrasting observations across various models [27-33]. Our *Flt1*$^{-/-}$ ESCs express the *LacZ* reporter gene under the control of the endogenous *Flt1* promoter, thus providing a means to observe which cells actively express the *Flt1* gene. Immunostaining ESC-derived vessels for β-galactosidase, the product from the *Flt1-LacZ* gene, along with Ng2 labeling, demonstrated that Ng2+ pericytes had little to no *Flt1* gene activity relative to neighboring endothelial cells (Figure 3 and Online Resource 4 – Supplemental Figure 3). To further test for pericyte expression of *Flt1*, we used magnetic-activated cell sorting (MACS) to isolate and enrich for WT pericytes and endothelial cells from day 10 ESC-derived vessels, as described previously [11,75]. Using qRT-PCR for gene expression analysis, we found that WT pericyte expression of *Flt1* was significantly lower relative to

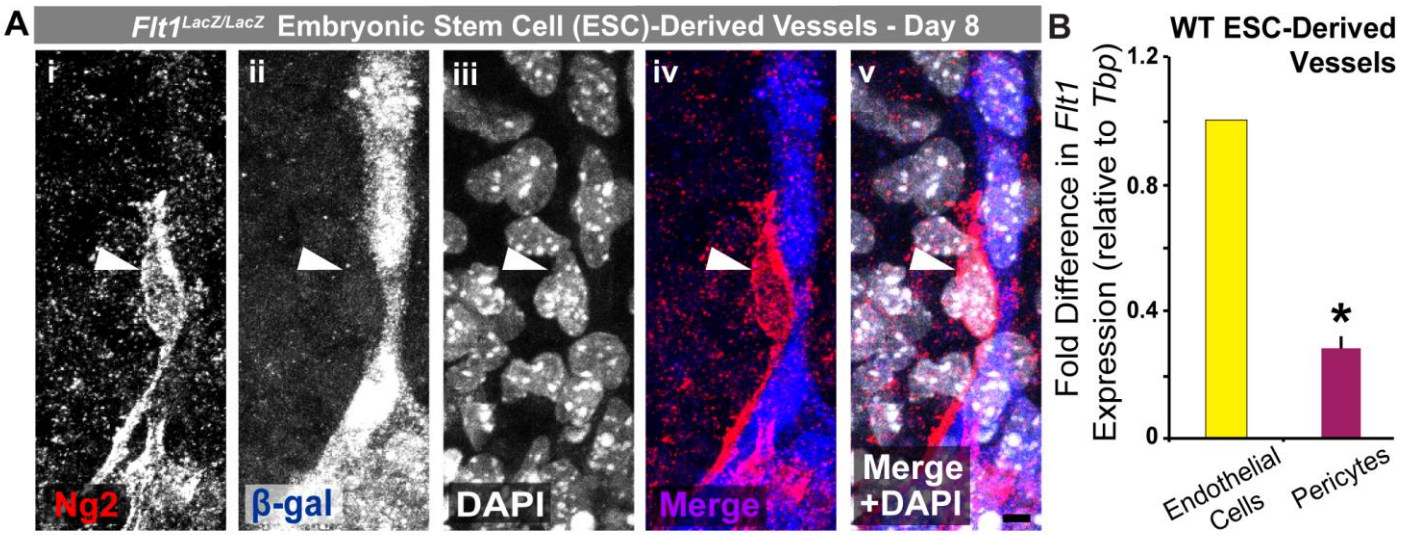

Fig. 3 ESC-derived pericytes display little to no *Flt1* promoter activity or gene expression. **A** Representative images of Ng2+ pericytes (Ng2: i, red in iv and v) and *Flt1* promoter activity as indicated by β-galactosidase (β-gal: ii, blue in iv and v) production from the *Flt-1:LacZ* gene. Cell nuclei are labeled by DAPI (iii, white in v). Scale bar, 5 μm. **B** Fold change in *Flt1* expression between endothelial cells (yellow bar) and pericytes (purple bar) enriched from WT ESC-derived vessels. Values are averages + SEM, n=4 biological replicates. *P≤0.05

WT endothelial cells in our differentiated ESCs (Figure 3 and Online Resource 4 – Supplemental Figure 3). Additional analysis of *Flk1/Kdr* (VEGF Receptor-2, VEGFR2) expression revealed that WT ESC-derived pericytes have little to no expression of this VEGF receptor relative to endothelial cells, which was verified further using our recently derived embryonic pericyte cell line (see Online Resource 4 – Supplemental Figure 3). Our data suggest that pericytes do not express appreciable levels of *Flt1* or *Flk1*, if any, during the early stages of vessel formation that we observed within our model. These results are consistent with previous observations from other developing vascular beds [29-33], though pericyte *Flt1* expression may potentially be stage or model specific [27,28]. Furthermore, these observations suggest that *Flt1* loss likely results in direct disruption of endothelial cell signaling and that downstream effects on pericyte dynamics

and coverage presumably occur indirectly, as pericytes express few to no VEGF receptors and therefore are unlikely to experience relevant levels of VEGF-A signaling.

Excess VEGF-A limits pericyte distribution by disrupting pericyte migration along sprouting endothelial cells.

Increased pericyte clustering, along with reduced pericyte coverage and distribution on developing *Flt1*$^{-/-}$ vessels, suggested that limited pericyte migration might be one of the primary defects caused indirectly by the loss of Flt1 regulation of the VEGF-A signaling in endothelial cells. To test this idea, we utilized an *ex vivo* model of early vessel formation that permitted real-time observation of pericyte and endothelial cell dynamics in the angiogenic context, as described previously [50]. Specifically, we used time-lapse confocal imaging to observe *Flk1-eGFP*+ endothelial cells and *Ng2-DsRed*+ *(Cspg4-DsRed+)* pericytes within the developing vasculature of explanted mouse embryonic skin [embryonic day 14.5 (E14.5)]. Angiogenic sprouting of *Flk1-eGFP*+ endothelial cells occurred during vehicle control treatment, with more robust sprouting observed in the VEGF-A-treated cultures (Figure 4). Additional analysis confirmed this increase in endothelial cell sprouting and revealed a net decrease in vessel branching for cultures exposed to ectopic VEGF-A (see Online Resource 5 – Supplemental Figure 4). Although no statistically significant differences were detected, these results were consistent with previous observations of *Flt1*$^{-/-}$ vessel dysmorphogenesis and the accumulation of remodeling defects [9,11,50,76]. Under vehicle control conditions, pericytes associated with sprouting endothelial cells migrated in a persistent manner towards the direction of the extending sprout. In contrast, ectopic VEGF-A caused pericyte migration to become more static and randomized and much less directed towards endothelial cell sprouting

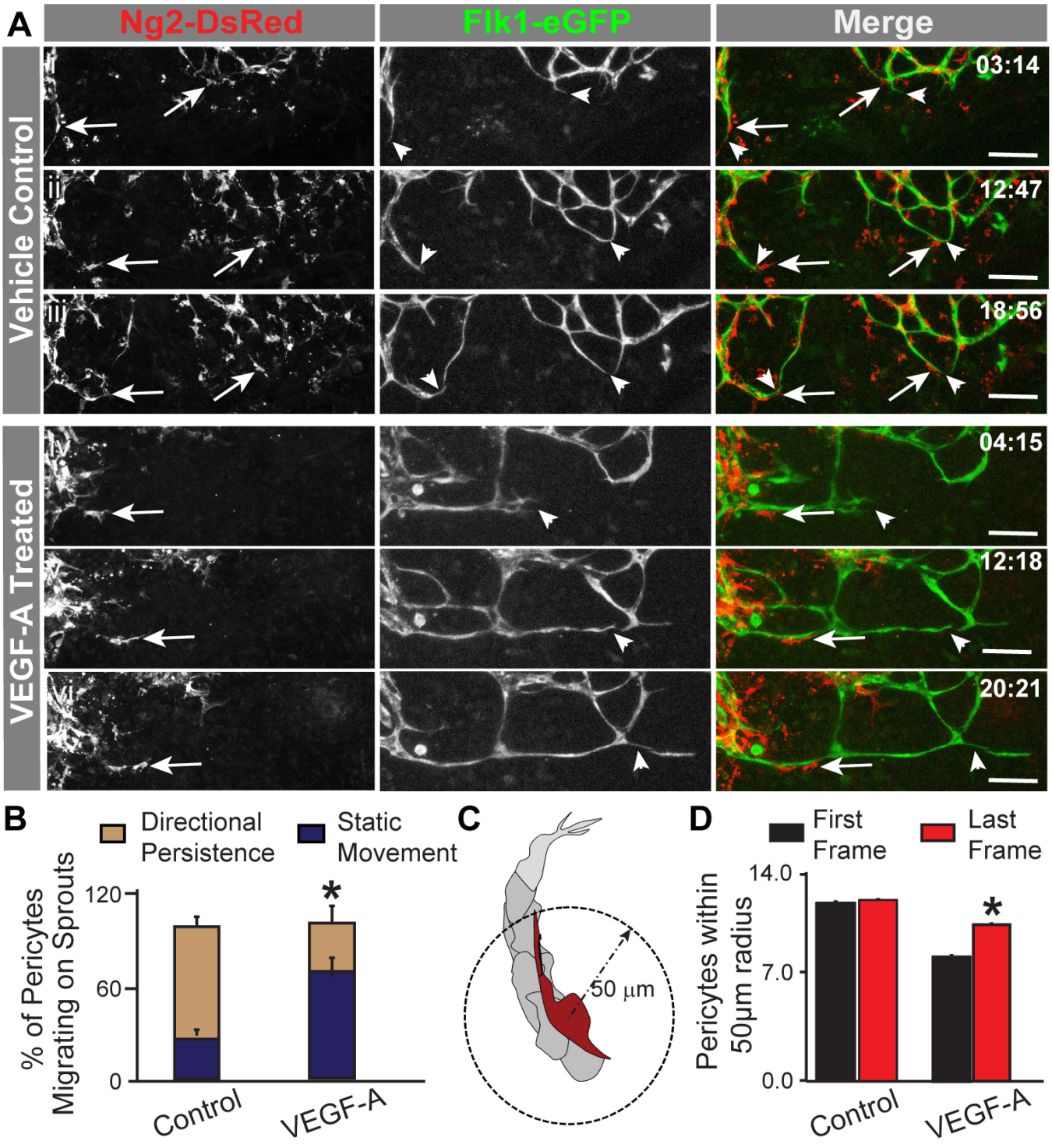

Fig. 4 Exogenous VEGF-A disrupts pericyte migration and limits pericyte distribution on developing embryonic blood vessels. **A** Representative sequential images from movies of vehicle control- (i-iii) and VEGF-A- (iv-vi) treated embryonic skin vessels in which endogenous pericytes (Ng2-DsRed+ and arrows, left column and red in right column) migrated along sprouting endothelial cells (Flk1-eGFP+ and arrowheads, middle column and green in right column). Time in upper right corner, hours:minutes (hh:mm). Scale

bars, 100 μm. **B** Average percent of pericytes migrating on sprouts with directional persistence (tan bars) or static movement (dark blue bars) in control (n=23 movies) and VEGF-A-treated (n=15 movies) embryonic vessels. Values are averages + SEM. *P≤0.05. **C** Schematic of approach to quantifying pericyte density, specifically pericytes on sprouting endothelial cells within a 50 μm radius of one another (dashed arrow and circle). **D** Average number of Ng2-DsRed+ pericytes within a 50 μm radius of one another in the first (black bars) and last (red bars) frames of movies from control (n=6 biological replicates) and VEGF-A-treated (n=4 biological replicates) embryonic vessels. Values are averages + SEM. *P≤0.05 vs. First Frames of VEGF-A-treated group

and anastomotic connection events (Figure 4). VEGF-A-induced defects in pericyte migration were also reflected in the observation that pericyte density within a 50-micron radius increased from the first movie frame to the last (Figure 4). These data further highlight that mis-regulated VEGF-A signaling stunts pericyte coverage and distribution likely by severing the crosstalk among mechanisms coordinating endothelial cell formation of new vessels with pericyte expansion along a developing vascular network.

Loss of *Flt1* leads to dysregulated gene expression in the Notch and PDGF-B pathways.

During the initial stages of sprouting angiogenesis, endothelial cells integrate VEGF-A signals with cues received from neighboring endothelial cells, primarily via the Notch pathway [11-13], to establish an emerging “tip” cell and proliferative “stalk” cells. As the endothelial “tip” cell migrates outward from an existing vessel, it up-regulates production of PDGF-B [14,16,15], which is localized in the surrounding extracellular matrix (ECM) by heparin sulfate proteoglycans (HSPGs) [16,77,78]. We therefore hypothesized that losing Flt1 regulation of VEGF-A activity in endothelial cells leads to mis-regulation within the Notch and PDGF-B pathways; these gene expression defects in turn likely contribute to impaired pericyte-endothelial cell crosstalk and potentially lead indirectly to the observed

reduction in pericyte coverage. As described above, we used MACS to obtain endothelial cells and pericytes from day 10 WT and *Flt1*$^{-/-}$ ESC-derived vessels. Gene expression analysis by qRT-PCR revealed that, as reported previously [11], *Flt1*$^{-/-}$ endothelial cell expression of the Notch ligand *Dll4* was significantly increased, as were the downstream Notch-regulated transcription factors *Hes1*, *Hey1*, and *Hey2* (Figure 5). Transcripts for the Notch receptors *Notch1* and *Notch3* and the transcription factor *HeyL* were unchanged in *Flt1*$^{-/-}$ endothelial cells, which aligns with previous reports from various populations of endothelial cells exposed to excess VEGF-A [79]. In addition, we observed a significant decrease in endothelial expression of *Jagged1 (Jag1)* in *Flt1*$^{-/-}$ vessels, suggesting a down-regulation of this Notch ligand that has been implicated in mediating endothelial cell-mural cell crosstalk [4,38,34,35]. In contrast, *Flt1*$^{-/-}$ pericytes showed no significant changes in Notch pathway gene expression, though *Notch1*, *Hey1*, and *HeyL* displayed trends towards increased expression (Figure 5). In exploring the PDGF-B pathway, we found that expression levels of the ligand *Pdgfb* and the associated anchoring protein *Hspg2* (*Perlecan*) were significantly increased in *Flt1*$^{-/-}$ endothelial cells relative to WT, consistent with previous observations of endothelial cells in elevated VEGF-A environments [14]. Interestingly, we found that pericytes from *Flt1*$^{-/-}$ ESC-derived vessels had decreased expression of *Pdgfr*β (PDGF Receptor-β gene) relative to WT pericytes. Collectively, these observations demonstrate that the genetic loss of *Flt1*, which is known to disrupt VEGF-A signaling in endothelial cells [9], has downstream effects on the Notch and PDGF-B pathways, likely disrupting signals that intersect or contribute indirectly to regulating pericyte coverage of developing blood vessels.

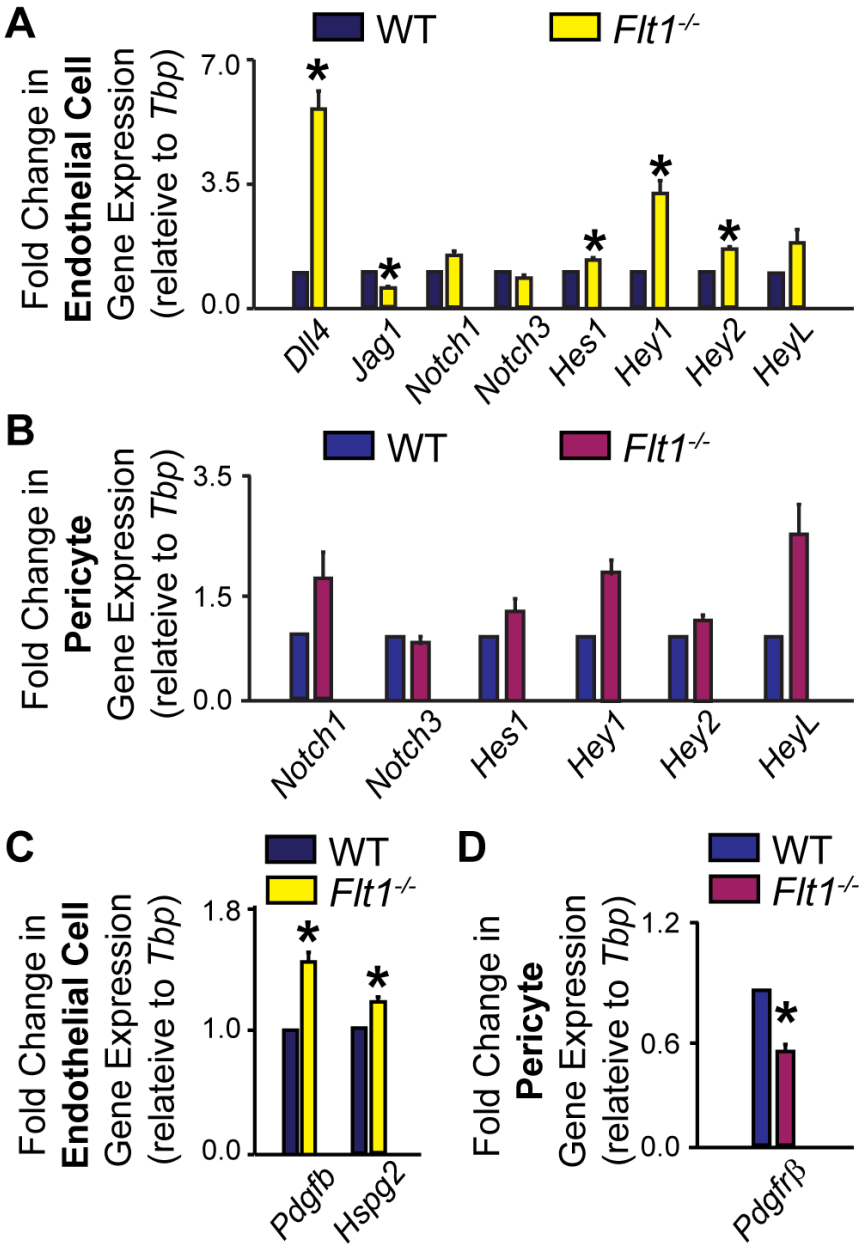

Fig. 5 Loss of *Flt1* disrupts transcriptional regulation within the Notch and PDGF-B pathways. **A** Fold change in Notch pathway gene expression between WT (dark blue bars) and *Flt1*$^{-/-}$ (yellow bars) endothelial cells enriched from ESC-derived vessels. Values are averages + SEM, n=4-8 biological replicates per gene. *P≤0.05 vs. WT. **B** Fold change in Notch pathway gene expression between WT (blue bars) and *Flt1*$^{-/-}$ (purple bars) pericytes enriched from ESC-derived vessels. Values are averages + SEM, n=4-8 biological replicates per gene. **C** Fold change in PDGF-B pathway gene expression between WT (dark blue bars) and *Flt1*$^{-/-}$ (yellow bars) endothelial cells enriched from ESC-derived vessels. Values are averages + SEM, n=4-8 biological replicates per gene. *P≤0.05 vs. WT. **D** Fold change in *Pdgfrβ* expression between WT (blue bars) and *Flt1*$^{-/-}$ (purple bars) pericytes enriched from ESC-derived vessels. Values are averages + SEM, n=4-8 biological replicates per gene. *P≤0.05 vs. WT

Pericytes produce a truncated PDGFRβ isoform during ESC-derived vessel formation.

Recent evidence suggests that vascular pericytes differentially regulate PDGFRβ depending on the particular microenvironment, such as during hypoxia, nutrient deprivation, or increased cell proliferation [44-47,55], consistent with our own data from the developing postnatal mouse brain (J. Darden and C. Jenkins-Houk, unpublished data). In observing altered *Pdgfrβ* transcriptional regulation in *Flt1*$^{-/-}$ ESC-derived pericytes, we hypothesized that these PDGFRβ isoforms, which may arise independent of Notch signaling [45], might be the more predominant PDGFRβ species in our ESC-derived vessels. To test this hypothesis and concurrently assess the relationship between PDGFRβ transcriptional changes and protein levels, we dissociated day 10 WT and *Flt1*$^{-/-}$ ESC-derived vessels, enriched for pericyte and endothelial populations using MACS as described above, and collected protein for Western Blot analysis. After using recombinant PDGFRβ to validate that our antibody was capable of detecting this protein (Figure 6), we applied this PDGFRβ antibody to detect PDGFRβ isoforms and their respective levels in each of our cell populations under WT and *Flt1*$^{-/-}$ conditions. Interestingly, we found an ~60 kDa PDGFRβ isoform present in both WT and *Flt1*$^{-/-}$ pericyte populations, with *Flt1*$^{-/-}$ pericytes containing around 3-fold less full-length PDGFRβ and this PDGFRβ isoform compared to WT pericytes (Figure 6).

In observing the differential regulation of this PDGFRβ isoform, we next asked how this isoform might be generated such as through alternative splicing on the mRNA level or post-translational cleavage as suggested by several previous studies [44-47]. We examined pericyte cDNA derived from ESC-derived vessel lysates for the presence of

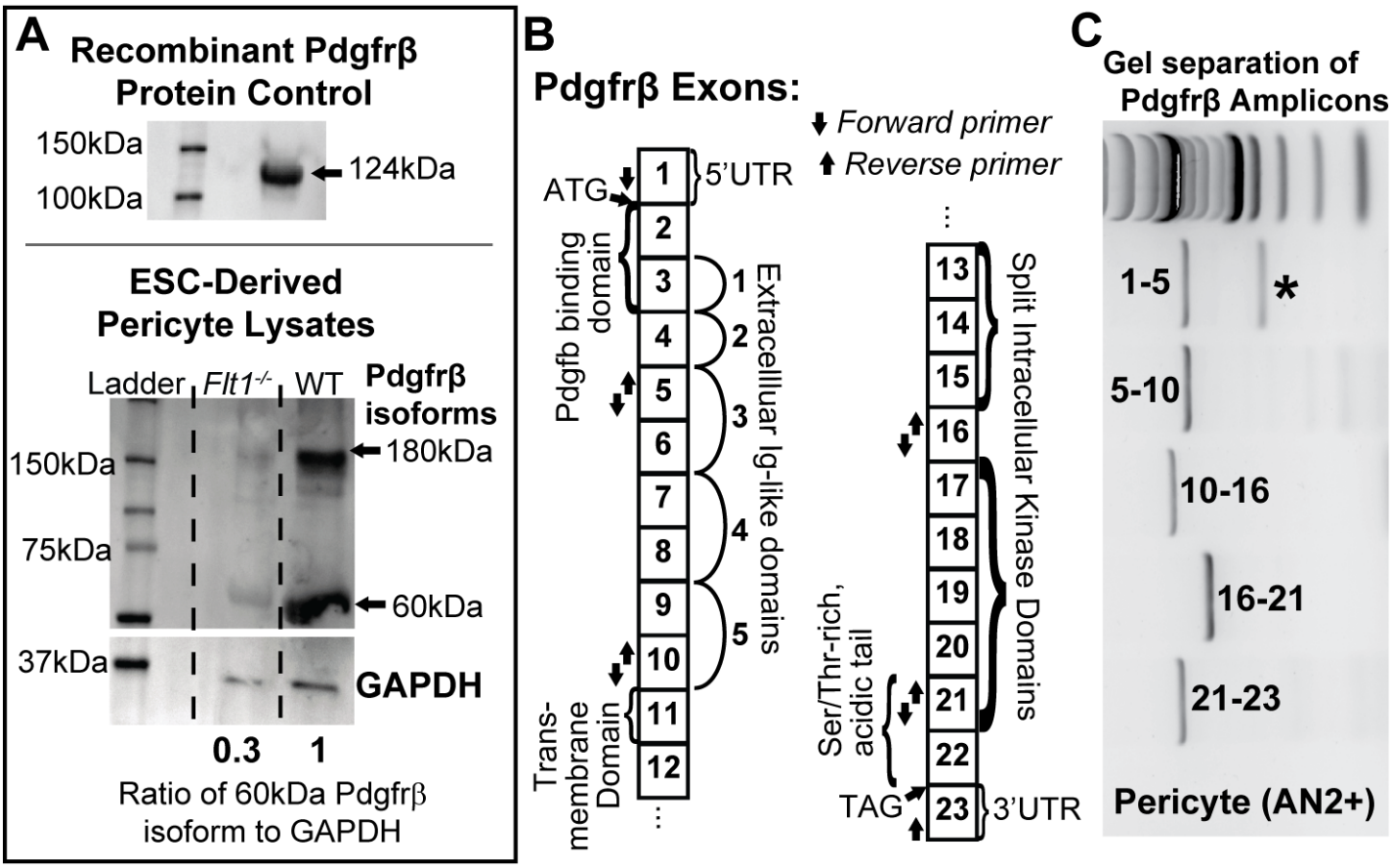

Fig. 6 *Flt1*$^{-/-}$ pericytes produce less PDGFRβ than WT pericytes, and pericytes in both backgrounds produce a truncated PDGFRβ isoform. **A** Representative images of Western Blots of recombinant PDGFRβ protein (top, antibody validation) and lysates from ESC-derived pericytes (bottom). Full-length (~180 kDa) and truncated (~60 kDa) isoforms of PDGFRβ were detected in WT and *Flt1*$^{-/-}$ pericyte lysates, and GAPDH (loading control) was used to normalize and compare relative amounts of full-length PDGFRβ (0.29) and this truncated isoform (0.34) between groups. n=4 biological replicates. **B** Map of *Pdgfrβ* exons with important features denoted as well as arrows indicating the location of forward and reverse primers used to identify potential mRNA splice variants. **C** Representative image of *Pdgfrβ* amplicons separated on an agarose gel. Number ranges indicate PCR products within indicated primer sets. * indicates the presence of a potential mRNA splice variant.

alternative splice variants. Specifically, we designed primer sets to amplify short, multiple exon-spanning regions of the complete, full-length *Pdgfrβ* transcript. PCR amplification with primers spanning exons 1-5 produced two distinct bands when separated by gel electrophoresis, with migration bands corresponding to the expected ~730bp (full-length PDGFRβ) and a smaller ~370bp. All other PCR fragments yielded a single band of expected size. This indicates an alternative splice variant that is modified within the first 5 exons of PDGFRβ, likely coding for a shorter N-terminus or a skipped exon. This is consistent with a human PDGFRβ transcript variant that yields a shorter N-terminus (accession number NM_001355016). Sanger sequencing of these bands indicated skipping of exons 2 and 3 in the smaller band, which corresponds to loss of the PDGF-B binding domain of the transcribed protein (Figure 6). Functional relevance of such a splicing event suggests loss of PDGF-B ligand binding, although more extensive analyses on the protein and mRNA levels are needed. However, this spice variant (shorter by ~360bp) does not correspond to a ~60kDa translated protein. While the primer sets tested would likely detect a shorter mRNA variant due to exon skipping, they may not detect a truncated 3'-end variant. Therefore, the shorter protein isoform observed may be due a truncated transcript or translational cleavage. Further investigation is needed to determine the exact mechanism. Hutter-Schmid and Humpel (2016) demonstrate that cleavage modifications may actually be PDGF-B-dependent, consistent with *Pdgfb* transcriptional changes described above (Figure 5).

Embryonic pericytes respond to stimulation by immobilized Dll4 but not Jag1, but neither ligand induces changes in *Pdgfrβ* transcription.

Pericytes and smooth muscle cells engage in Notch signaling across a range of developmental contexts to promote their differentiation and augment overall vessel maturation [4,38,34,35,37]. While Notch signals have been implicated in pericyte recruitment through regulation of *Pdgfrβ* expression [38,39], not all Notch pathway manipulations alter pericyte *Pdgfrβ* expression and impair pericyte coverage [35,36]. Observing lower *Jag1* expression in *Flt1*$^{-/-}$ endothelial cells and a concomitant decrease in *Pdgfrβ* expression in *Flt1*$^{-/-}$ pericytes suggested that Jag1 might regulate pericyte PDGFRβ in our model. Thus, a loss of Jag1 stimulation might impair embryonic pericyte migration and recruitment via reduced PDGFRβ activity. We tested this hypothesis using a functionally validated pericyte cell line recently derived in our lab from embryonic day 12.5 (E12.5) mice harboring the *Ng2-DsRed* reporter gene [59]. To stimulate Notch signaling in these embryonic pericytes, we cultured them on substrates of immobilized Dll4 or Jag1 as previously described [80-82], as well as on control substrates (untreated plate, Fc-γ with blocking serum only, and Fc-γ with human IgG, Fc fragment). Pericytes stimulated by immobilized Dll4 displayed significant increases in the downstream Notch targets *Hey1*, *Hey2*, and *HeyL* (notably a more than 35-fold increase), though not *Hes1*, and *Notch1* receptor transcription was also up-regulated (Figure 7). Jag1 ligands influenced pericyte transcription levels of downstream Notch targets, though statistically significant changes were not detected, and neither Dll4 nor Jag1 induced any changes in *Pdgfrβ* transcription. These results indicate that Dll4, but not Jag1, can stimulate Notch signaling in embryonic pericytes, but neither Notch ligand induces increased *Pdgfrβ* gene expression in these pericytes. To gain further insight into the potential role, or lack thereof, for Notch signaling in regulating pericyte coverage during early vessel formation, we exposed our WT and

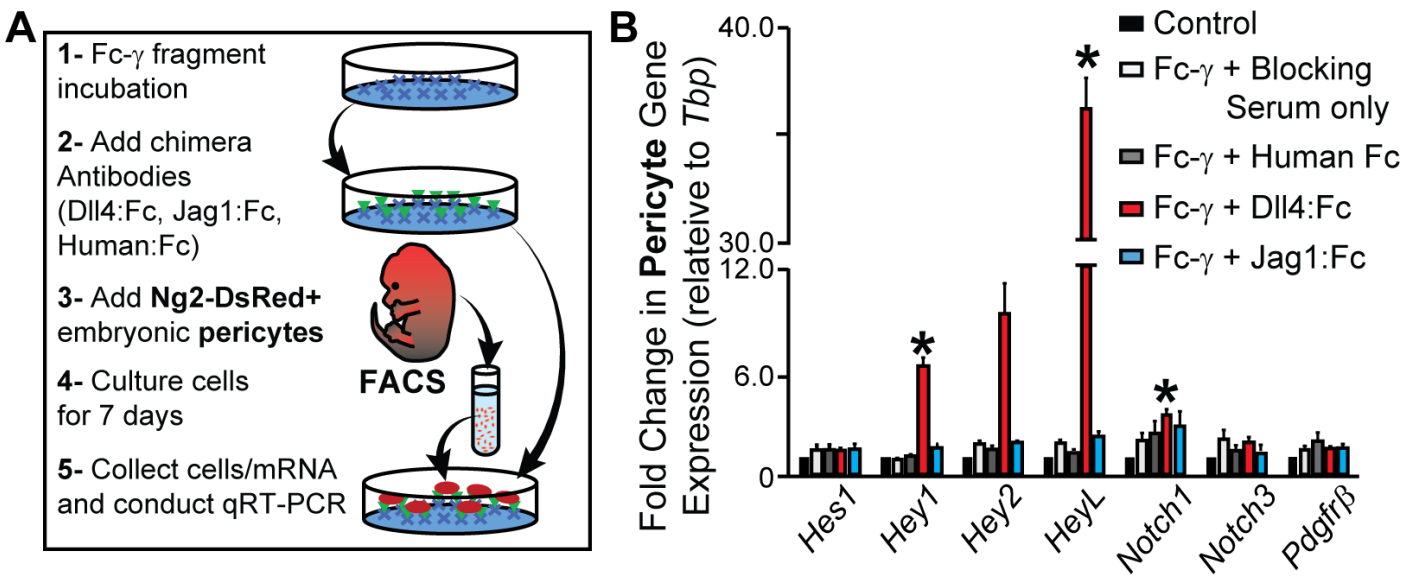

Fig. 7 Immobilized Dll4, but not Jag1, induces changes in embryonic pericyte gene expression, but neither ligand alters *Pdgfrβ* expression. **A** Schematic of experimental setup for coating plates with Notch or control ligands, deriving Ng2-DsRed+ embryonic pericytes, and cultures these cells on Notch ligands to measure changes in gene expression. **B** Fold change in *Pdgfrβ* and Notch pathway gene expression between embryonic pericytes cultured under control conditions (black bars), exposed to Fc-γ and blocking serum only (white bars), on Fc-γ with Human Fc (gray bars), on Fc-γ with Dll4:Fc (red bars), or on Fc-γ with Jag1:Fc (light blue bars). Values are averages + SEM, n=5 biological replicates. *P≤0.05 vs. control conditions for specified gene target.

Flt1$^{-/-}$ ESCs to a Notch inhibitor during vessel formation (see Online Resource 1 – Supplemental Materials and Methods). We found that Notch inhibition had no effect on pericyte coverage in either background (see Online Resource 6 – Supplemental Figure 5), further supporting the notion described in previous studies [35,37] that, at early stages in vessel development, pericyte coverage may not require Notch signaling.

DISCUSSION

Pericytes are critical components in the maturation of developing blood vessels into stable, higher-order vascular networks. In the current study, we show that mis-regulated VEGF-A signaling in endothelial cells indirectly compromises pericyte distribution and coverage along developing embryonic vessels, in part, by limiting pericyte migration. Defective VEGF-A regulation perturbed the Notch and PDGF-B pathways in both endothelial cells and pericytes, though direct stimulation of embryonic pericytes with Notch ligands did not affect *Pdgfrβ* expression. Interestingly, the indirect reduction in pericyte PDGFRβ that occurred with disrupted endothelial VEGF-A signaling was also detected on the protein level, that is, decreased levels of both full-length and truncated PDGFRβ isoforms. These PDGFRβ isoforms have been identified in unique biological contexts [44-47,55], and their relative abundance appears to be dependent on PDGF-B levels and proteolytic cleavage events [45], which is consistent with results from the current study. Taken together and summarized in Online Resource 7 – Supplemental Figure 6, these observations suggest pericyte coverage of developing vessels requires precise coordination of endothelial VEGF-A signaling, as this pathway provides important downstream regulation of pericyte distribution via PDGF-B-PDGFRβ activity, in a seemingly Notch-independent manner during early developmental stages.

Pericytes perform a broad range of functions in modulating blood vessel formation and remodeling [83-85], with new roles still being discovered [86,87]. Pericytes have been shown to directly and indirectly regulate VEGF-A signaling during vascular development, in part, via production of the VEGF receptor Flt1 [66,27,67,68], though this regulation appears to be largely context dependent [28-32]. Our expression analysis of pericytes within ESC-derived vasculature indicated that these cells lack *Flt1* and *Flk1* expression

levels comparable to that of endothelial cells at early embryonic time points. In another developmental model, a similar *in vivo* analysis of *Flt1* promoter activity [i.e. *Flt1*$^{lacZ/+}$ gene yielding β-galactosidase (β-gal)] in the developing postnatal retina revealed an expression pattern consistent with our current findings, as little to no β-gal signal was detected in perivascular cells [Ref. [61], and J. Chappell, unpublished data]. Because pericyte expression of *Flt1* and *Flk1* may be significantly lower relative to endothelial cells [27], additional analysis may be necessary to incorporate methods with enhanced sensitivities for Flt1 and Flk1 production and activity. Additionally, pericyte Flt1 may be more abundant at later developmental stages or in disease-specific contexts [28,31], beyond the early stages of vascular development that we observed herein. Thus, the apparent context-dependence for Flt1 synthesis from pericytes warrants further investigation to establish if this mode of VEGF-A regulation might be a potential therapeutic target in certain disease states.

Following their recruitment to the abluminal surface of developing vessels, perivascular cells migrate along the vasculature to establish sufficient coverage of the emerging vascular network [88,73]. Angiogenic endothelial cells secrete several molecular cues that modulate pericyte migration along the endothelium including PDGF-B, among others. For instance, Angiopoietin-2 (Angpt2) over-expression can induce pericyte migration off existing and remodeling vasculature [89], while Angpt1 promotes more stable interactions of pericytes with endothelial cells [90-92]. The Angpt-Tie pathway may also intersect with heparin-binding EGF-like growth factor (HB-EGF) signaling [93], presumably through Erb1 and Erb4 receptors [94], to coordinate pericyte recruitment and subsequent migration along developing vessels. While our current data

demonstrate how Flt1 regulation of VEGF-A influences downstream PDGF-B-PDGFRβ dynamics and subsequent pericyte coverage, we cannot rule out the influence of secondary effects from vessel dysmorphogenesis or the likely intersection(s) among a number of these collateral pathways, including the Angpt-Tie pathway [95]. In fact, additional transcriptional profiling and image analysis revealed that, in our ESC-derived vessel model, VEGF-A mis-regulation disrupted synthesis of important extracellular matrix (ECM) components such as Type IV Collagen (J. Darden and H. Zhao, unpublished data), which may play a critical role in pericyte migration dynamics. Additional studies are therefore essential for dissecting the unique contribution of these and other factors in regulating pericyte-endothelial cell interactions during the early stages of vessel formation as well as during vascular maturation.

The Notch pathway has emerged as a convergence point for many signaling pathways, most notable is the crosstalk with VEGF-A signaling in endothelial cells during sprouting angiogenesis [11-13]. Notch signaling in mural cells is also critical for vascular development, as disrupting Notch cues such as Jagged1 and Notch3 can compromise smooth muscle cell differentiation and investment [96,35,37]. Pericytes also appear to experience Notch signaling, though the downstream effects of Notch perturbations on pericytes are somewhat unclear, with pericyte *Pdgfrβ* expression and vessel coverage being affected in certain contexts [4,38,39] but not others [35-37,34]. In the current study, embryonic pericytes stimulated by the Notch ligands Dll4 and Jag1 did not up-regulate *Pdgfrβ* expression, suggesting that the reduced expression of *Pdgfrβ* in pericytes was not directly downstream of the decreased endothelial expression of *Jag1* in the *Flt1*$^{-/-}$ ESC-derived vessels. In addition, pericyte coverage of ESC-derived vessels was not

influenced by the addition of the Notch inhibitor DAPT. These observations are consistent with other embryonic vascular development studies in which loss of Notch signaling did not compromise pericyte PDGFRβ synthesis or pericyte coverage within the microcirculation [35,37]. Collectively our data, along with others, suggest that pericyte *Pdgfrβ* expression is Notch-independent in certain contexts. PDGFRβ activity may depend on alternate modes of regulation such as via other pathways e.g. Wnt or Transforming Growth Factor-β (TGFβ) signaling [97,98] or through a ligand-dependent feedback loop.

Pericyte coverage and stabilization of the developing vasculature requires competent PDGF-B signaling via full-length PDGFRβ on pericytes [99,16,43,100]. Interestingly, recent studies have suggested that perivascular cells may produce truncated PDGFRβ isoforms in certain scenarios like hypoxia, nutrient starvation, or rapid cellular proliferation [44-47,55]. Although less abundant in the *Flt1*$^{-/-}$ background, a PDGFRβ isoform shorter than full-length PDGFRβ (~60 kDa) was detected in pericytes from WT and *Flt1*$^{-/-}$ ESC-derived vessels. Sequence analysis suggested that this PDGFRβ isoform is presumably not the product of alternative splicing on the mRNA level, but rather from post-translational modification such as proteolytic cleavage, consistent with previous studies [45]. Receptor isoforms, particularly soluble ones, are a conserved element of numerous signaling pathways, including the VEGF-A axis [50,11,61], often functioning to regulate ligand abundance and spatial distribution. It is therefore intriguing to speculate that this PDGFRβ isoform might also act in this way to modulate pericyte signaling, thereby “fine-tuning” vessel growth and maturation in certain contexts, such as in the germinal matrix regions of the developing brain [5]. If this or any other

PDGFRβ isoforms are indeed functionally relevant, additional studies will be needed to establish the exact nature of their contribution to PDGF signaling and pericyte biology.

Given the importance of pericytes in promoting vascular stability and maturation throughout the human body [101-104,70], it is critical to expand our understanding of their basic behaviors during vessel development and specifically how different signaling pathways intersect to coordinate pericyte coverage of vascular networks. Here, we provided evidence for how mis-regulated VEGF-A activity impairs pericyte coverage and distribution by disrupting pericyte migration. The onset and progression of several pathological conditions such as cerebrovascular malformations (i.e. AVMs, CCMs, etc.), and neonatal germinal matrix hemorrhage involve a component of VEGF-A signaling occurring beyond a physiological range. The vascular abnormalities associated with these conditions result, in part, from downstream defects in pericyte behaviors and their underlying signaling mechanisms. Our data, along with others, suggest that therapeutic strategies designed to target Notch or PDGF-B signaling in pericytes will need to consider how a given disease context may alter or limit therapeutic efficacy via the effects of abnormal VEGF-A activity on pericyte responsiveness.

REFERENCES

1. Benjamin EJ, Blaha MJ, Chiuve SE, Cushman M, Das SR, Deo R, de Ferranti SD, Floyd J, Fornage M, Gillespie C, Isasi CR, Jimenez MC, Jordan LC, Judd SE, Lackland D, Lichtman JH, Lisabeth L, Liu S, Longenecker CT, Mackey RH, Matsushita K, Mozaffarian D, Mussolino ME, Nasir K, Neumar RW, Palaniappan L, Pandey DK, Thiagarajan RR, Reeves MJ, Ritchey M, Rodriguez CJ, Roth GA, Rosamond WD, Sasson C, Towfighi A, Tsao CW, Turner MB, Virani SS, Voeks JH, Willey JZ, Wilkins JT, Wu JH, Alger HM, Wong SS, Muntner P, American Heart Association Statistics C, Stroke Statistics S (2017) Heart Disease and Stroke Statistics-2017 Update: A Report From the American Heart Association. Circulation 135 (10):e146-e603. doi:10.1161/CIR.0000000000000485

2. Whitehead KJ, Smith MC, Li DY (2013) Arteriovenous malformations and other vascular malformation syndromes. Cold Spring Harb Perspect Med 3 (2):a006635. doi:10.1101/cshperspect.a006635

3. Leblanc GG, Golanov E, Awad IA, Young WL, Biology of Vascular Malformations of the Brain NWC (2009) Biology of vascular malformations of the brain. Stroke 40 (12):e694-702. doi:10.1161/STROKEAHA.109.563692

4. Kofler NM, Cuervo H, Uh MK, Murtomaki A, Kitajewski J (2015) Combined deficiency of Notch1 and Notch3 causes pericyte dysfunction, models CADASIL, and results in arteriovenous malformations. Sci Rep 5:16449. doi:10.1038/srep16449

5. Dave JM, Mirabella T, Weatherbee SD, Greif DM (2018) Pericyte ALK5/TIMP3 Axis Contributes to Endothelial Morphogenesis in the Developing Brain. Dev Cell. doi:10.1016/j.devcel.2018.01.018

6. Chappell JC, Bautch VL (2010) Vascular development: genetic mechanisms and links to vascular disease. Curr Top Dev Biol 90:43-72. doi:S0070-2153(10)90002-1 [pii]

10.1016/S0070-2153(10)90002-1

7. Vieira JM, Ruhrberg C, Schwarz Q (2010) VEGF receptor signaling in vertebrate development. Organogenesis 6 (2):97-106

8. Gerhardt H, Golding M, Fruttiger M, Ruhrberg C, Lundkvist A, Abramsson A, Jeltsch M, Mitchell C, Alitalo K, Shima D, Betsholtz C (2003) VEGF guides angiogenic sprouting utilizing endothelial tip cell filopodia. J Cell Biol 161 (6):1163-1177

9. Kappas NC, Zeng G, Chappell JC, Kearney JB, Hazarika S, Kallianos KG, Patterson C, Annex BH, Bautch VL (2008) The VEGF receptor Flt-1 spatially modulates Flk-1 signaling and blood vessel branching. J Cell Biol 181 (5):847-858. doi:jcb.200709114 [pii]

10.1083/jcb.200709114

10. Strilic B, Kucera T, Eglinger J, Hughes MR, McNagny KM, Tsukita S, Dejana E, Ferrara N, Lammert E (2009) The molecular basis of vascular lumen formation in the developing mouse aorta. Dev Cell 17 (4):505-515. doi:S1534-5807(09)00349-9 [pii]

10.1016/j.devcel.2009.08.011

11. Chappell JC, Mouillesseaux KP, Bautch VL (2013) Flt-1 (Vascular Endothelial Growth Factor Receptor-1) Is Essential for the Vascular Endothelial Growth Factor-Notch Feedback Loop During Angiogenesis. Arterioscler Thromb Vasc Biol 33 (8):1952-1959. doi:ATVBAHA.113.301805 [pii]

10.1161/ATVBAHA.113.301805

12. Jakobsson L, Bentley K, Gerhardt H (2009) VEGFRs and Notch: a dynamic collaboration in vascular patterning. Biochem Soc Trans 37 (Pt 6):1233-1236. doi:BST0371233 [pii]

10.1042/BST0371233

13. Siekmann AF, Covassin L, Lawson ND (2008) Modulation of VEGF signalling output by the Notch pathway. Bioessays 30 (4):303-313. doi:10.1002/bies.20736

14. Hellstrom M, Phng LK, Hofmann JJ, Wallgard E, Coultas L, Lindblom P, Alva J, Nilsson AK, Karlsson L, Gaiano N, Yoon K, Rossant J, Iruela-Arispe ML, Kalen M, Gerhardt H, Betsholtz C (2007) Dll4 signalling through Notch1 regulates formation of tip cells during angiogenesis. Nature 445 (7129):776-780. doi:nature05571 [pii]

10.1038/nature05571

15. Gerhardt H, Betsholtz C (2003) Endothelial-pericyte interactions in angiogenesis. Cell Tissue Res 314 (1):15-23. doi:10.1007/s00441-003-0745-x

16. Lindblom P, Gerhardt H, Liebner S, Abramsson A, Enge M, Hellstrom M, Backstrom G, Fredriksson S, Landegren U, Nystrom HC, Bergstrom G, Dejana E, Ostman A, Lindahl P, Betsholtz C (2003) Endothelial PDGF-B retention is required for proper investment of pericytes in the microvessel wall. Genes Dev 17 (15):1835-1840. doi:10.1101/gad.266803

17/15/1835 [pii]

17. Armulik A, Genove G, Mae M, Nisancioglu MH, Wallgard E, Niaudet C, He L, Norlin J, Lindblom P, Strittmatter K, Johansson BR, Betsholtz C (2010) Pericytes regulate the blood-brain barrier. Nature 468 (7323):557-561. doi:nature09522 [pii]

10.1038/nature09522

18. Daneman R, Zhou L, Kebede AA, Barres BA (2010) Pericytes are required for blood-brain barrier integrity during embryogenesis. Nature 468 (7323):562-566. doi:nature09513 [pii]

10.1038/nature09513

19. Stratman AN, Pezoa SA, Farrelly OM, Castranova D, Dye LE, 3rd, Butler MG, Sidik H, Talbot WS, Weinstein BM (2017) Interactions between mural cells and endothelial cells stabilize the developing zebrafish dorsal aorta. Development 144 (1):115-127. doi:10.1242/dev.143131

20. Hill RA, Tong L, Yuan P, Murikinati S, Gupta S, Grutzendler J (2015) Regional Blood Flow in the Normal and Ischemic Brain Is Controlled by Arteriolar Smooth Muscle Cell Contractility and Not by Capillary Pericytes. Neuron 87 (1):95-110. doi:10.1016/j.neuron.2015.06.001

21. Hall CN, Reynell C, Gesslein B, Hamilton NB, Mishra A, Sutherland BA, O'Farrell FM, Buchan AM, Lauritzen M, Attwell D (2014) Capillary pericytes regulate cerebral blood flow in health and disease. Nature 508 (7494):55-60. doi:10.1038/nature13165

22. Fernandez-Klett F, Potas JR, Hilpert D, Blazej K, Radke J, Huck J, Engel O, Stenzel W, Genove G, Priller J (2013) Early loss of pericytes and perivascular stromal cell-induced scar formation after stroke. J Cereb Blood Flow Metab 33 (3):428-439. doi:10.1038/jcbfm.2012.187

23. Hamilton NB, Attwell D, Hall CN (2010) Pericyte-mediated regulation of capillary diameter: a component of neurovascular coupling in health and disease. Front Neuroenergetics 2. doi:10.3389/fnene.2010.00005

24. Bergers G, Song S (2005) The role of pericytes in blood-vessel formation and maintenance. Neuro-oncology 7 (4):452-464. doi:10.1215/S1152851705000232

25. Kofler NM, Shawber CJ, Kangsamaksin T, Reed HO, Galatioto J, Kitajewski J (2011) Notch signaling in developmental and tumor angiogenesis. Genes Cancer 2 (12):1106-1116. doi:10.1177/1947601911423030

26. Schrimpf C, Teebken OE, Wilhelmi M, Duffield JS (2014) The role of pericyte detachment in vascular rarefaction. J Vasc Res 51 (4):247-258. doi:10.1159/000365149

27. Eilken HM, Dieguez-Hurtado R, Schmidt I, Nakayama M, Jeong HW, Arf H, Adams S, Ferrara N, Adams RH (2017) Pericytes regulate VEGF-induced endothelial sprouting through VEGFR1. Nature communications 8 (1):1574. doi:10.1038/s41467-017-01738-3

28. Cao R, Xue Y, Hedlund EM, Zhong Z, Tritsaris K, Tondelli B, Lucchini F, Zhu Z, Dissing S, Cao Y (2010) VEGFR1-mediated pericyte ablation links VEGF and PlGF to

cancer-associated retinopathy. Proc Natl Acad Sci U S A 107 (2):856-861. doi:0911661107 [pii]

10.1073/pnas.0911661107

29. He L, Vanlandewijck M, Raschperger E, Andaloussi Mae M, Jung B, Lebouvier T, Ando K, Hofmann J, Keller A, Betsholtz C (2016) Analysis of the brain mural cell transcriptome. Sci Rep 6:35108. doi:10.1038/srep35108

30. Fruttiger M (2002) Development of the mouse retinal vasculature: angiogenesis versus vasculogenesis. Invest Ophthalmol Vis Sci 43 (2):522-527

31. Shih SC, Ju M, Liu N, Smith LE (2003) Selective stimulation of VEGFR-1 prevents oxygen-induced retinal vascular degeneration in retinopathy of prematurity. J Clin Invest 112 (1):50-57

32. Matsumoto K, Azami T, Otsu A, Takase H, Ishitobi H, Tanaka J, Miwa Y, Takahashi S, Ema M (2012) Study of normal and pathological blood vessel morphogenesis in Flt1-tdsRed BAC Tg mice. Genesis 50 (7):561-571. doi:10.1002/dvg.22031

33. Luo L, Uehara H, Zhang X, Das SK, Olsen T, Holt D, Simonis JM, Jackman K, Singh N, Miya TR, Huang W, Ahmed F, Bastos-Carvalho A, Le YZ, Mamalis C, Chiodo VA, Hauswirth WW, Baffi J, Lacal PM, Orecchia A, Ferrara N, Gao G, Young-Hee K, Fu Y, Owen L, Albuquerque R, Baehr W, Thomas K, Li DY, Chalam KV, Shibuya M, Grisanti S, Wilson DJ, Ambati J, Ambati BK (2013) Photoreceptor avascular privilege is shielded by soluble VEGF receptor-1. Elife 2:e00324. doi:10.7554/eLife.00324

34. Liu H, Kennard S, Lilly B (2009) NOTCH3 expression is induced in mural cells through an autoregulatory loop that requires endothelial-expressed JAGGED1. Circ Res 104 (4):466-475. doi:CIRCRESAHA.108.184846 [pii]

10.1161/CIRCRESAHA.108.184846

35. Henshall TL, Keller A, He L, Johansson BR, Wallgard E, Raschperger E, Mae MA, Jin S, Betsholtz C, Lendahl U (2015) Notch3 is necessary for blood vessel integrity in the central nervous system. Arterioscler Thromb Vasc Biol 35 (2):409-420. doi:10.1161/ATVBAHA.114.304849

36. Pedrosa AR, Trindade A, Carvalho C, Graca J, Carvalho S, Peleteiro MC, Adams RH, Duarte A (2015) Endothelial Jagged1 promotes solid tumor growth through both pro-angiogenic and angiocrine functions. Oncotarget 6 (27):24404-24423. doi:10.18632/oncotarget.4380

37. Volz KS, Jacobs AH, Chen HI, Poduri A, McKay AS, Riordan DP, Kofler N, Kitajewski J, Weissman I, Red-Horse K (2015) Pericytes are progenitors for coronary artery smooth muscle. Elife 4. doi:10.7554/eLife.10036

38. Jin S, Hansson EM, Tikka S, Lanner F, Sahlgren C, Farnebo F, Baumann M, Kalimo H, Lendahl U (2008) Notch signaling regulates platelet-derived growth factor receptor-beta expression in vascular smooth muscle cells. Circ Res 102 (12):1483-1491. doi:10.1161/CIRCRESAHA.107.167965

39. Wang Y, Pan L, Moens CB, Appel B (2014) Notch3 establishes brain vascular integrity by regulating pericyte number. Development 141 (2):307-317. doi:10.1242/dev.096107

40. Geraldes P, Hiraoka-Yamamoto J, Matsumoto M, Clermont A, Leitges M, Marette A, Aiello LP, Kern TS, King GL (2009) Activation of PKC-delta and SHP-1 by hyperglycemia causes vascular cell apoptosis and diabetic retinopathy. Nat Med 15 (11):1298-1306. doi:10.1038/nm.2052

41. Abramsson A, Kurup S, Busse M, Yamada S, Lindblom P, Schallmeiner E, Stenzel D, Sauvaget D, Ledin J, Ringvall M, Landegren U, Kjellen L, Bondjers G, Li JP, Lindahl U, Spillmann D, Betsholtz C, Gerhardt H (2007) Defective N-sulfation of heparan sulfate proteoglycans limits PDGF-BB binding and pericyte recruitment in vascular development. Genes Dev 21 (3):316-331. doi:21/3/316 [pii]

10.1101/gad.398207

42. Hellstrom M, Gerhardt H, Kalen M, Li X, Eriksson U, Wolburg H, Betsholtz C (2001) Lack of pericytes leads to endothelial hyperplasia and abnormal vascular morphogenesis. J Cell Biol 153 (3):543-553

43. Hellstrom M, Kalen M, Lindahl P, Abramsson A, Betsholtz C (1999) Role of PDGF-B and PDGFR-beta in recruitment of vascular smooth muscle cells and pericytes during embryonic blood vessel formation in the mouse. Development 126 (14):3047-3055

44. Sagare AP, Sweeney MD, Makshanoff J, Zlokovic BV (2015) Shedding of soluble platelet-derived growth factor receptor-beta from human brain pericytes. Neurosci Lett 607:97-101. doi:10.1016/j.neulet.2015.09.025

45. Hutter-Schmid B, Humpel C (2016) Platelet-derived Growth Factor Receptor-beta is Differentially Regulated in Primary Mouse Pericytes and Brain Slices. Curr Neurovasc Res 13 (2):127-134

46. Mendelson K, Swendeman S, Saftig P, Blobel CP (2010) Stimulation of platelet-derived growth factor receptor beta (PDGFRbeta) activates ADAM17 and promotes metalloproteinase-dependent cross-talk between the PDGFRbeta and epidermal growth

factor receptor (EGFR) signaling pathways. J Biol Chem 285 (32):25024-25032. doi:10.1074/jbc.M110.102566

47. Duan DS, Pazin MJ, Fretto LJ, Williams LT (1991) A functional soluble extracellular region of the platelet-derived growth factor (PDGF) beta-receptor antagonizes PDGF-stimulated responses. J Biol Chem 266 (1):413-418

48. Hiratsuka S, Minowa O, Kuno J, Noda T, Shibuya M (1998) Flt-1 lacking the tyrosine kinase domain is sufficient for normal development and angiogenesis in mice. Proc Natl Acad Sci U S A 95 (16):9349-9354

49. Sawano A, Takahashi T, Yamaguchi S, Aonuma M, Shibuya M (1996) Flt-1 but not KDR/Flk-1 tyrosine kinase is a receptor for placenta growth factor, which is related to vascular endothelial growth factor. Cell Growth Differ 7 (2):213-221

50. Chappell JC, Cluceru JG, Nesmith JE, Mouillesseaux KP, Bradley V, Hartland C, Hashambhoy-Ramsay YL, Walpole J, Peirce SM, Gabhann FM, Bautch VL (2016) Flt-1 (VEGFR-1) Coordinates Discrete Stages of Blood Vessel Formation. Cardiovasc Res 111 (1):84-93. doi:10.1093/cvr/cvw091

51. Roberts DM, Kearney JB, Johnson JH, Rosenberg MP, Kumar R, Bautch VL (2004) The vascular endothelial growth factor (VEGF) receptor Flt-1 (VEGFR-1) modulates Flk-1 (VEGFR-2) signaling during blood vessel formation. Am J Pathol 164 (5):1531-1535

52. Taylor SM, Nevis KR, Park HL, Rogers GC, Rogers SL, Cook JG, Bautch VL (2010) Angiogenic factor signaling regulates centrosome duplication in endothelial cells of developing blood vessels. Blood 116 (16):3108-3117. doi:10.1182/blood-2010-01-266197

53. Zeng G, Taylor SM, McColm JR, Kappas NC, Kearney JB, Williams LH, Hartnett ME, Bautch VL (2007) Orientation of endothelial cell division is regulated by VEGF signaling during blood vessel formation. Blood 109 (4):1345-1352

54. Ho VC, Duan LJ, Cronin C, Liang BT, Fong GH (2012) Elevated vascular endothelial growth factor receptor-2 abundance contributes to increased angiogenesis in vascular endothelial growth factor receptor-1-deficient mice. Circulation 126 (6):741-752. doi:CIRCULATIONAHA.112.091603 [pii]

10.1161/CIRCULATIONAHA.112.091603

55. Hosaka K, Yang Y, Seki T, Nakamura M, Andersson P, Rouhi P, Yang X, Jensen L, Lim S, Feng N, Xue Y, Li X, Larsson O, Ohhashi T, Cao Y (2013) Tumour PDGF-BB expression levels determine dual effects of anti-PDGF drugs on vascular remodelling and metastasis. Nature communications 4:2129. doi:10.1038/ncomms3129

56. Kearney JB, Bautch VL (2003) In vitro differentiation of mouse ES cells: hematopoietic and vascular development. Methods Enzymol 365:83-98

57. Schindelin J, Arganda-Carreras I, Frise E, Kaynig V, Longair M, Pietzsch T, Preibisch S, Rueden C, Saalfeld S, Schmid B, Tinevez JY, White DJ, Hartenstein V, Eliceiri K, Tomancak P, Cardona A (2012) Fiji: an open-source platform for biological-image analysis. Nature methods 9 (7):676-682. doi:10.1038/nmeth.2019

58. Stegmuller J, Schneider S, Hellwig A, Garwood J, Trotter J (2002) AN2, the mouse homologue of NG2, is a surface antigen on glial precursor cells implicated in control of cell migration. J Neurocytol 31 (6-7):497-505

59. Zhao H, Darden J, Chappell JC (2018) Establishment and Characterization of an Embryonic Pericyte Cell Line. Microcirculation:e12461. doi:10.1111/micc.12461

60. Nesmith JE, Chappell JC, Cluceru JG, Bautch VL (2017) Blood vessel anastomosis is spatially regulated by Flt1 during angiogenesis. Development 144 (5):889-896. doi:10.1242/dev.145672

61. Chappell JC, Taylor SM, Ferrara N, Bautch VL (2009) Local guidance of emerging vessel sprouts requires soluble Flt-1. Dev Cell 17 (3):377-386. doi:10.1016/j.devcel.2009.07.011

62. Wild R, Klems A, Takamiya M, Hayashi Y, Strahle U, Ando K, Mochizuki N, van Impel A, Schulte-Merker S, Krueger J, Preau L, le Noble F (2017) Neuronal sFlt1 and Vegfaa determine venous sprouting and spinal cord vascularization. Nature communications 8:13991. doi:10.1038/ncomms13991

63. Krueger J, Liu D, Scholz K, Zimmer A, Shi Y, Klein C, Siekmann A, Schulte-Merker S, Cudmore M, Ahmed A, le Noble F (2011) Flt1 acts as a negative regulator of tip cell formation and branching morphogenesis in the zebrafish embryo. Development 138 (10):2111-2120. doi:138/10/2111 [pii]

10.1242/dev.063933

64. Zygmunt T, Gay CM, Blondelle J, Singh MK, Flaherty KM, Means PC, Herwig L, Krudewig A, Belting HG, Affolter M, Epstein JA, Torres-Vazquez J (2011) Semaphorin-PlexinD1 signaling limits angiogenic potential via the VEGF decoy receptor sFlt1. Dev Cell 21 (2):301-314. doi:S1534-5807(11)00267-X [pii]

10.1016/j.devcel.2011.06.033

65. Stefater JA, 3rd, Lewkowich I, Rao S, Mariggi G, Carpenter AC, Burr AR, Fan J, Ajima R, Molkentin JD, Williams BO, Wills-Karp M, Pollard JW, Yamaguchi T, Ferrara N,

Gerhardt H, Lang RA (2011) Regulation of angiogenesis by a non-canonical Wnt-Flt1 pathway in myeloid cells. Nature 474 (7352):511-515. doi:nature10085 [pii]

10.1038/nature10085

66. Greenberg JI, Shields DJ, Barillas SG, Acevedo LM, Murphy E, Huang J, Scheppke L, Stockmann C, Johnson RS, Angle N, Cheresh DA (2008) A role for VEGF as a negative regulator of pericyte function and vessel maturation. Nature 456 (7223):809-813. doi:nature07424 [pii]

10.1038/nature07424

67. Yamagishi S, Yonekura H, Yamamoto Y, Fujimori H, Sakurai S, Tanaka N, Yamamoto H (1999) Vascular endothelial growth factor acts as a pericyte mitogen under hypoxic conditions. Lab Invest 79 (4):501-509

68. Hagedorn M, Balke M, Schmidt A, Bloch W, Kurz H, Javerzat S, Rousseau B, Wilting J, Bikfalvi A (2004) VEGF coordinates interaction of pericytes and endothelial cells during vasculogenesis and experimental angiogenesis. Dev Dyn 230 (1):23-33. doi:10.1002/dvdy.20020

69. Larina IV, Shen W, Kelly OG, Hadjantonakis AK, Baron MH, Dickinson ME (2009) A membrane associated mCherry fluorescent reporter line for studying vascular remodeling and cardiac function during murine embryonic development. Anat Rec (Hoboken) 292 (3):333-341. doi:10.1002/ar.20821

70. Armulik A, Genove G, Betsholtz C (2011) Pericytes: developmental, physiological, and pathological perspectives, problems, and promises. Dev Cell 21 (2):193-215. doi:S1534-5807(11)00269-3 [pii]

10.1016/j.devcel.2011.07.001

71. Trotter J, Karram K, Nishiyama A (2010) NG2 cells: Properties, progeny and origin. Brain Res Rev 63 (1-2):72-82. doi:10.1016/j.brainresrev.2009.12.006

72. Attwell D, Mishra A, Hall CN, O'Farrell FM, Dalkara T (2016) What is a pericyte? J Cereb Blood Flow Metab 36 (2):451-455. doi:10.1177/0271678X15610340

73. Berthiaume AA, Grant RI, McDowell KP, Underly RG, Hartmann DA, Levy M, Bhat NR, Shih AY (2018) Dynamic Remodeling of Pericytes In Vivo Maintains Capillary Coverage in the Adult Mouse Brain. Cell reports 22 (1):8-16. doi:10.1016/j.celrep.2017.12.016

74. Fischer C, Mazzone M, Jonckx B, Carmeliet P (2008) FLT1 and its ligands VEGFB and PlGF: drug targets for anti-angiogenic therapy? Nat Rev Cancer 8 (12):942-956. doi:nrc2524 [pii]

10.1038/nrc2524

75. Arreola A, Payne LB, Julian MH, de Cubas AA, Daniels AB, Taylor S, Zhao H, Darden J, Bautch VL, Rathmell WK, Chappell JC (2018) Von Hippel-Lindau mutations disrupt vascular patterning and maturation via Notch. JCI Insight 3 (4). doi:10.1172/jci.insight.92193

76. Fong GH, Rossant J, Gertsenstein M, Breitman ML (1995) Role of the Flt-1 receptor tyrosine kinase in regulating the assembly of vascular endothelium. Nature 376 (6535):66-70

77. Armulik A, Abramsson A, Betsholtz C (2005) Endothelial/pericyte interactions. Circ Res 97 (6):512-523. doi:97/6/512 [pii]

10.1161/01.RES.0000182903.16652.d7

78. Kurup S, Abramsson A, Li JP, Lindahl U, Kjellen L, Betsholtz C, Gerhardt H, Spillmann D (2006) Heparan sulphate requirement in platelet-derived growth factor B-mediated pericyte recruitment. Biochem Soc Trans 34 (Pt 3):454-455. doi:10.1042/BST0340454

79. Liu ZJ, Shirakawa T, Li Y, Soma A, Oka M, Dotto GP, Fairman RM, Velazquez OC, Herlyn M (2003) Regulation of Notch1 and Dll4 by vascular endothelial growth factor in arterial endothelial cells: implications for modulating arteriogenesis and angiogenesis. Mol Cell Biol 23 (1):14-25

80. Harrington LS, Sainson RC, Williams CK, Taylor JM, Shi W, Li JL, Harris AL (2008) Regulation of multiple angiogenic pathways by Dll4 and Notch in human umbilical vein endothelial cells. Microvasc Res 75 (2):144-154. doi:S0026-2862(07)00080-5 [pii]

10.1016/j.mvr.2007.06.006

81. Beckstead BL, Santosa DM, Giachelli CM (2006) Mimicking cell-cell interactions at the biomaterial-cell interface for control of stem cell differentiation. J Biomed Mater Res A 79 (1):94-103. doi:10.1002/jbm.a.30760

82. Mouillesseaux KP, Wiley DS, Saunders LM, Wylie LA, Kushner EJ, Chong DC, Citrin KM, Barber AT, Park Y, Kim JD, Samsa LA, Kim J, Liu J, Jin SW, Bautch VL (2016) Notch regulates BMP responsiveness and lateral branching in vessel networks via SMAD6. Nature communications 7:13247. doi:10.1038/ncomms13247

83. Simonavicius N, Ashenden M, van Weverwijk A, Lax S, Huso DL, Buckley CD, Huijbers IJ, Yarwood H, Isacke CM (2012) Pericytes promote selective vessel regression to regulate vascular patterning. Blood 120 (7):1516-1527. doi:10.1182/blood-2011-01-332338

84. Kelly-Goss MR, Sweat RS, Stapor PC, Peirce SM, Murfee WL (2014) Targeting pericytes for angiogenic therapies. Microcirculation 21 (4):345-357. doi:10.1111/micc.12107

85. Gaengel K, Genove G, Armulik A, Betsholtz C (2009) Endothelial-mural cell signaling in vascular development and angiogenesis. Arterioscler Thromb Vasc Biol 29 (5):630-638. doi:ATVBAHA.107.161521 [pii]

10.1161/ATVBAHA.107.161521

86. Walpole J, Gabhann FM, Peirce SM, Chappell JC (2017) Agent-based Computational Model of Retinal Angiogenesis Simulates Microvascular Network Morphology as a Function of Pericyte Coverage. Microcirculation. doi:10.1111/micc.12393

87. Birbrair A, Zhang T, Wang ZM, Messi ML, Olson JD, Mintz A, Delbono O (2014) Type-2 pericytes participate in normal and tumoral angiogenesis. Am J Physiol Cell Physiol 307 (1):C25-38. doi:10.1152/ajpcell.00084.2014

88. Ando K, Fukuhara S, Izumi N, Nakajima H, Fukui H, Kelsh RN, Mochizuki N (2016) Clarification of mural cell coverage of vascular endothelial cells by live imaging of zebrafish. Development 143 (8):1328-1339. doi:10.1242/dev.132654

89. Hammes HP, Lin J, Wagner P, Feng Y, Vom Hagen F, Krzizok T, Renner O, Breier G, Brownlee M, Deutsch U (2004) Angiopoietin-2 causes pericyte dropout in the normal retina: evidence for involvement in diabetic retinopathy. Diabetes 53 (4):1104-1110

90. Patan S (1998) TIE1 and TIE2 receptor tyrosine kinases inversely regulate embryonic angiogenesis by the mechanism of intussusceptive microvascular growth. Microvasc Res 56 (1):1-21. doi:10.1006/mvre.1998.2081

91. Suri C, Jones PF, Patan S, Bartunkova S, Maisonpierre PC, Davis S, Sato TN, Yancopoulos GD (1996) Requisite role of angiopoietin-1, a ligand for the TIE2 receptor, during embryonic angiogenesis. Cell 87 (7):1171-1180

92. Jeansson M, Gawlik A, Anderson G, Li C, Kerjaschki D, Henkelman M, Quaggin SE (2011) Angiopoietin-1 is essential in mouse vasculature during development and in response to injury. J Clin Invest 121 (6):2278-2289. doi:10.1172/JCI46322

93. Iivanainen E, Nelimarkka L, Elenius V, Heikkinen SM, Junttila TT, Sihombing L, Sundvall M, Maatta JA, Laine VJ, Yla-Herttuala S, Higashiyama S, Alitalo K, Elenius K (2003) Angiopoietin-regulated recruitment of vascular smooth muscle cells by endothelial-derived heparin binding EGF-like growth factor. FASEB J 17 (12):1609-1621. doi:10.1096/fj.02-0939com

94. Stratman AN, Schwindt AE, Malotte KM, Davis GE (2010) Endothelial-derived PDGF-BB and HB-EGF coordinately regulate pericyte recruitment during vasculogenic tube assembly and stabilization. Blood 116 (22):4720-4730. doi:blood-2010-05-286872 [pii]

10.1182/blood-2010-05-286872

95. Uebelhoer M, Natynki M, Kangas J, Mendola A, Nguyen HL, Soblet J, Godfraind C, Boon LM, Eklund L, Limaye N, Vikkula M (2013) Venous malformation-causative TIE2 mutations mediate an AKT-dependent decrease in PDGFB. Hum Mol Genet 22 (17):3438-3448. doi:10.1093/hmg/ddt198

96. High FA, Lu MM, Pear WS, Loomes KM, Kaestner KH, Epstein JA (2008) Endothelial expression of the Notch ligand Jagged1 is required for vascular smooth muscle development. Proc Natl Acad Sci U S A 105 (6):1955-1959. doi:0709663105 [pii]

10.1073/pnas.0709663105

97. Cohen ED, Ihida-Stansbury K, Lu MM, Panettieri RA, Jones PL, Morrisey EE (2009) Wnt signaling regulates smooth muscle precursor development in the mouse lung via a tenascin C/PDGFR pathway. J Clin Invest 119 (9):2538-2549. doi:10.1172/JCI38079

98. Peng Y, Yan S, Chen D, Cui X, Jiao K (2017) Pdgfrb is a direct regulatory target of TGFbeta signaling in atrioventricular cushion mesenchymal cells. PLoS One 12 (4):e0175791. doi:10.1371/journal.pone.0175791

99. Bjarnegard M, Enge M, Norlin J, Gustafsdottir S, Fredriksson S, Abramsson A, Takemoto M, Gustafsson E, Fassler R, Betsholtz C (2004) Endothelium-specific ablation of PDGFB leads to pericyte loss and glomerular, cardiac and placental abnormalities. Development 131 (8):1847-1857. doi:10.1242/dev.01080

131/8/1847 [pii]

100. Lindahl P, Johansson BR, Leveen P, Betsholtz C (1997) Pericyte loss and microaneurysm formation in PDGF-B-deficient mice. Science 277 (5323):242-245

101. Kisler K, Nelson AR, Rege SV, Ramanathan A, Wang Y, Ahuja A, Lazic D, Tsai PS, Zhao Z, Zhou Y, Boas DA, Sakadzic S, Zlokovic BV (2017) Pericyte degeneration leads to neurovascular uncoupling and limits oxygen supply to brain. Nature neuroscience. doi:10.1038/nn.4489

102. Trost A, Lange S, Schroedl F, Bruckner D, Motloch KA, Bogner B, Kaser-Eichberger A, Strohmaier C, Runge C, Aigner L, Rivera FJ, Reitsamer HA (2016) Brain and Retinal Pericytes: Origin, Function and Role. Front Cell Neurosci 10:20. doi:10.3389/fncel.2016.00020

103. Sweeney MD, Ayyadurai S, Zlokovic BV (2016) Pericytes of the neurovascular unit: key functions and signaling pathways. Nature neuroscience 19 (6):771-783. doi:10.1038/nn.4288

104. Zhao Z, Nelson AR, Betsholtz C, Zlokovic BV (2015) Establishment and Dysfunction of the Blood-Brain Barrier. Cell 163 (5):1064-1078. doi:10.1016/j.cell.2015.10.067

Supplemental Materials and Methods

Live Imaging of Ex Vivo Angiogenesis

All animal experiments were conducted with review and approval from the Virginia Tech IACUC. All protocols were reviewed and approved by IACUC boards. The Virginia Tech NIH/PHS Animal Welfare Assurance Number is A-32081-01 (expires 7/31/2021). Embryonic tissue culture assay (ETCA) experiments were conducted as previously described [1]. Briefly, following mating with *Flk1-eGFP; Ng2-DsRed* males, pregnant C57BL/6 female mice were sacrificed at embryonic day 14.5 (E14.5) by CO_2 inhalation and cervical dislocation. Embryos were retrieved from the uterus in 4ºC dissection media, and genotype was evaluated by fluorescence microscopy. Embryos positive for both *Ng2-DsRed* (i.e. pericyte signal) and *Flk1-eGFP* (i.e. endothelial cell signal) were selected for micro-dissection to isolate dorsal skin (i.e. tissue absent of Ng2+ glia). Dermal tissues were placed in single wells of a glass-bottom 6-well plate and embedded in a fibrin matrix with the hypodermis (subcutaneous layer) facing the glass. Basic culture media was added at 3 mL per well. The following day, spent media was replaced with culture media containing PBS (vehicle control) or VEGF-A (50 ng/ml, Peprotech, Cat #450-32). Plates were then transferred to an incubation chamber (37ºC, 5% CO_2, humidity controlled) mounted on a Zeiss LSM880 confocal microscope for live imaging. Multi-position, time-lapse confocal scans were acquired through each sample thickness (z-stacks: 6-8 images with 4-6 microns between planes) at 10-25 minute intervals for a minimum of 12 hours using a 20x objective. Each time point was compressed from the raw z-stack and exported as a video file in RGB channel format.

Embryonic Stem Cell (ESC) Maintenance Media Components:

- Dulbeccos's Modified Eagle's Medium- High glucose (DMEM-H) with added 0.1% Gentamicin (Thermo Fisher Scientific, Cat. No. 1575-060)
- 100x MTG is made from 11.5 M Sigma bottle (1-Thioglycerol, Cat. No. M6145-25ML) diluted in sterile PBS
- Leukemia Inhibiting Factor (LIF) contained in media collected from cultured 5637 tumor cell line (ATCC)
- Fetal Bovine Serum (FBS) from Thermo Fisher Scientific, Cat. No. 26140079
- Antibiotic-Antimycotic from Thermo Fisher Scientific, Cat. No. 15240112

Culture Media Composition

Maintenance Media for ESCs: Our ESC maintenance media is used for passaging of ES cells and maintenance of cell cultures that are not to be used in experiments. The media contains the following; 88mls of 5637 tumor media (65%), 22.9mls of FBS (17%) 1.6 mls each of 100x MTG and Antibiotic-Antimycotic (1.2% each) and 21.1 mls DMEM-H (16%) to make 135.6mls media

Differentiation Media for ESCs: Our differentiation media contains the same components as our maintenance media except LIF (5637 tumor media). To make 250 mls of differentiation media, add the following: 50mls FBS (20%), 5mls each of 100x MTG and Antibiotic-Antimycotic (2% each) and 194.75 mls DMEM-H (78%).

Dissection Media for ETCA: Our dissection media used in embryonic tissue culture live imaging experiments uses cold media containing the following; DMEM-H and 5% Antibiotic-Antimycotic.

Culture Media for ETCA: Our culture media used in embryonic tissue culture live imaging experiments uses media containing the following; DMEM-H, 10% FBS and 5% Antibiotic-Antimycotic.

Pericyte Cell Line Isolation and Characterization

Previously, our lab isolated an enriched population of Neural Glial Antigen-2 (NG2):DsRed+ pericytes from embryonic day 12.5 (E12.5) mice. Briefly, male mice expressing the DsRed fluorescent protein under control of the NG2 promoter (i.e. NG2-DsRed mice) [Tg(Cspg4-DsRed.T1)1Akik/J, JAX # 008241, The Jackson Laboratory, Bar Harbor, ME] were set up in timed matings with C57BL/6 females. On embryonic day 12.5 (E12.5) embryos were collected and verified as NG2-DsRed+ under fluorescent dissection scope. Embryos were then digested in Type 1 collagenase in PBS for 1 hour. Dissociated cells were then sorted using flow cytometry to isolate NG2-DsRed+ cells, cultured these cells and froze them for future use.

This pericyte cell line was compared to mouse embryonic fibroblasts (MEFs) with respect to gene expression, cell morphology, migrational patterns, and engagement with endothelial cells in single and co-culture conditions. Findings showed distinct characteristics from MEFs in regard to gene expression patterns, cell morphology, and 2D migration patterns that were phenotypically different than MEF cells. When co-cultured with human umbilical vein endothelial cells, these pericytes stimulated increased VE-Cadherin junction formation between HUVECs as well as organized them into primitive vasculature structures.

Additionally, blood vessel formation and interaction was assessed in three different models, including cell culture with human umbilical vein endothelial cells (HUVECs) in 2D and 3D collagen matrix cultures, wild-type ESC derived vessels in both 2D and collagen matrix cultures, as well as in embryonic tissue culture assay live imaging. The pericyte cell line was added to these models to study the incorporation and migration of exogenous pericytes to developing vessels.

For more detailed description of results, please see Zhao et al. *Microcirculation* 2018.

Exogenous VEGF-A Treatments to ES Cells

ESCs were treated with 50ng/mL of VEGF-A (PeproTech, Cat. # 450-32-100UG) or PBS vehicle control at days 0, 3, 5, and 7. Briefly, WT ESCs were maintained as described previously [1-3]. After undifferentiated WT ESCs gave rise to spherical embryoid bodies (EBs) (i.e. over 3-4 days in culture), these EBs were released from the culture plate and collected using 1x dispase in PBS (i.e. experimental Day 0). EBs were washed twice with PBS and re-plated in differentiation media treated with 50ng/mL VEGF-A or vehicle control in 10 cm^2 petri dishes. The cell suspension in media was added at 5 mls per plate and cultured at 37^oC and 5% CO_2. On experimental Day 3, EBs were transferred to slide flasks using sterile wide-tip transfer pipets and media treated with 50ng/mL VEGF-A or vehicle control. Differentiating EBs were cultured for a 6 additional days, feeding with VEGF-A treatment or vehicle control at Days 5 and 7, for a total of 9 days. Differentiated cells were washed twice with PBS, fixed, and processed for immunocytochemistry (ICC) and confocal imaging.

Notch Inhibition Treatments on ESC Model

ESCs were treated with 2μM γ-secretase inhibitor (N-[N-(3,5-**D**ifluorophenacetyl)-L-**A**lanyl]-S-**P**henylglycine **T**-butyl ester, DAPT, Santa Cruz, Cat. # 208255-80-5) or vehicle control i.e. equivalent volume of dimethyl sulfide (DMSO, Sigma) on Days 5 and 7. Briefly, WT and *Flt1*$^{-/-}$ ESCs were maintained as described previously [1-3]. After undifferentiated WT ESCs gave rise to spherical embryoid bodies (EBs) (i.e. over 3-4 days in culture), these EBs were released from the culture plate and collected using 1x dispase in PBS (i.e. experimental Day 0). EBs were washed twice with PBS and re-plated in differentiation media in 10 cm^2 petri dishes. The cell suspension in media was added at 5 mls per plate and cultured at 37^{o}C and 5% CO_2. On experimental Day 3, EBs were transferred to slide flasks using sterile wide-tip transfer pipets and normal differentiation media. Differentiating EBs were cultured for a 6 additional days, feeding with treatments (DAPT or vehicle control DMSO) at Days 5 and 7, for a total of 9 days. Differentiated cells were washed twice with PBS, fixed, and processed for immunocytochemistry (ICC) and confocal imaging of Day 9 cultures.

ONLINE RESOURCES – SUPPLEMENTAL MOVIE LEGENDS

Movies available at https://link.springer.com/article/10.1007%2Fs10456-018-9648-z

Supplemental Movie 1. From *Figure 4Ai-iii* of the main paper. Time sequence of pericytes (red, *Ng2-DsRed*+) engaging with *Flk-1-eGFP*+ endothelial sprouts (green) emerging from parent vessels within cultured E13.5 embryonic skin exposed to a vehicle (PBS) control. Time in upper right corner, hh:mm (hours:minutes). Scale bar, 100 μm.

Supplemental Movie 2. From *Figure 4Aiv-vi* of the main paper. Time sequence of pericytes (red, *Ng2-DsRed*+) engaging with *Flk-1-eGFP*+ endothelial sprouts (green) emerging from parent vessels within cultured E13.5 embryonic skin exposed to exogenous VEGF-A. Time in upper right corner, hh:mm (hours:minutes). Scale bar, 100 μm.

REFERENCES

1. Chappell JC, Cluceru JG, Nesmith JE, Mouillesseaux KP, Bradley V, Hartland C, Hashambhoy-Ramsay YL, Walpole J, Peirce SM, Gabhann FM, Bautch VL (2016) Flt-1 (VEGFR-1) Coordinates Discrete Stages of Blood Vessel Formation. Cardiovasc Res 111 (1):84-93. doi:10.1093/cvr/cvw091

2. Chappell JC, Taylor SM, Ferrara N, Bautch VL (2009) Local guidance of emerging vessel sprouts requires soluble Flt-1. Dev Cell 17 (3):377-386. doi:10.1016/j.devcel.2009.07.011

3. Kearney JB, Bautch VL (2003) In vitro differentiation of mouse ES cells: hematopoietic and vascular development. Methods Enzymol 365:83-98

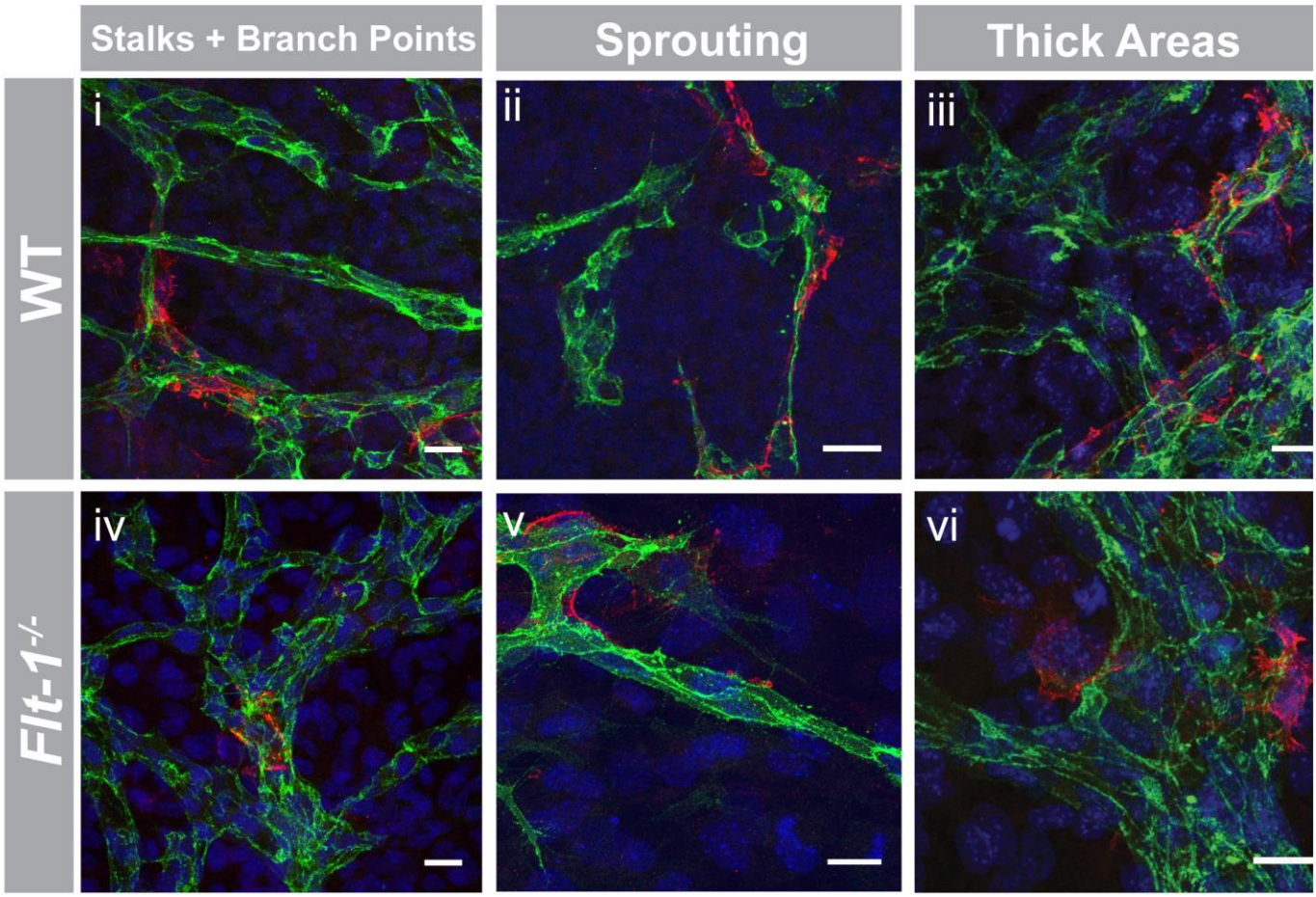

Online Resource 2 -- Supplemental Figure 1. Representative images of WT (i-iii) and *Flt1*$^{-/-}$ (iv-vi) Day 9 ESC-derived blood vessels labeled for endothelial cells (Pecam1: green), pericytes (Ng2, red), and cell nuclei (DAPI, blue). Distinct morphological locations (Stalks +Branch Points, Sprouting, and Thick Areas) were selected to provide a more comprehensive view of pericyte coverage within each region. Scale bars, 25 μm.

Excess Vascular Endothelial Growth Factor-A Disrupts Pericyte Recruitment during Blood Vessel Formation. Angiogenesis. Jordan Darden, Laura Beth Payne, Huaning Zhao, John C. Chappell.

Corresponding Author: John C. Chappell, Center for Heart and Regenerative Medicine, Virginia Tech Carilion Research Institute, Roanoke, VA 24016, USA. E-mail: JChappell@vtc.vt.edu

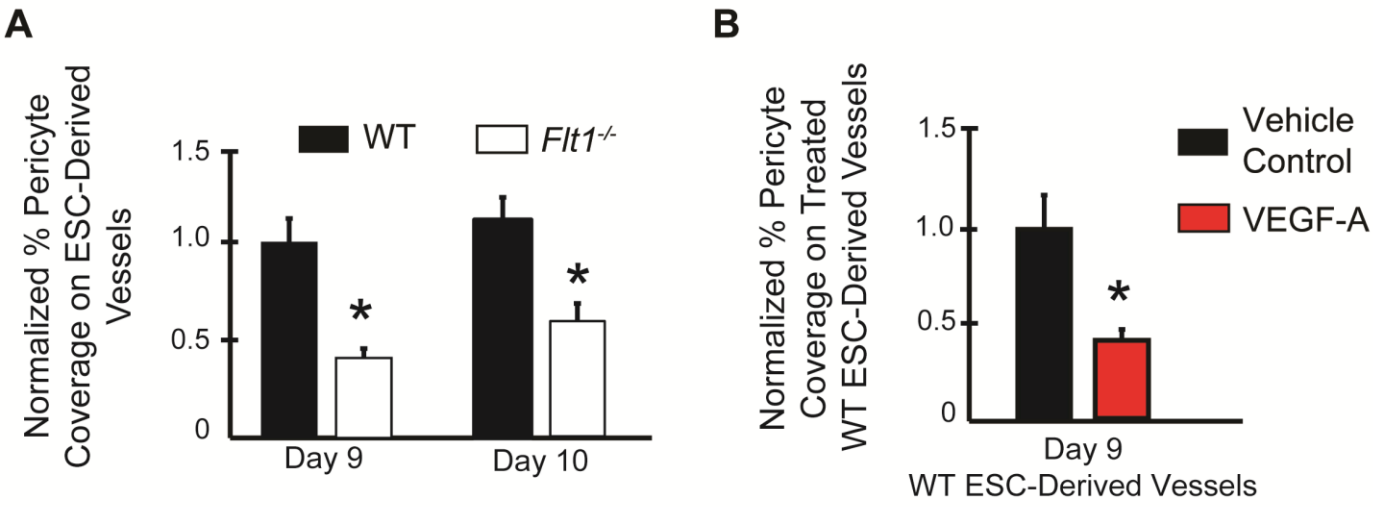

Online Resource 3 -- Supplemental Figure 2. Utilizing raw data presented in Figure 1B, we used the Day 9 WT group to find the normalized average percentages of Ng2+ pericyte coverage on Days 9 (n=6 of biological replicates) and 10 (n=10 of biological replicates) ESC derived vessels for WT (black bars) and *Flt1*$^{-/-}$ (white bars) conditions. Values are averages + Standard Error of the Mean (SEM). *P≤0.05 vs. WT at the same time point. (A) Normalized percentages of Ng2+ pericyte coverage on Day 9 (n=3 biological replicates) WT ESC-derived vessels treated with vehicle control (black bar) and VEGF-A (red bar). Values are averages + Standard Error of the Mean (SEM). *P≤0.05 vs. vehicle control group.

Excess Vascular Endothelial Growth Factor-A Disrupts Pericyte Recruitment during Blood Vessel Formation. Angiogenesis. Jordan Darden, Laura Beth Payne, Huaning Zhao, John C. Chappell.

Corresponding Author: John C. Chappell, Center for Heart and Regenerative Medicine, Virginia Tech Carilion Research Institute, Roanoke, VA 24016, USA. E-mail: JChappell@vtc.vt.edu

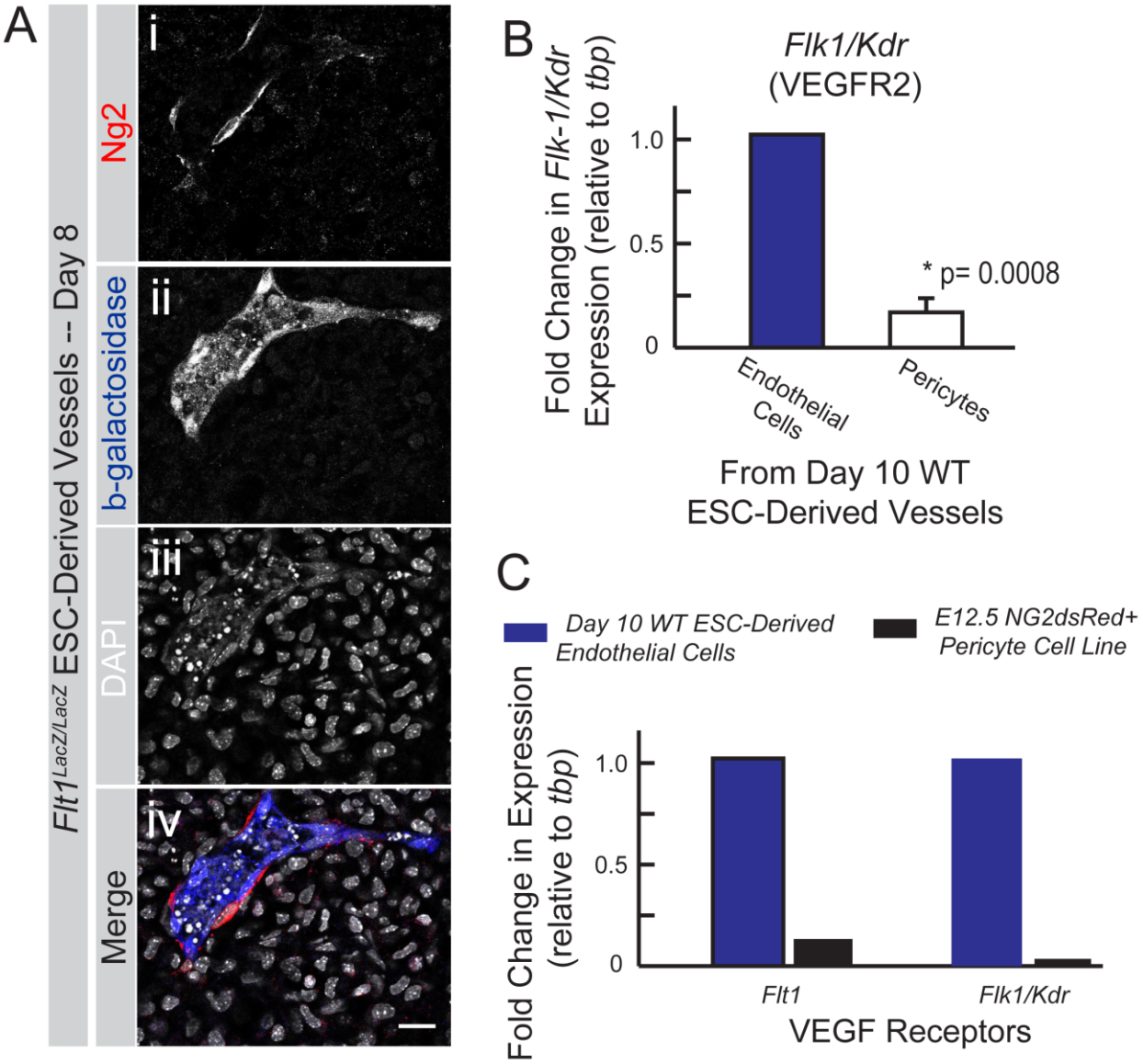

Online Resource 4 -- Supplemental Figure 3. Representative images of Ng2+ pericytes (Ng2: i, red in iv) and Flt1 promoter activity as indicated by β-galactosidase (β-gal: ii, blue in iv) production from the Flt-1:LacZ gene. Cell nuclei are labeled by DAPI (iii, white in iv). Scale bar, 20 μm (A). Fold change in *Flk1/Kdr/VEGFR2* expression between endothelial cells (blue bar) and pericytes (white bar) enriched from Day 10 WT ESC-derived vessels. Values are averages + SEM, n=4 biological replicates. *P≤0.05. (B) Fold change in *Flt1* and *Flk1/Kdr* expression between endothelial cells isolated from Day 10 WT ESC-Derived (blue bars) and our embryonic pericyte cell line (black bars). Values are averages + SEM, n=4 biological replicates. *P≤0.05. (B)

Excess Vascular Endothelial Growth Factor-A Disrupts Pericyte Recruitment during Blood Vessel Formation. Angiogenesis. Jordan Darden, Laura Beth Payne, Huaning Zhao, John C. Chappell.

Corresponding Author: John C. Chappell, Center for Heart and Regenerative Medicine, Virginia Tech Carilion Research Institute, Roanoke, VA 24016, USA. E-mail: JChappell@vtc.vt.edu

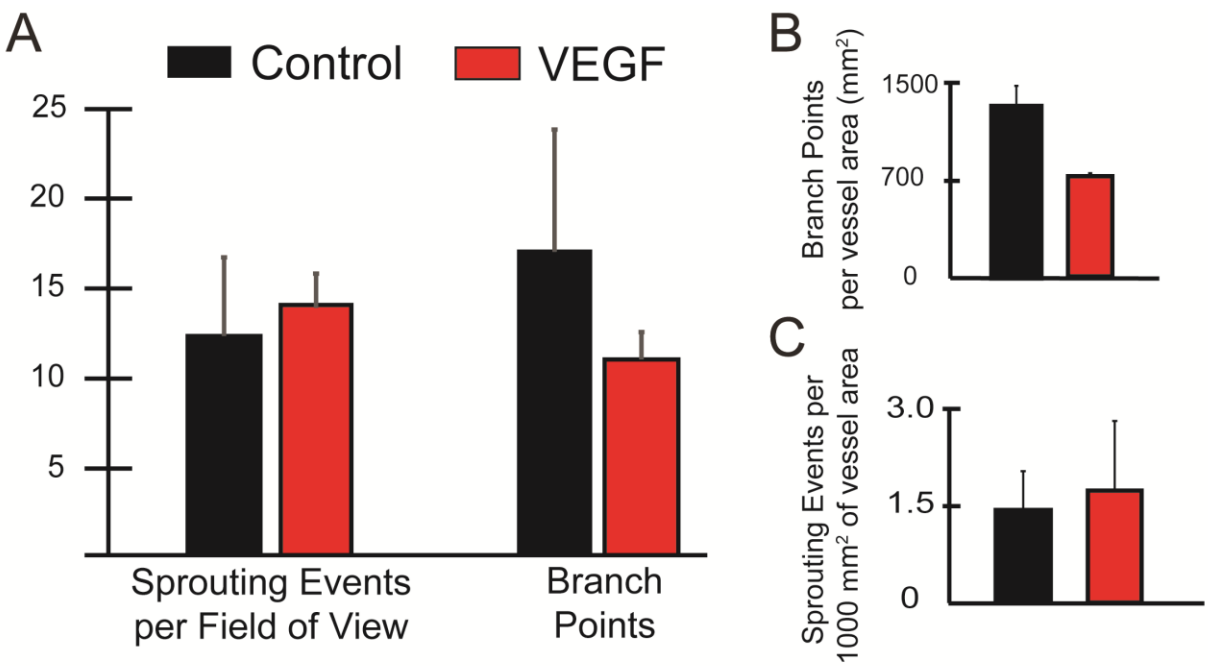

Online Resource 5 -- Supplemental Figure 4. Quantification of endothelial cell sprouting and vessel branching in E14.5 *ex vivo* remodeling embryonic skin vasculature during VEGF-A and control treatment. Values are averages + Standard Error of the Mean (SEM). No statistically significant differences were found (A). Branch point and sprouting event measurements from (A) normalized to vessel area. Values are averages + Standard Error of the Mean (SEM). No statistically significant differences were found (B).

Excess Vascular Endothelial Growth Factor-A Disrupts Pericyte Recruitment during Blood Vessel Formation. Angiogenesis. Jordan Darden, Laura Beth Payne, Huaning Zhao, John C. Chappell.

Corresponding Author: John C. Chappell, Center for Heart and Regenerative Medicine, Virginia Tech Carilion Research Institute, Roanoke, VA 24016, USA. E-mail: JChappell@vtc.vt.edu

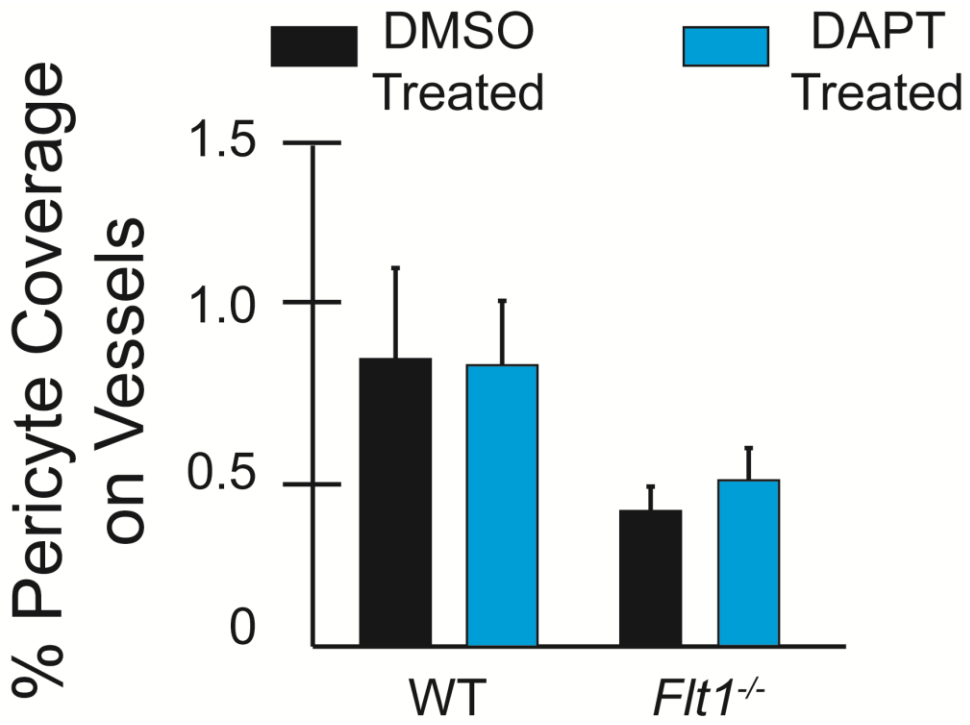

Online Resource 6 -- Supplemental Figure 5. Average percentages of Ng2+ pericyte coverage on Day 10 (n=3 of biological replicates) WT and *Flt1*$^{-/-}$ ESC derived vessels treated with DMSO vehicle control (black bars) or the Notch inhibitor DAPT (blue bars) conditions. Values are averages + Standard Error of the Mean (SEM). No statistically significant differences were found.

Excess Vascular Endothelial Growth Factor-A Disrupts Pericyte Recruitment during Blood Vessel Formation. Angiogenesis. Jordan Darden, Laura Beth Payne, Huaning Zhao, John C. Chappell.

Corresponding Author: John C. Chappell, Center for Heart and Regenerative Medicine, Virginia Tech Carilion Research Institute, Roanoke, VA 24016, USA. E-mail: JChappell@vtc.vt.edu

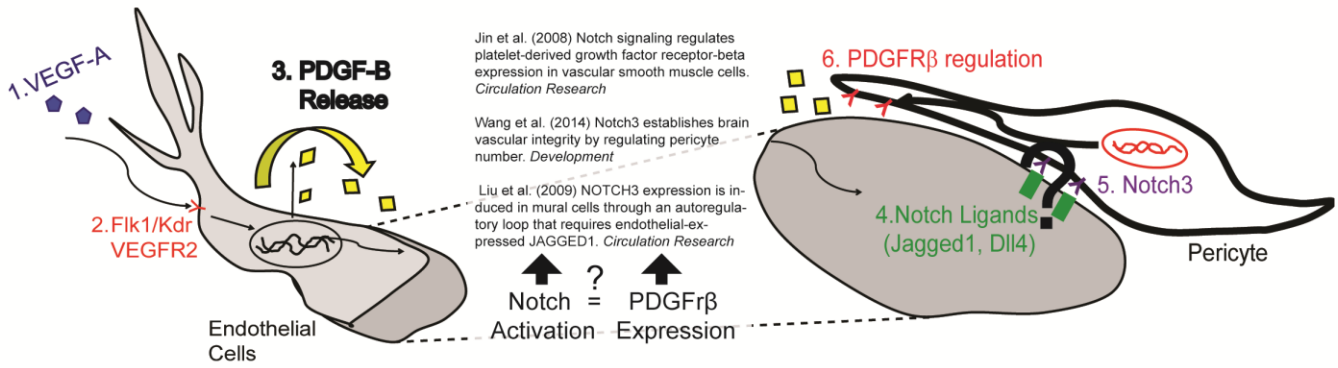

Online Resource 7 -- Supplemental Figure 6. Simplified schematic illustrating the working hypothesis from the current study. Briefly, during developmental blood vessel formation, VEGF-A predominantly signals through endothelial cells (through Flk1/Kdr/ VEGFR2), such that loss of Flt-1 regulation of VEGF-A leads to aberrant endothelial cell signaling and excess PDGF-B release from numerous "tip" cells. Pericyte production of PDGFRβ decreases, which appears to be independent of Notch signaling between pericytes and adjacent endothelial cells. Thus, the observed decrease in pericyte coverage of *Flt1*$^{-/-}$ vessels likely occurs via *direct effects on endothelial cell signaling* and *indirect effects on pericyte signaling and behaviors.*

Excess Vascular Endothelial Growth Factor-A Disrupts Pericyte Recruitment during Blood Vessel Formation. Angiogenesis. Jordan Darden, Laura Beth Payne, Huaning Zhao, John C. Chappell.

Corresponding Author: John C. Chappell, Center for Heart and Regenerative Medicine, Virginia Tech Carilion Research Institute, Roanoke, VA 24016, USA. E-mail: JChappell@vtc.vt.edu

CHAPTER 3

InSite: A High Throughput Image Analysis Platform for Resolving Multi-signal Proximity

Jordan Darden*[,1,2], Harsh Patolia*[,1,3], John C. Chappell[1,4,5]

[1]Center for Heart and Reparative Medicine Research, Fralin Biomedical Research Institute, Roanoke, VA 24016, USA

[2]Graduate Program in Translational Biology, Medicine, and Health, Virginia Polytechnic Institute and State University, Blacksburg, VA 24061, USA

[3]Virginia Tech Carilion School of Medicine, Roanoke VA 24016, USA

[4]Department of Biomedical Engineering and Mechanics, Virginia Polytechnic State Institute and State University, Blacksburg, VA 24061, USA

[5]Department of Basic Science Education, Virginia Tech Carilion School of Medicine, Roanoke, VA 24016, USA

*Both authors contributed equally to this work.

ABSTRACT

Establishing the relative position of two entities in space or time can reveal important information about a particular system during normal and irregular conditions, in biology as well as in a broad range of disciplines. In vascular biology, for example, resolving the relative locations of cellular and molecular components within the blood vessel wall can provide an indication of a healthy vasculature versus one affected by genetic mutation or disease. It is critical therefore to develop high throughput methods for processing large datasets, and specifically those from various imaging modalities, to determine the relative proximity of two or more signals, as this will yield greater insight into key characteristics of the system being studied. Two signals that occupy the same spatial

location for example are often described as “co-localized”, which can be determined via post-acquisition image analysis and yield important quantitative relationships within a system. Signal colocalization metrics can be challenging in the analysis of multi-dimensional image “stacks” however, as flattening these stacks into maximum intensity projections (MIPs) saves time but sacrifices spatial fidelity. MIPs are generated via a compression algorithm that projects voxels with the highest intensity along the depth axis (Z) in the visualization plane (XY). Implementing MIP methods for large, light microscopy datasets can therefore bias subsequent analyses. In contrast, utilizing manual 2D image analysis techniques to quantify large sets of light microscopy data “slice-by-slice”, though potentially more accurate, is often inefficient and time-consuming. Therefore, in creating InSite, we aimed to develop an automated and adaptive image analysis algorithm that addresses the needs of efficiency and reproducibility, as well as for high-throughput and fidelity, for light microscopy datasets as well as for a broad range of applications involving multiple signal localization.

INTRODUCTION

Detailed morphological analysis has been a useful approach across many disciplines within the life sciences, being utilized in comparative observation of plants, animals, cells, and microorganisms. Studies focused on a particular organism’s form have not only aided in the classification of new species [1], but also in identifying structural anomalies that may arise within an organism. Morphological comparisons have been critical for gaining new insight into pathological conditions that afflict humans for example [2]. Nevertheless, assessing morphology can extend beyond comparing

inherent differences, but can also be applied to experimental and functional intervention studies to establish certain relationships, such as between cells within a system or between intercellular components [3-5]. Therefore determining the relative position, or proximity, of two or more elements within a biological system (e.g. cells or proteins) can shed light on key characteristics of developmental organization [6], and therefore offer clues to functional pathways. In this way, proximity metrics can implicate specific functions across a range of scales. On the microscopic and ultrastructure level, proximity can be determined for cells or intercellular proteins, and even within particular organisms on a system-wide level. Examples of these important relationships can be seen in the study of neurotransmitter release and uptake in neurons [7, 8], filament localization within skeletal muscle cells [9, 10], and viral protein structure [11], each with broad implications for our understanding of disease progression and recovery.

Vascular biology is another field of study in which proximity measures are critical for understanding the spatial relationships among the various cellular and molecular compartments within the blood vessel wall [12, 13]. A range of imaging modalities, and most notably confocal microscopy, are used to visualize multiple elements of the vascular system, including endothelial cells and mural cells (i.e. pericytes and vascular smooth muscle cells) [13], along with other key components like the extracellular matrix (ECM) that forms the vascular basement membrane (Figure 1) [14, 15]. Deconstructing the vessel wall into basic constituents facilitates a deeper understanding of (i) established and emerging functions of each element, and (ii) how defects in each component might lead to abnormalities on the tissue or systemic level. These insights are particularly relevant in developmental studies [16] as well as those focused on

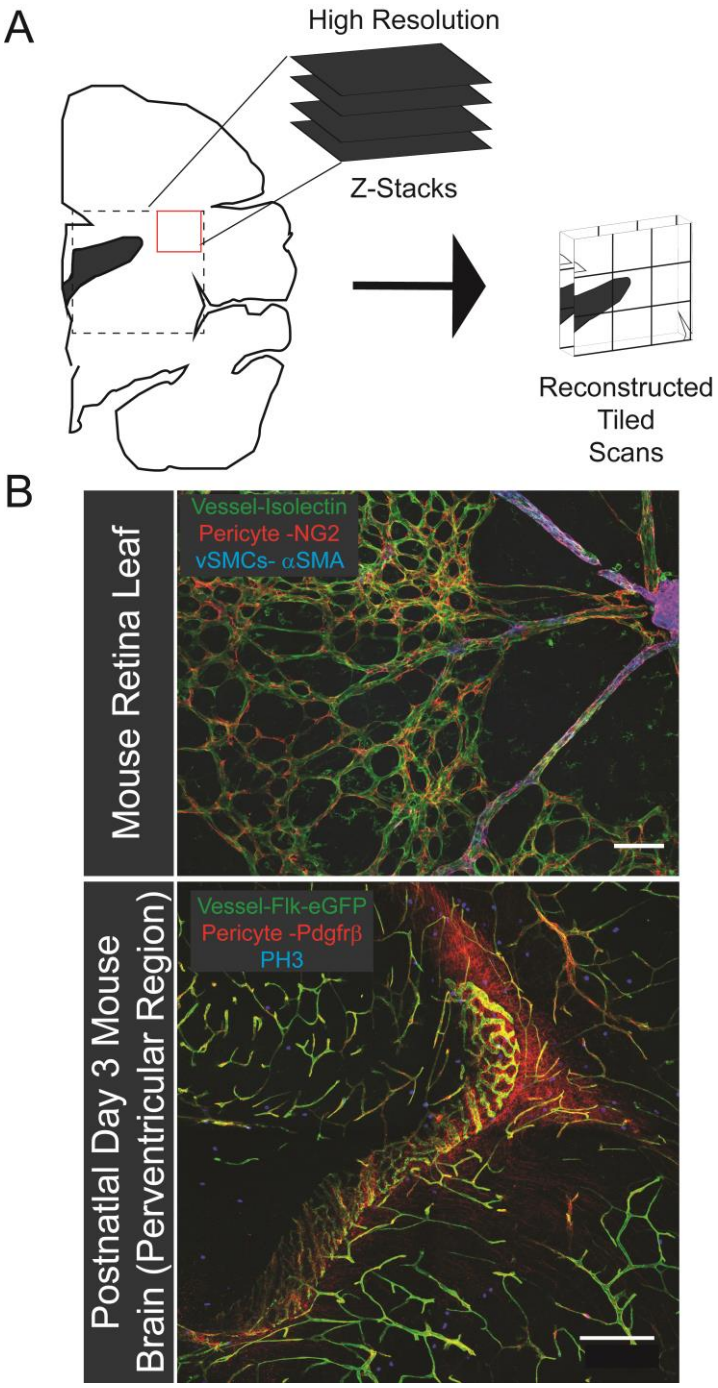

Figure 1. High resolution, high magnification images present a computational challenge for image analysis. **A** Schematic representing how large data files of high-resolution, high-magnification images are acquired and reconstructed for analysis. **B** Example images of complex data sets acquired in retina and brain tissue. Scale bars 100 µm and 250 µm respectively.

pathological conditions such as tumor angiogenesis [17, 18], cardiovascular disease [19], and catastrophic vessel rupture (e.g. hemorrhagic stroke) [20]. As imaging technologies and sample preparation methods [21, 22] continue to develop, vascular structures within larger tissue volumes can be imaged and analyzed at multiple levels of resolution, thus enhancing our interpretations of the integrated relationship among discrete vessel elements.

Since the advent of Minsky's confocal scanning microscope in 1955 [23-25], optical imaging technologies have rapidly expanded, allowing greater resolution in observing biological specimen on the microscopic level while maintaining endogenous geometric relationships between cells and molecules. As imaging modalities continue to advance, so will the need for more rigorous, high-throughput analytical tools [26, 27]. Confocal and multi-photon imaging systems have evolved to capture high resolution, high magnification images in three dimensions along the X, Y, and Z planes. Newer technologies such as light-sheet fluorescence microscopy also allow for visualization of larger, more complete volumes of tissue (such as heart [28], brain, and even whole animal [29]) through digital reconstruction of scanned fields of view. Accumulation of these larger and more complex volumetric renderings generate enormous data files that present several computational challenges in terms of quantitative analysis [24, 25].

A number of previous methods for image quantification included the compression of volumetric data captured in all three dimensions, yielding a 2D image. More specifically, individual "slices" from an image stack are superimposed on each other to yield a maximum intensity projection (MIP). A MIP compression algorithm projects voxels onto the same Z plane in the X-Y visualization field. MIP images are then

analyzed manually or via an automated platform using software packages such as ImageJ [30-33]. While MIP images may be suitable for smaller volumetric images, implementing MIPs for large volumes of light microscopy imaging will likely introduce compression artifacts. In these more comprehensive datasets, signals in discrete and separate Z-planes may appear in close proximity or even colocalized in MIPs, when these signals may in fact be much more distant from one another. Thus, there is a need to develop computationally inexpensive methods to analyze larger 3D imaging datasets on a slice-by-slice basis to avoid artificially superimposing signals.

In contrast to automated image quantification, manual analysis allow the user to evaluate each Z-plane and interpret images that may be of lower quality or variable signal-to-noise ratio. While this approach may yield a more accurate assessment of each image, manual analysis methods can present challenges with reproducibility, as image and signal interpretations may vary from user to user [34]. Furthermore, manual quantification of large image datasets can be inefficient and time-consuming. For example, performing ImageJ [33] colocalization analysis for image stacks using MIPs, or in a more rigorous slice-by-slice manner, can incur an extensive time-cost for image preparation and analysis. In addition to being unfavorable ergonomically, these methods can also distract researchers from experimentation and data collection. Software platforms exist that will analyze volumetric data (e.g. Imaris©); these options are unfortunately expensive monetarily and require intensive user training for confident implementation. Deconvolution is another method that can reconstruct 3D image sets using algorithms that numerically compensate for the limitations of diffracted light, achieving enhanced image resolution in all three dimensions and at lower levels of light

intensity [35]. While deconvolution platforms yield images of sharper quality and clearer visualization, the analytical methods to generate quantitative data are based on the same raw images provided to deconvolution algorithms. Thus, we reasoned that developing computational methods to analyze raw image datasets would provide assessment tools to complement current visualization enhancement platforms.

To that end, we developed InSite: a user-friendly MATLAB program to quantitatively analyze complex, volumetric imaging datasets for multi-signal colocalization and proximity. This program will also allow us to report our specific analysis parameters and provide raw image datasets upon request, enhancing scientific rigor, transparency, and reproducibility. This largely automated platform adapts to signal variability through the depth of an image stack, and addresses the need for an efficient, high-throughput, and high fidelity approach to volumetric analysis of large imaging datasets. We tested InSite by applying datasets acquired from our specific research interest, namely the cellular and molecular composition of the blood vessel wall.

MATERIALS AND METHODS

Software Requirements

MATLAB analysis was performed utilizing MATLAB R2017 with the Image Processing Toolbox on a Dell Precision T1700 computer with an Intel core i7-4770 CPU 3.40 GHz processor, 64-bit operating system, and 32.0 GB of random-access memory (RAM). Microsoft Office 2016 was also installed for exported slice by slice and batch analysis

results (into Microsoft Excel). The operating system utilized was Windows 10 Enterprise OS 2016.

Manual Image Analysis

Manual image analysis was conducted with ImageJ/FIJI software available for download at https://fiji.sc/ [36]. Color channels were separated, and the green channel/cell (e.g. endothelial cell) and red channel/cell (e.g. pericyte) area were determined through application of a pixel intensity threshold value. Regions of overlap between red and green signals were established, and pixel areas of these overlapping regions were quantified. The percent of red cell proximity to green was calculated by dividing the area of red-green overlap by the total green channel area.

***In Vivo* Models**

All animal experiments were conducted with review and approval from the Virginia Tech IACUC. All protocols were reviewed and approved by IACUC boards. The Virginia Tech NIH/PHS Animal Welfare Assurance Number is A-32081-01 (expires 7/31/2021).

Briefly, mouse breeding was conducted with *Flk1-eGFP; Ng2-DsRed* males and C57BL/6 female mice. At postnatal day 1 (P1), P3, and P7, pups were sacrificed via asphyxiation by isoflurane and an approved secondary method (i.e. thoracotomy). Tissues were fixed by injecting 2-3 mL of 4% paraformaldehyde (PFA) through the right ventricle. Eyes and brains were removed and fixed in 4% PFA overnight before transfer to Dubecco's phosphate buffer saline (PBS) solution for storage until further processing.

Brain Tissue Processing and Immunostaining

Brains were removed from PBS and cut by vibratome into 100 µm-thick sections. Separate sections were placed in PBS in 24-well plates for immunostaining. Brain sections were exposed to a blocking solution for 1 hour at room temperature with PBS and 1% Triton X-100 plus 1.5% normal donkey serum (PBS-T+NDS). Blocking solution was removed and replaced with primary antibody solution overnight at 4°C. Tissues were washed 4 times with PBS-T for 10-15 min each, and secondary antibody solution was added for 4 hours at room temperature on a nutator. Primary antibodies used in brain section incubations include: rat anti-mouse platelet derived growth factor-β (pdgfrβ, Invitrogen, #14-1402-81, 1:1000), goat anti-mouse platelet-endothelial cell adhesion molecule-1 (PECAM-1, R&D Systems, #AF3628, 1:200), goat anti-mouse type IV collagen (Millipore, #AB769, 1: 200), and rat anti-mouse glial fibrillary acidic protein (GFAP, Millipore, #AB5804, 1:1000). Secondary antibodies used were: donkey anti-rabbit AlexaFluor 568 (Thermo Fisher, #A10042), donkey anti-rat DyLight 550 (Thermo Fisher, #SA5-10027), donkey anti-goat 488 (Jackson ImmunoResearch, #705-545-147) and donkey anti rabbit 647 (Jackson ImmunoResearch, #711-605-152), all with 1:1000 concentrations. Sections mounted on glass slides were imaged with 20x (air) and 40x (water) objectives on a Zeiss LSM 880 confocal microscope, with the number of Z-slices ranging from 40-85.

Retina Tissue Processing and Immunostaining

Eyes were fixed by whole animal perfusion with 0.5% PFA followed by immersion in 2% PFA for 2 hours at room temperature. Following PBS rinse, retinas were dissected from

the whole eye and immersed in 100% cold ethanol for 30 mins. Retina tissues were then rinsed with PBS containing 1% Triton X-100 (PBS-T) for 30 mins at room temperature, and blocked in 3% NDS in PBS-T for 1 hour at room temperature. Primary antibody incubation was performed in PBS-T overnight at 4°C with isolectin GS-IB4 conjugated to AlexaFluor 488 (Molecular Probes, #I21411, 1:100), mouse anti-alpha-smooth muscle actin (αSMA) conjugated to Cy3 (clone 1A4, Sigma, C6198, 1:200), and rabbit anti-mouse neural glial antigen-2 (NG2, EMD Millipore, AB5320, 1:200). Secondary antibody incubation was also in PBS-T overnight at 4°C with donkey anti-rabbit AlexaFluor 647 (Jackson ImmunoResearch, 711-605-152, 1:400). Retinas were washed 3 times for 5 mins in PBS-T, flattened and mounted on slides in 50:50 PBS: glycerol with 1.5 coverslips. Images of retina whole mounts were acquired with a Zeiss LSM 880 confocal microscope with a 40x objective, and 10-15 Z-axis confocal scans were acquired.

RESULTS

Program Design

Signal colocalization is a useful metric for the study of specific cellular interactions, how these interactions affect particular cells, and thus the homeostasis of a tissue or system. Imaging techniques, particularly those with higher resolution, can provide insight into signal colocalization in the strictest sense, that is, being defined by a signal voxel occupying the exact X, Y, Z coordinates in space as another voxel. Signal co-distribution in spatially proportionate patterns may also be identified with these imaging modalities [37, 38]. MIPs, which are often used in microscopy image analysis, will often

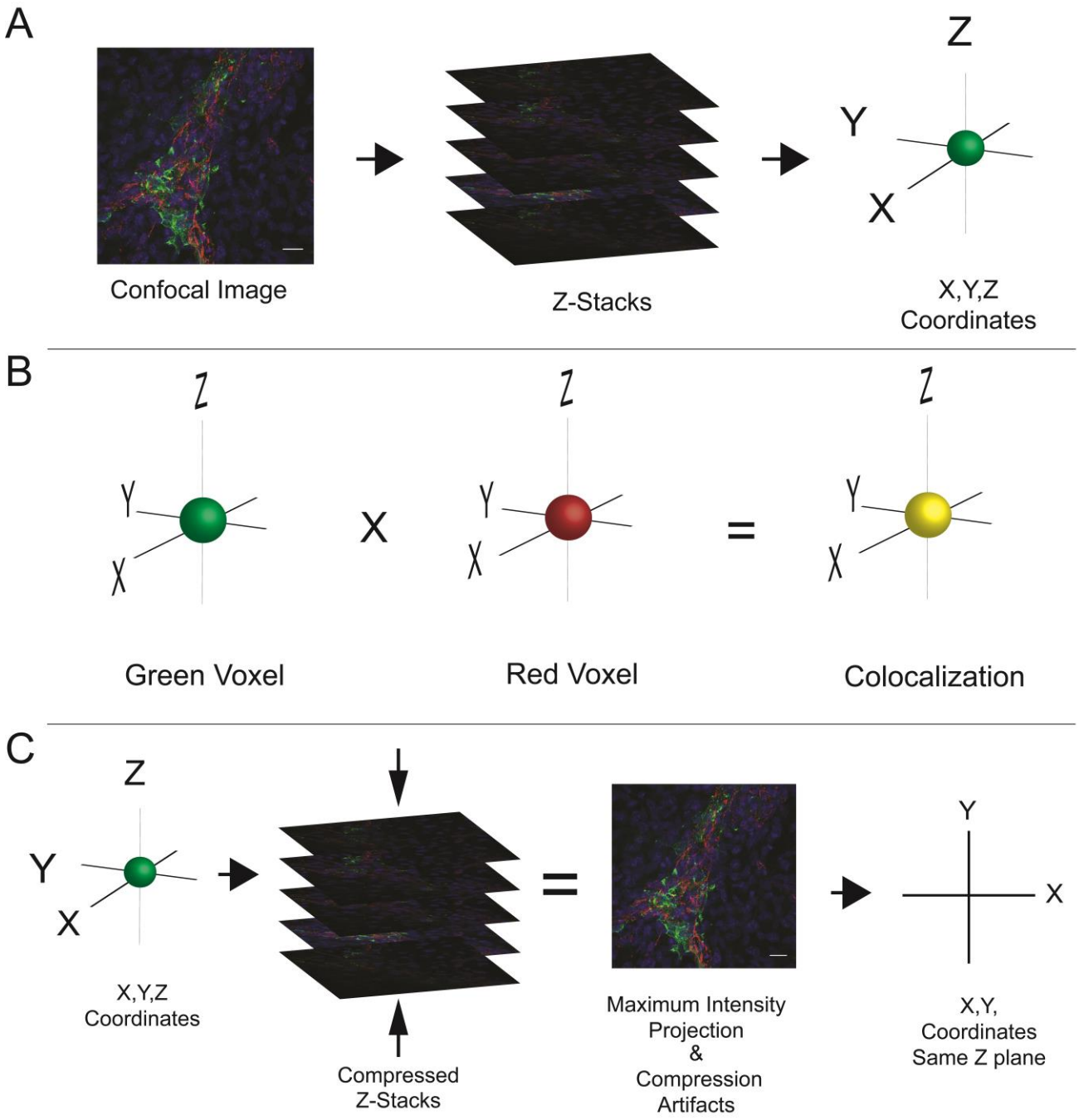

Figure 2. Acquisition and traditional preparations of multidimensional images from laser microscopy and analysis. **A** Schematic of how volumetric images are acquired from viewing a region of interest to capture and the setting of Z-depth range. **B** Schematic of true colocalization being the occupying of the exact same X,Y,Z coordinates in space of two voxels. **C** Schematic of traditional preparation of multidimensional images from volumetric to losing data and introduction of bias by being compressed into the visualization plane. Scale bar is 20µm.

overestimate colocalization due to the Z-stacks being compressed into the same plane, causing signals of interest to be artificially superimposed (Figure 2). InSite was designed to receive a Z-stack of images into the program and recombine those images to form the full image obtained during acquisition, maintaining the original tissue volume. For example, InSite will analyze 16-bit files in TIFF format with 2 color channels, often red and green pseudo-coloring for signals of interest (e.g. green for endothelial cells, and red for vascular pericytes in our research). The user can quantify the degree of direct colocalization of the red channel with the green channel (e.g. direct pericyte coverage along the endothelium). Images from one Z-stack must be processed, saved in the TIFF format, and stored in a folder containing the individual Z-stack images before loading the raw images into the program. The user then selects the folder containing the image stack TIFF sequence to import into MATLAB and initiate analysis.

After initiation, the user selects a polygonal region of interest (ROI) using the designated interface tools. The selected ROI is then utilized for all subsequent analyses performed on that loaded set of images. In our experience, increases in the depth of imaging presented a near-ubiquitous challenge in overcoming signal-to-noise and, in some cases, signal weakening or loss. To address this concern, InSite computes a depth-based intensity threshold (DBT) value, which adjusts the intensity threshold based on the depth of the image stack (e.g. image slice). Our underlying assumption was that signal loss follows an approximately linear correlation with increasing imaging depth during acquisition. Therefore, the maximum possible intensity value for a given voxel after applying a threshold value is modified based on the depth of the image (i.e. as a function of image slice number). InSite determines the linear relationship by

calculating a line-of-best-fit between the maximum intensity recorded for the most superficial and deepest slices as a function of image slice. By comparing the “brightest” first slice and the “weakest” last slice, the line-of-best-fit will change based on the number of slices or depth e.g. a 15-slice image stack will have a more gradual line slope, where as a 75-slice image stack will likely have a more drastic slope. This feature allows the user to scroll through imported image stacks to visually assess the implementation of intensity threshold values. Furthermore, post-threshold images viewable on the software user interface incorporate the applied DBT value based on user selection. This feature of real-time feedback on the graphical user interface assists the user in selecting intensity thresholds that best capture the intended data (Figure 3). To determine post-threshold voxel colocalization among red (e.g. pericyte) and green signals/cells (e.g. endothelial cells), voxels are scanned in the post-threshold image stack for each channel. The presence of signal in both the red and green channel of a voxel will be considered positive signal colocalization outcomes (Figure 3).

Colocalization metrics facilitate the analysis of potentially near overlapping or closely associated structures or proteins. In addition, signals or cells in close association or spatial proximity may not present as an overlapping structure. Based on the microscopic separation present between cells, image dilation was justified as a process to more accurately capture the “proximity” or close association of signals or cells in a system. Prior to determination of voxel overlap, the selected red channel undergoes dilation in all three dimensions (Figure 3). This procedure is implemented to address potential signal-signal or cell-cell separation, aiming for a more precise

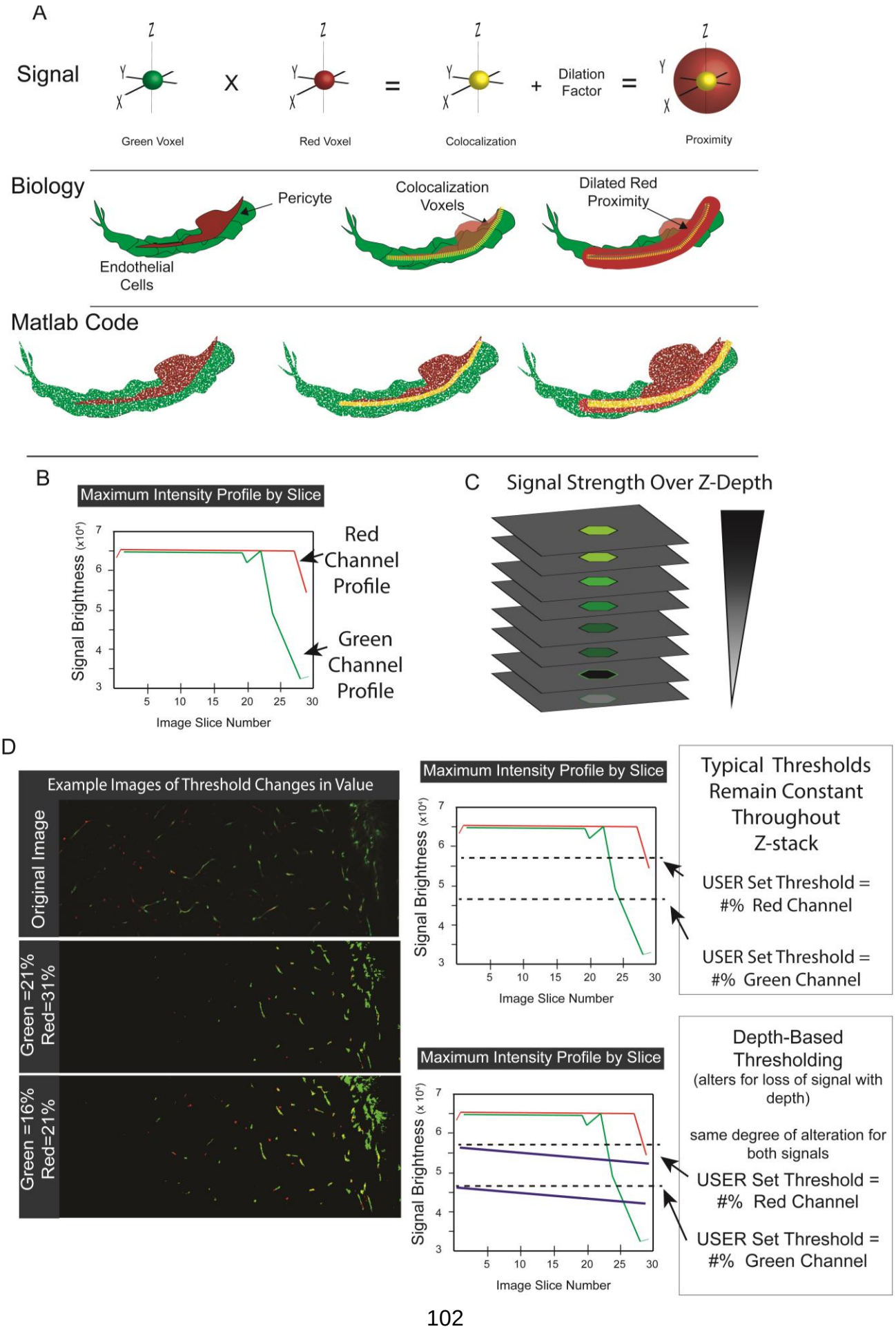
A
Signal
Green Voxel
X
Red Voxel
=
Colocalization
+
Dilation Factor
=
Proximity
Biology
Pericyte
Endothelial Cells
Colocalization Voxels
Dilated Red Proximity
Matlab Code
B
Maximum Intensity Profile by Slice
Signal Brightness (x10⁴)
Red Channel Profile
Green Channel Profile
Image Slice Number
C
Signal Strength Over Z-Depth
D
Example Images of Threshold Changes in Value
Original Image
Green =21%
Red=31%
Green =16%
Red=21%
Maximum Intensity Profile by Slice
Signal Brightness (x10⁴)
Image Slice Number
Typical Thresholds Remain Constant Throughout Z-stack
USER Set Threshold = #% Red Channel
USER Set Threshold = #% Green Channel
Maximum Intensity Profile by Slice
Signal Brightness (x 10⁴)
Image Slice Number
Depth-Based Thresholding
(alters for loss of signal with depth)
same degree of alteration for both signals
USER Set Threshold = #% Red Channel
USER Set Threshold = #% Green Channel

Figure 3. Representative schematic of InSite program descriptions. **A** Diagram of how InSite determines metrics of colocalization and proximity. The true signal or voxel of an image is capture to determine colocalization by occupying the same coordinate in space. With the addition of a dilation factor that expands the red channel voxels in all three dimensions, proximity can be quantified. **B** InSite quantifies the maximum signal intensity of each Z-slice throughout the image stack to allow for visualization of threshold changes with increasing slice number or depth. **C** Signal strength decreases with depth in an estimated linear fashion. Automated depth based threshold (DBT) is programmed into InSite to account for this loss of signal. **D** Changes in threshold values can be seen in real-time in comparison to the original loaded image stack to accurately determine thresholds for analysis.

estimation of cell "coverage" in a given tissue or system. This dilation procedure generates a new image stack that is utilized for the purposes of determining proximity; colocalization analysis is also performed on both dilated and non-dilated image stacks, thereby giving results for both quantifications after analysis (Figure 6).

As users generate proximity and co-localization data with this platform, it is critical to couple a basic understanding of the observed biology with InSite results to yield logical interpretations. In instances of low percentage of true colocalization, proximity may be useful to incorporate into an understanding of these spatial relationships between discrete elements (e.g. cell distribution, patterns of association, etc.). The results for colocalization may be a low percentage, but the proximity results may yield a mid-range to higher percentage (i.e. 3% versus 25-60%), which may inform a biological perspective. An example from our research interests in vascular biology is the association of the extracellular matrix (ECM)/basement membrane relative to vascular pericytes along vessels as well as to neighboring astrocytic end-feet in the retina and brain. ECM colocalization outcomes are often around 80-100%, and proximity measures are near 100%, which matches the known biology of ECM that ensheathes blood vessels. In a contrasting scenario, pericytes or astrocyte end-feet

may only have a 2-3% true signal colocalization but may have a 20-30% proximity, as only part of these cellular components actually come in direct contact with vessels.

Validation

Angiogenesis requires the formation of tip cells that then recruit pericytes to stabilize the vessels [39-41]. We focused on this stage of vascular remodeling to study pericyte coverage of the microvasculature in normal and pathological contexts as well as in the developmental setting. MIPs were generated in ImageJ [33] software and analysis of colocalization performed, as well as red (pericyte) proximity using the area of post-threshold channels. This type of analysis was considered as a main method of validating our program due to the consistent use of MIPs for analysis in the field. In a survey for microscope users, 84.3% utilized 2D MIPs to visualize 3D datasets [42]. For a more in-depth analysis validation, manual analysis of individual Z-slices was conducted for entire images for both colocalization and proximity. Slice-by-slice analysis of an image could be considered a gold standard in contrast to MIPs due to each slice being visually assessed for positive signal colocalization. Although each Z-slice is analyzed individually and thus makes the analysis more thorough, there is a higher likelihood of the introduction of bias in the determining threshold values to overcome signal-to-noise ratios. This bias can be further exacerbated with variations in selected threshold values at each slice depending on the ability to record and reproduce exact threshold values.

For validation, multiple image types were analyzed using the above methods to compare with analysis by InSite. Genetic excision of vascular-related genes used as models of gene mutation conditions, as well as early developmental interactions in brain

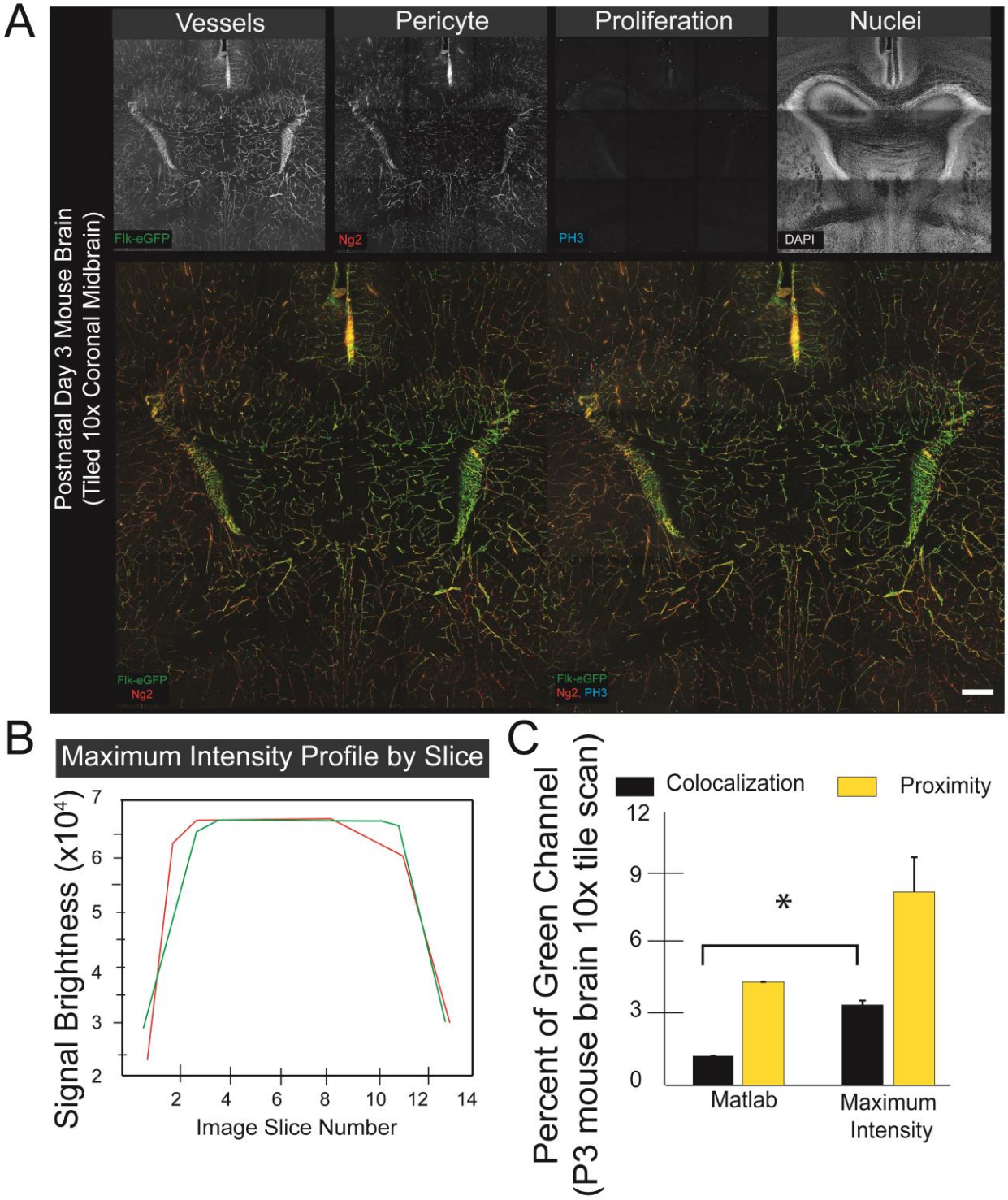

Figure 4. Example complex multidimensional image of the mouse brain at postnatal day 3. **A** Representative image of each channel captured in the brain of P3 mouse, vessels with Flk-eGFP fluorescent reporter, pericytes with NG2 fluorescent reporter, proliferation with phosphor-histone 3 (PH3), and dapi as a nuclear marker. Scale bars, 100 µm. **B** Example of maximum signal for each channel changes over image depth. **C** Quantification of differences in colocalization and proximity by automated InSite analysis versus manual MIP using ImageJ.

and retinal tissues were used for large dataset comparisons. Tissues from mouse brain and retinas from various ages were used in this analysis. To study developmental interactions, multiple images were used to validate the effectiveness of our program. *In vitro* assays consisting of mouse embryonic stem cells (ESCs) differentiated to form vessel-like structures and pericyte coverage, as well as ECM arrays with human umbilical vein endothelial cells (HUVECs) and NG2+ pericytes were used for cellular comparisons between analysis methods (See Supplemental Materials).

All validation test images were prepared into TIFF files using Zen Black software (Zeiss) for full resolution images in multiple planes to combine channels for analysis together for every Z stack i.e. multiple Z-stacks were represented by 1 image per slice by using Zen software, Zen Black. Red and green pseudo-coloring was applied to images, usually with endothelial cells represented in the green channel and pericytes or other targets such as ECM components or glial cells were assigned to the red channel.

Images were first manually analyzed using MIPs in ImageJ [33] software to determine colocalization and proximity (or “coverage”) of the signal in the red channel. After MIP analysis, images were uploaded into InSite to assess signal loss with depth and determine appropriate threshold values (Figure 4). Comparison of both methods revealed an overestimation by MIP-based analysis compared to volumetric analysis by InSite, as expected. Manual analysis of individual Z-slices yielded extreme variation in colocalization and proximity values compared to InSite outcomes, with general overestimation for each z-slice (Figure 5).

Workflow

Materials needed:

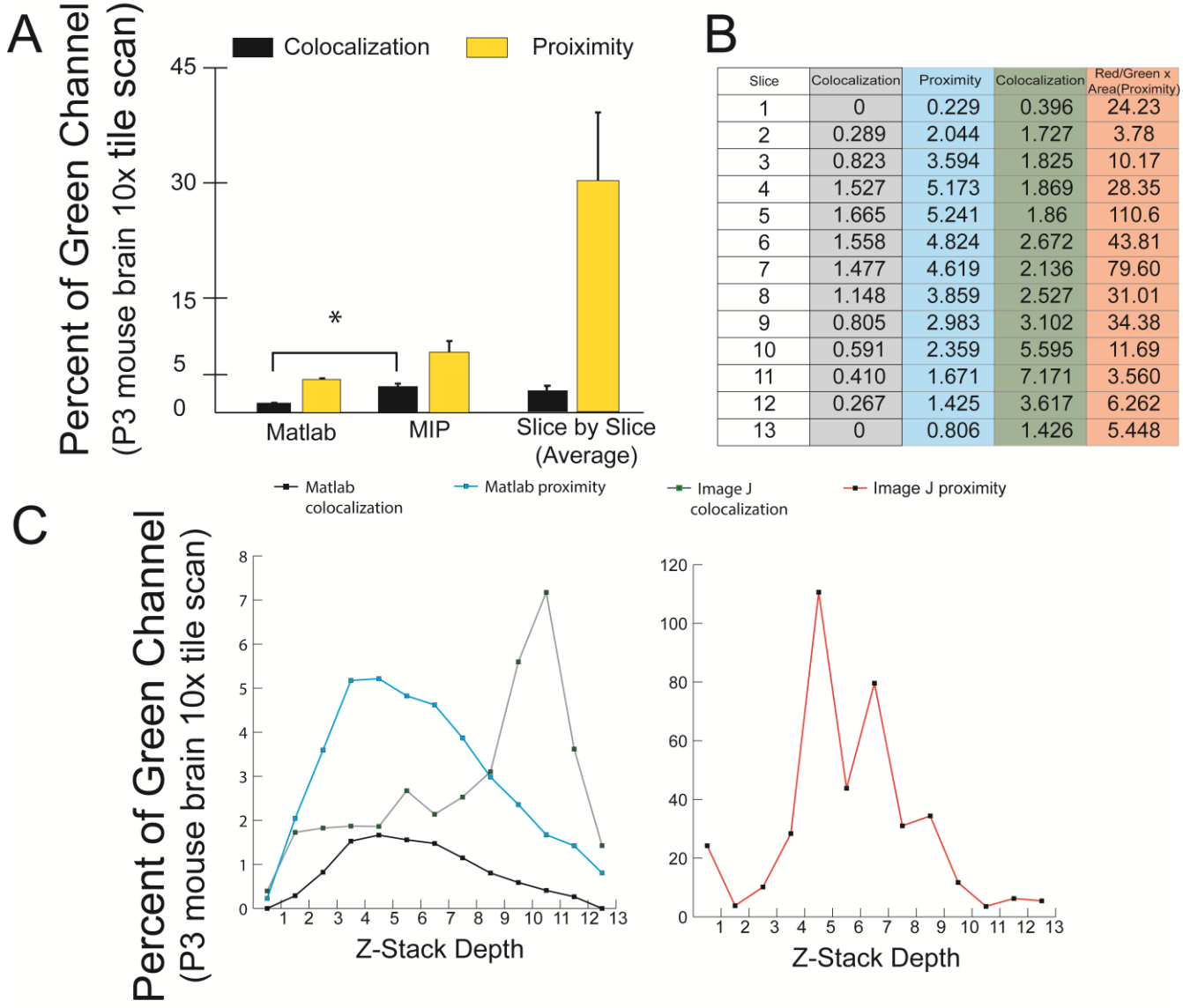

Slice	Colocalization	Proximity	Colocalization	Red/Green x Area(Proximity)
1	0	0.229	0.396	24.23
2	0.289	2.044	1.727	3.78
3	0.823	3.594	1.825	10.17
4	1.527	5.173	1.869	28.35
5	1.665	5.241	1.86	110.6
6	1.558	4.824	2.672	43.81
7	1.477	4.619	2.136	79.60
8	1.148	3.859	2.527	31.01
9	0.805	2.983	3.102	34.38
10	0.591	2.359	5.595	11.69
11	0.410	1.671	7.171	3.560
12	0.267	1.425	3.617	6.262
13	0	0.806	1.426	5.448

Figure 5. InSite reduces high variability introduced in manual analysis techniques. **A** Quantification of colocalization and proximity metrics using automated InSite versus manual analysis techniques MIP and individual Z-slice analysis for one image stack. Minimum of 3 analysis completed for comparisons for InSite and MIP. Values are averages +SEM *P≤0.05 vs. MIP. **B** Table of metrics at each individual Z-slice representing the high variability of automated versus manual analysis that introduces user bias in each slice. **C** Graphical representation of table in B.

- Laser microscopy system (e.g. Zeiss LSM880)
- Microscopy software (e.g. Zen Black 2.3, Zeiss)
- Computer with 32+GB RAM
- MATLAB R2017
- Microsoft Excel 2016

Preparation: 1-2 mins

Red and green pseudo coloring was applied to images in the accompanying microscopy software from Zeiss, Zen black, usually with vessels being the green channel and pericytes or other interests such as ECM components or glial cells in the red channel. All images were exported into TIFFs for full resolution series images. This method of export allows combination of both red and green channels in every z-stack. Zen was used over ImageJ to create TIFFs that had both channels in each slice image versus the channels remaining separate, which could not be used for colocalization analysis.

Program:

Opening InSite resulted in the appearance of the MATLAB command window. Selecting “Run” prompted the appearance of the graphical user interface (GUI) for pericyte tool code. GUI options allows for two methods of analysis – using individual folders for a more thorough analysis of 1 image by slice by slice computation for colocalization and coverage, or batch analysis that selects a folder that contains multiple images in TIFF folders.

1a. First select whether the user intends for individual image or batch image analysis after prompting for the pop-up message in MATLAB. For individual analysis upload a single folder that contains the TIFFs of 1 image Z-stack. MATLAB loads the images from the selected folder quickly and progress can be monitored in the main MATLAB command window (Figure 6).

2a. After loading an image folder, the user must select a region of interest (ROI) to be analyzed. Once outlined, the program will crop all z-slices to the ROI selected. After cropping is complete, the percent area of the ROI will be presented in the command window. The interface will update to display the selected ROI (Figure 6).

3a. User selects “Masking Analysis” option on the GUI to begin analysis of signal intensity loss with depth and determine appropriate thresholds for the image stack. Users can visualize the changes in the image to be analyzed in real-time by typing in a percent threshold and hitting enter to apply the changes for each channel. Additionally, both the original image and to be analyzed image may be scrolled through in real-time to visualize changes in threshold throughout the Z-stack. At this time the user can also set the dilation factor to compute cell proximity.

4a. Once satisfied with thresholds and dilation factor settings, the user must select “Proceed with Analysis” on the GUI. Progress for the colocalization and proximity analysis are visible in the MATLAB command window, as well as indicated on a wait

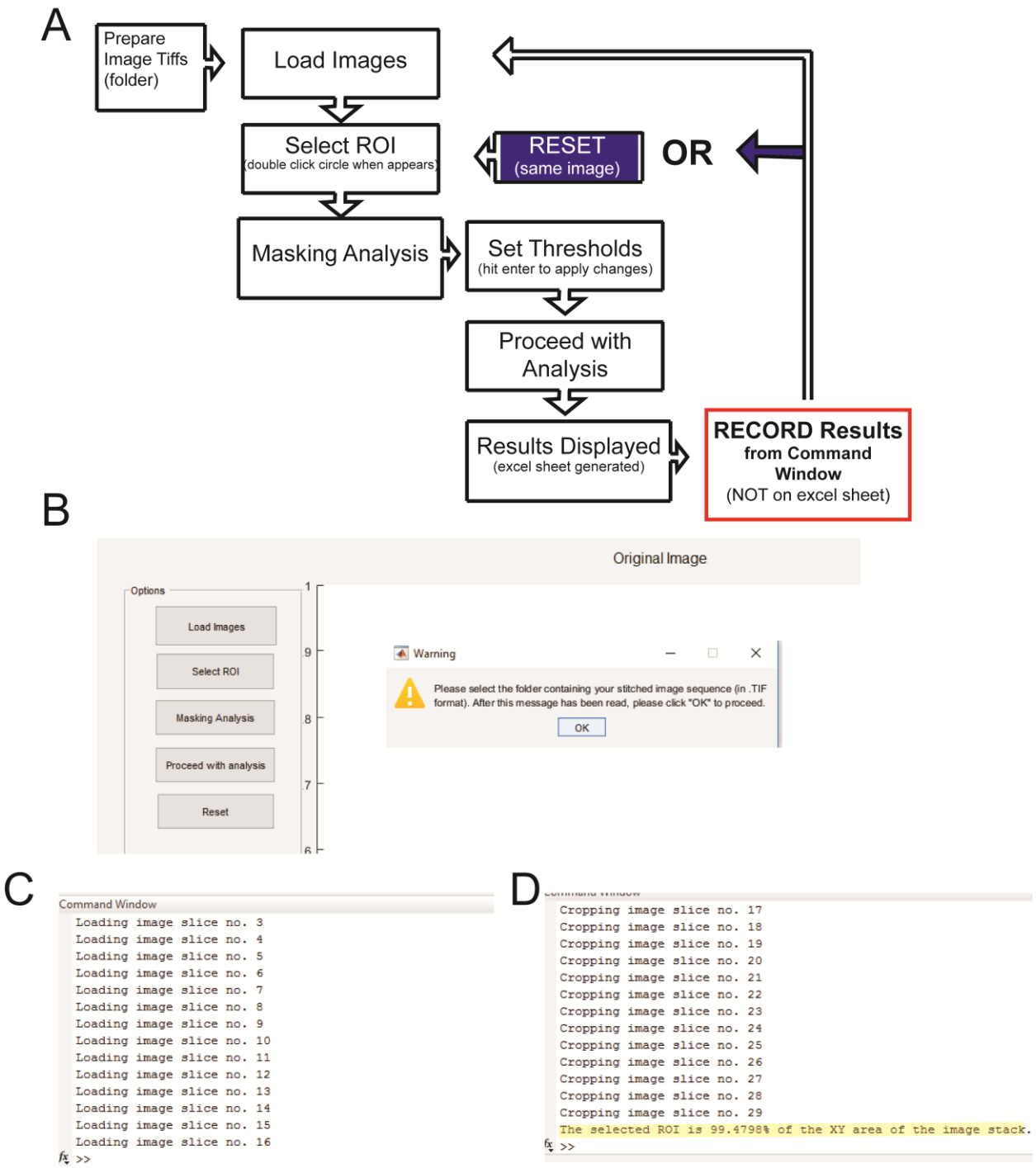

Figure 6. Representative images of InSite programming. **A** Schematic InSite workflow for the user. **B** Representative image of InSite prompt for loading folder with image stacks. **C** Image of end of loading stage and ability to proceed to next stage of ROI selection. **D** Image of the end of cropping ROI stage. End statement of percentage of ROI to original image stack is indicator of ability to proceed to masking analysis stage.

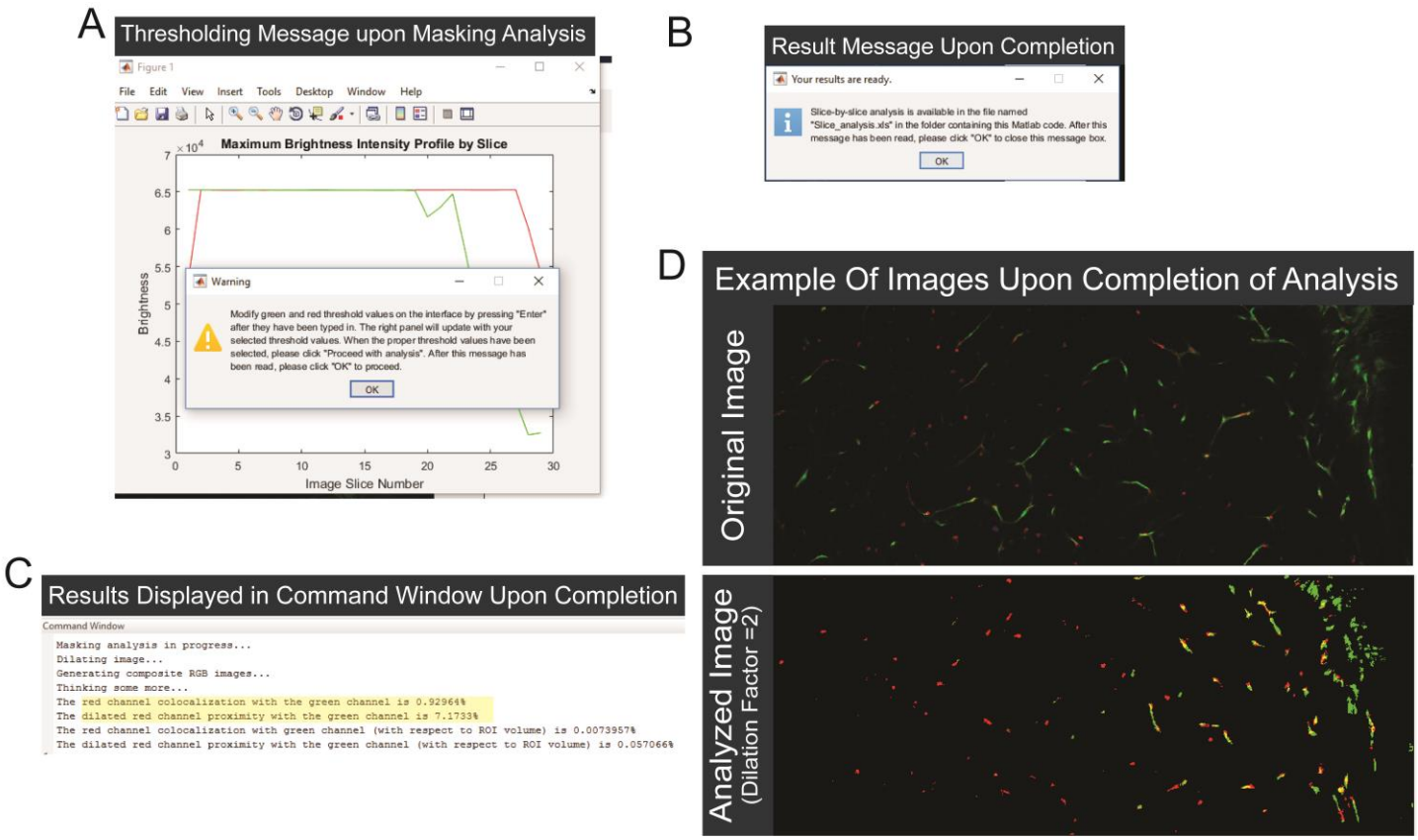

Figure 7. Representative images of prompts and readouts of InSite throughout program analysis. **A** Signal changes with depth is first readout from Masking Analysis used to help determine appropriate thresholds to proceed with analysis. **B** Message upon completion of individual image stack analysis indicating the generation of an excel sheet detailing metrics at each Z-slice. **C** Readout of the metrics for the entire image Z-stack at end of analysis. **D** Representative images of the original image stack loaded versus the image stack that was analyzed by MATLAB program at the end of analysis. Analyzed image shows the threshold values with the addition of the red channel dilation factor that was ultimately analyzed for the analysis of colocalization and proximity.

bar. Typical time to analysis depends on the file size, usually between 30 seconds to 2 minutes.

5a. The results from the Z-stack are given in the command window giving the colocalization, proximity, and these two measures in regards to ROI volume (Figure 7). There is also an excel file generated for the slice-by-slice analysis values of colocalization and proximity that automatically saves to the InSite main access folder ("Slice by Slice Analysis").

1b. If the user wishes to do batch analysis, MATLAB asks the user to input dilation factor and green/red threshold values. The user then selects a prepared folder that contains folders of TIFFs with 1 complete image per folder. MATLAB loads and analyzes these image folders sequentially. After analysis is complete, an excel file is generated for the results that automatically saves to the InSite main access folder ("Analysis Results"). Typical time to run this type of batch analysis is 2 minutes for a folder of 1.69 GB data or 3 image folders at a time.

DISCUSSION

Understanding certain disease states can benefit from reductionist models, usually *in vitro* or *in vivo* models, which can be used to characterize morphologically normal and irregular (e.g. pathological) conditions. These systems often involve the analysis of more than one element, requiring an integrated consideration of multiple components that interact to form functional systems. Insight into these interactions on a molecular,

cellular, and tissue level can provide clues for developing novel therapeutic interventions. In the field of vascular biology, endothelial cells interact with support cells, such as pericytes, and surrounding ECM that composes the vascular basement membrane. These interactions are critical during phases of development, stabilization and homeostasis, and wound repair, with dysfunction often leading to the onset and progression pathologies. Angiogenesis involves sprouting endothelial cells interacting with recruited pericytes, as well as the deposition of the vascular basement membrane to stabilize a maturing microvascular network. When one of these components fails, consequences can be severe; for example, pericyte “drop-out” is believed to be a contributing factor to progression of proliferative diabetic retinopathy [43, 44].

Investigating the mechanistic determinants underlying physiological and pathological processes requires technological advances that allow researchers to visualize and interpret data in new ways. Until the advent of imaging technologies capable of more precise volumetric rendering, visualization was often performed, and images analyzed, as single-plane images or using MIPs to examine morphology. Although useful, MIPs are Z-stacks compressed into a single Z-plane, thus inherent in this method is the tendency toward false positives in colocalization metrics. The “gold standard” for our comparison was the manual slice-by-slice analysis where each Z-stack was analyzed separately, for threshold value determination and signal colocalization. Although this approach tends to be more accurate by reducing the false positives of compression, it also produces a high degree of variability (Figure 5) owing to the subjectivity in determining threshold values for Z-stacks toward the upper and lower ranges of the image stack. Most datasets are acquired such that a small margin of

less intense/less focused images are taken above and below the desired ROI captured by confocal microscopy (Figure 8). This margin for focal error introduces variability in signal interpretation and analysis from user-to-user and from image-to-image. Because InSite accounts for this variability, analysis by our program is less influenced by any differences in margin acquisition and therefore introduces less variability into the statistical analysis of outcomes metrics.

The largely automated nature of image analysis by InSite reduces user variability and bias, and enhances reproducibility by recording the exact threshold value and dilation factor used for each image. InSite uses one threshold value for the entire image for every Z-stack (i.e. no within-image heterogeneity) for consistent and rigorous quantification of colocalization and proximity. Also, the program is designed to present the user with threshold values that “adapt” to the signal-to-noise ratio throughout the entire Z-stack. This information provides a more accurate estimate of the threshold values to use, as well as indicating any changes that occur for each channel. Adjusting threshold values for the deeper Z-stack images (and larger number of slices), InSite employs a depth-based threshold (DBT) to compensate for signal loss with image depth. If the threshold values drops severely at more superficial slices within the Z-range, it will be important for the user consider restructuring and/or reacquiring an image stack so that there will be more confidence in the analysis and accuracy for threshold values applied.

Setting a reliable and accurate threshold can be difficult in some types of images due to the manner of acquisition, resulting in high variation within the results. There are several reasons for differences in colocalization and proximity in a similar type of image.

Common differences in image acquisition settings (e.g. objective magnification, laser power, master gain, signal offset, and Z-range) contribute to variance in threshold values used for analysis. Other factors such as the excitation wavelength used (i.e. 488 nm vs. 568 nm vs. 633 nm) and whether an image was acquired in tile-mode or one single field-of-view also account for variations in threshold values. During program validation, we observed that imaging with the 568 nm laser yielded a more robust signal with a more constant intensity through the Z-depth, even in imaging the same cell type but with a different excitation wavelength. Across imaging modalities, end-users will need to consider these details to maximize the output from InSite analysis.

Finally, it is imperative that end-users familiarize themselves with InSite output metrics, as this is vital for more accurate biological interpretations of resulting data. Colocalization in the truest sense is the detection of a signal (i.e. voxel/pixel) in the exact 3D space as another signal. If the output from InSite has a moderate to low read out for colocalization (e.g. 3%), it may not necessarily mean that the biological entities are drastically separate from one another in space. It is well known for example that ECM components fully cover the outer surface of the blood vessel wall; however, InSite often indicated only 3% of the ECM as truly colocalized with vessel voxels. The key to interpreting this data is considering the context of the biological samples. The other metric -- proximity -- can be used as a complementary indication of the close association of specific molecules or cells. Again, in assessing ECM components along the vessel wall, we can set our dilation factor to account for the minor though real distance between the endothelium and the ECM. In this case, the proximity outcomes are higher (i.e. 99%), which is more congruent with an interpretation of the biology. As

A

	Maximum Intensity Projection	Slice by Slice	Matlab
What	Compressed Z-stacks	visual check of every Z-slice within a stack and manual computations	thresholded images in all 3 planes (keeping voume/Z-depth)
Coverage/ Colocalization	get more false positives due to compressed onfo one plane	depending on how do analysis will under or over estimate true values (i.e. decreasing threshold to get artificaial signals)	colocalization of voxels in exact x,y,z coordinates - accounts for space between cells/tissue to determine proximity
Z-Depth	none	forcing thresholding to visualize signals at ends of staclk to do manual analysis (decreasing thresholds where shouldn't)	keep z-depth and consistent thresholding throughout analysis- depth based thresholding
Usage	Most commonly used method	not well used but a gold standard because of rigorous checking of each Zslice	best for true values of colocalization can be used on anything with z-depth
Time	4 minutes per image	4 minutes per image slice x slice number (ex 13) = 52 mins	2 minutes per image *batch analysis = 2 mins for 8 image stacks*

B

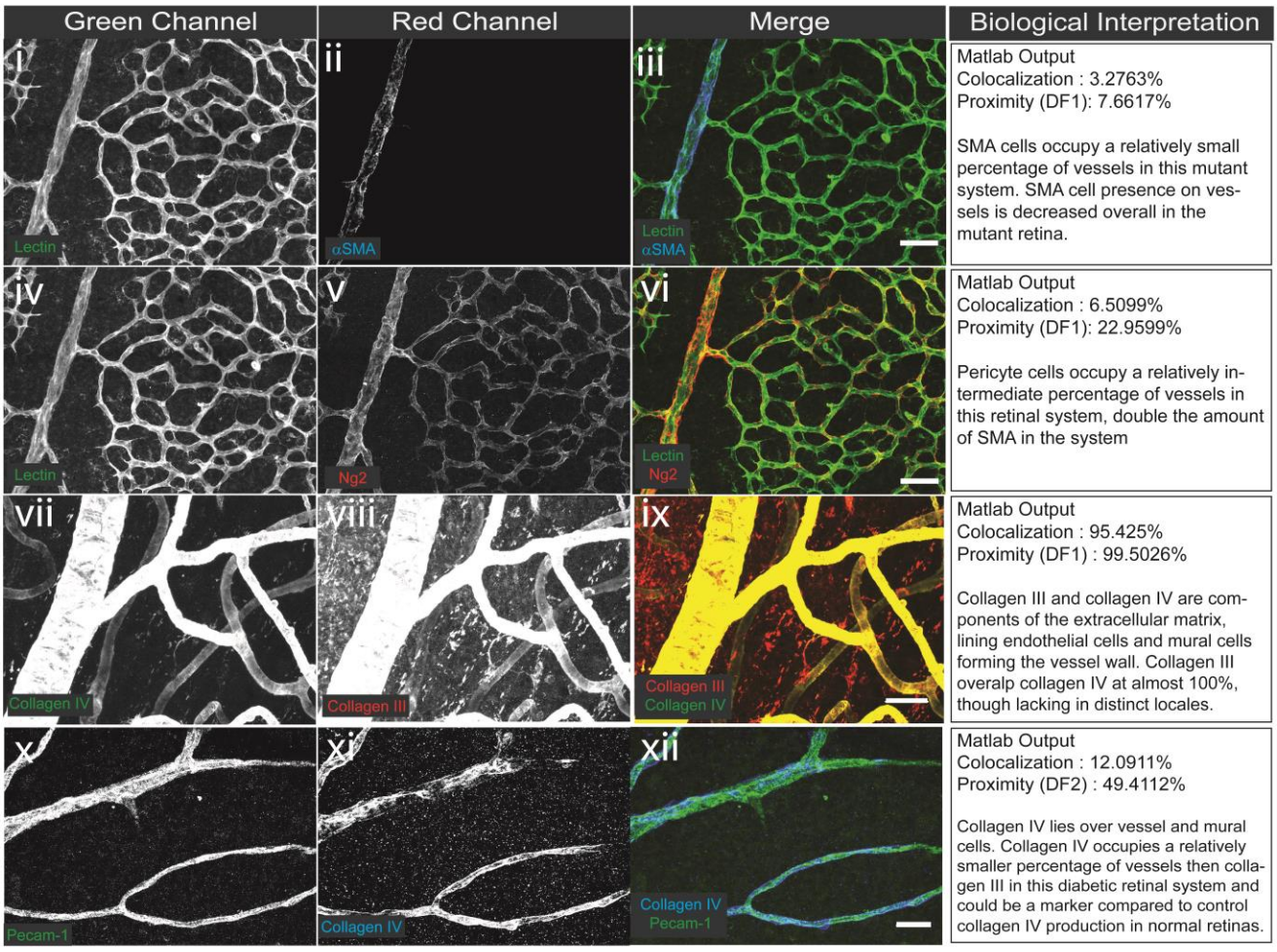

Figure 8. Summary of integrity and fidelity of InSite program. **A** Table outlining the differences in manual analysis methods versus the automated method of novel InSite program. **B** Representative images of various biological samples for example interpretations of InSite metric outputs. Images i-vi of mouse retina staining with lectin for vessels and alpha-smooth muscle actin (αSMA) for vascular smooth muscle cells or NG2 for pericytes. Scale bar is 50µm. Images vii – ix of human diabetic retina staining with collagen IV and III for ECM components. Scale bar is 100µm. Image x-xii of mouse brain. Staining of PECAM-1 for endothelial cells and type IV collagen. Scale bar is 50µm.

with many morphological quantification strategies, thoughtful consideration of the biological context is important for interpreting output measurements from InSite. In doing so, colocalization and proximity can provide rigorously assessed metrics for establishing key differences across biological samples (e.g. examining multiple components of the vascular ECM/BM in pathological conditions vs. healthy) (Figure 8).

Image acquisition and data analysis can be a time-consuming and manually-driven processes, and this presents a challenge with respect to current imaging modalities in designing easy-to-use analytical tools that can adapt to differences across specimens. Image analysis will always rely on a level of user interpretation and input for parameter selection and implementation, which may introduce a bias in quantification. With InSite, however, we aimed to develop a largely automated and adaptive image analysis algorithm that addresses the needs of efficiency, high-throughput, and fidelity, creating a tool for biological researchers using optics-based microscopy as well as anyone interested in the rapid analysis of comprehensive, multi-signal datasets.

REFERENCES

1. Garg, S. and S.D. Biju, *Molecular and Morphological Study of Leaping Frogs (Anura, Ranixalidae) with Description of Two New Species.* PLoS One, 2016. **11**(11): p. e0166326.
2. Olivares, A.M., et al., *Animal Models of Diabetic Retinopathy.* Curr Diab Rep, 2017. **17**(10): p. 93.
3. Arreola, A., et al., *Von Hippel-Lindau mutations disrupt vascular patterning and maturation via Notch.* JCI Insight, 2018. **3**(4).
4. Darden, J., et al., *Excess vascular endothelial growth factor-A disrupts pericyte recruitment during blood vessel formation.* Angiogenesis, 2018.
5. Walpole, J., et al., *Agent-based Computational Model of Retinal Angiogenesis Simulates Microvascular Network Morphology as a Function of Pericyte Coverage.* Microcirculation, 2017.
6. Hammer, S., et al., *Multiple Retinal Axons Converge onto Relay Cells in the Adult Mouse Thalamus.* Cell Rep, 2015. **12**(10): p. 1575-83.
7. Liu, Y.Y., G. Ju, and M.T. Wong-Riley, *Distribution and colocalization of neurotransmitters and receptors in the pre-Botzinger complex of rats.* J Appl Physiol (1985), 2001. **91**(3): p. 1387-95.
8. Stornetta, R.L., *Identification of neurotransmitters and co-localization of transmitters in brainstem respiratory neurons.* Respir Physiol Neurobiol, 2008. **164**(1-2): p. 18-27.
9. Masuda, T., et al., *Confocal laser microscopy of dystrophin localization in guinea pig skeletal muscle fibers.* J Cell Biol, 1992. **119**(3): p. 543-8.
10. Vistisen, B., et al., *Sarcolemmal FAT/CD36 in human skeletal muscle colocalizes with caveolin-3 and is more abundant in type 1 than in type 2 fibers.* J Lipid Res, 2004. **45**(4): p. 603-9.
11. McKell, A.O., L.E. LaConte, and S.M. McDonald, *A Temperature-Sensitive Lesion in the N-Terminal Domain of the Rotavirus Polymerase Affects Its Intracellular Localization and Enzymatic Activity.* J Virol, 2017. **91**(7).
12. Jung, B., et al., *Visualization of vascular mural cells in developing brain using genetically labeled transgenic reporter mice.* J Cereb Blood Flow Metab, 2018. **38**(3): p. 456-468.
13. Grant, R.I., et al., *Organizational hierarchy and structural diversity of microvascular pericytes in adult mouse cortex.* J Cereb Blood Flow Metab, 2017: p. 271678X17732229.
14. Sava, P., et al., *Human pericytes adopt myofibroblast properties in the microenvironment of the IPF lung.* JCI Insight, 2017. **2**(24).
15. Sava, P., et al., *Human microvascular pericyte basement membrane remodeling regulates neutrophil recruitment.* Microcirculation, 2015. **22**(1): p. 54-67.
16. Barry, D.M., et al., *Cdc42 is required for cytoskeletal support of endothelial cell adhesion during blood vessel formation in mice.* Development, 2015. **142**(17): p. 3058-70.
17. Bergers, G. and S. Song, *The role of pericytes in blood-vessel formation and maintenance.* Neuro Oncol, 2005. **7**(4): p. 452-64.
18. Morikawa, S., et al., *Abnormalities in pericytes on blood vessels and endothelial sprouts in tumors.* Am J Pathol, 2002. **160**(3): p. 985-1000.

19. Simons, M., et al., *State-of-the-Art Methods for Evaluation of Angiogenesis and Tissue Vascularization: A Scientific Statement From the American Heart Association.* Circ Res, 2015. **116**(11): p. e99-132.
20. Dave, J.M., et al., *Pericyte ALK5/TIMP3 Axis Contributes to Endothelial Morphogenesis in the Developing Brain.* Dev Cell, 2018.
21. Liebmann, T., et al., *Three-Dimensional Study of Alzheimer's Disease Hallmarks Using the iDISCO Clearing Method.* Cell Rep, 2016. **16**(4): p. 1138-1152.
22. Kuwajima, T., et al., *ClearT: a detergent- and solvent-free clearing method for neuronal and non-neuronal tissue.* Development, 2013. **140**(6): p. 1364-8.
23. Combs, C.A., *Fluorescence microscopy: a concise guide to current imaging methods.* Curr Protoc Neurosci, 2010. **Chapter 2**: p. Unit2 1.
24. Paddock, S.W. and K.W. Eliceiri, *Laser scanning confocal microscopy: history, applications, and related optical sectioning techniques.* Methods Mol Biol, 2014. **1075**: p. 9-47.
25. Nathan S. Claxton, T.J.F., & Michael W. Davidson. *Laser Scanning Confocal Microscopy*. in
. 2005.
26. Corliss, B.A., et al., *Methods to label, image, and analyze the complex structural architectures of microvascular networks.* Microcirculation, 2018: p. e12520.
27. Seaman, M.E., S.M. Peirce, and K. Kelly, *Rapid analysis of vessel elements (RAVE): a tool for studying physiologic, pathologic and tumor angiogenesis.* PLoS One, 2011. **6**(6): p. e20807.
28. Ding, Y., et al., *Light-sheet fluorescence imaging to localize cardiac lineage and protein distribution.* Sci Rep, 2017. **7**: p. 42209.
29. Cai, R., et al., *Panoptic imaging of transparent mice reveals whole-body neuronal projections and skull-meninges connections.* Nat Neurosci, 2019. **22**(2): p. 317-327.
30. Chappell, J.C., et al., *Local guidance of emerging vessel sprouts requires soluble Flt-1.* Dev Cell, 2009. **17**(3): p. 377-86.
31. Kappas, N.C., et al., *The VEGF receptor Flt-1 spatially modulates Flk-1 signaling and blood vessel branching.* J Cell Biol, 2008. **181**(5): p. 847-58.
32. Nesmith, J.E., et al., *Blood vessel anastomosis is spatially regulated by Flt1 during angiogenesis.* Development, 2017. **144**(5): p. 889-896.
33. Rueden, C.T., et al., *ImageJ2: ImageJ for the next generation of scientific image data.* BMC Bioinformatics, 2017. **18**(1): p. 529.
34. Riber-Hansen, R., B. Vainer, and T. Steiniche, *Digital image analysis: a review of reproducibility, stability and basic requirements for optimal results.* APMIS, 2012. **120**(4): p. 276-89.
35. Biggs, D.S., *3D deconvolution microscopy.* Curr Protoc Cytom, 2010. **Chapter 12**: p. Unit 12 19 1-20.
36. Schindelin, J., et al., *Fiji: an open-source platform for biological-image analysis.* Nat Methods, 2012. **9**(7): p. 676-82.
37. Bolte, S. and F.P. Cordelieres, *A guided tour into subcellular colocalization analysis in light microscopy.* J Microsc, 2006. **224**(Pt 3): p. 213-32.

38. Dunn, K.W., M.M. Kamocka, and J.H. McDonald, *A practical guide to evaluating colocalization in biological microscopy.* Am J Physiol Cell Physiol, 2011. **300**(4): p. C723-42.
39. Hellstrom, M., et al., *Role of PDGF-B and PDGFR-beta in recruitment of vascular smooth muscle cells and pericytes during embryonic blood vessel formation in the mouse.* Development, 1999. **126**(14): p. 3047-55.
40. Lindblom, P., et al., *Endothelial PDGF-B retention is required for proper investment of pericytes in the microvessel wall.* Genes Dev, 2003. **17**(15): p. 1835-40.
41. Seynhaeve, A.L.B., et al., *Spatiotemporal endothelial cell - pericyte association in tumors as shown by high resolution 4D intravital imaging.* Sci Rep, 2018. **8**(1): p. 9596.
42. Shihavuddin, A., et al., *Smooth 2D manifold extraction from 3D image stack.* Nat Commun, 2017. **8**: p. 15554.
43. Beltramo, E. and M. Porta, *Pericyte loss in diabetic retinopathy: mechanisms and consequences.* Curr Med Chem, 2013. **20**(26): p. 3218-25.
44. Murata, M., et al., *Selective pericyte degeneration in the retinal capillaries of galactose-fed dogs results from apoptosis linked to aldose reductase-catalyzed galactitol accumulation.* J Diabetes Complications, 2002. **16**(5): p. 363-70.

CHAPTER 4

Characterization and Comparisons of Vascular Maturation in Areas of Early Postnatal Mouse Brain

Jordan Darden[1,2]*, Clifton Jenkins-Houk[4]*, Karan Paralkar, Harsh Patolia[4], John C. Chappell[12,3,4]

[1]Center for Heart and Regenerative Medicine, Virginia Tech Carilion Research Institute, Roanoke, VA 24016, USA

[2]Graduate Program in Translational Biology, Medicine, and Health, Virginia Polytechnic Institute and State University, Blacksburg, VA 24061, USA

[3]Department of Basic Science Education, [4]Virginia Tech Carilion School of Medicine, Roanoke VA 24016

* Co-authorship

ABSTRACT

Vascular dysfunction plays an important role in a plethora of diseases, both initiation and progression. Within the blood brain barrier (BBB), the stages of vascular development must be carefully controlled by highly specific developmental programs with spatial-temporal cues. Previously, our research has shown that alterations in the vascular endothelial growth factor- A (VEGF-A) pathways can impact not only the endothelial cells composing the vessels, but the downstream maturation effects on pericyte and ECM components *in vitro* and *ex vivo*. To further elucidate the effects of altered VEGF signaling *in vivo*, we sought a developmental tissue that naturally exhibited a normal and high growth factor environment simultaneously to characterize the development of the BBB. One such region of the brain is the “germinal matrix” (GM), present in the third trimester of human development. The GM is located centrally, beneath the lateral ventricles and is hallmarked by high levels of growth factors,

angiogenesis, and neural stem cell proliferation. Research has indicated changes in the germinal matrix of human fetus and have been recapitulated in murine models, thus marking the GM as an ideal region to study the altered physiology of the vasculature in high growth factor and simultaneous normal brain regions. Through the careful analysis of the vessel wall, including vessel morphology, pericyte morphology, astrocyte endfeet, and extracellular matrix component, laminin, our study indicated the slower maturation progression of the microvasculature contrary to reported models. Together our results indicate that understanding how and why murine vasculature is resistant to hemorrhage, and other insults to the BBB, is critical to developing advanced treatments for use in human disease and develop more relevant models to study these effects.

INTRODUCTION

While cardiovascular disease is generally associated with atherosclerosis, vasculature plays a critical role in a wide range of pathologies that impact quality of life, including behavioral and cognitive functioning [1-3]. Cerebrovascular diseases, which include stroke, transient ischemic attacks, aneurysms, and vascular malformations, are the fifth leading cause of death in the United States [4]. Other circumstances and pathologies also contribute to brain disorders, such as the obvious traumatic brain injuries [5-7], infection [8, 9], epilepsy [10, 11], and even diabetes [12, 13]. Recent research into dementias, such as Alzheimer's [14-17]and Lewy Body [18, 19], reveal underlying malfunctions of blood vessel components. Understanding how blood vessels, and their main components, develop and mature is essential to develop better treatments for disease and improve quality of life.

Vascular development occurs in several stages. The first stage is the *de novo* formation of vessels from the coalescence of blood islets, called vasculogenesis [20-22]. These primordial vessels are then fine-tuned through remodeling of the vasculature by new vessel growth, angiogenesis, and the regression of unnecessary vessels [22, 23]. Finally, this primitive vessel network must mature through the recruitment of mural cells, vascular smooth muscle cells and pericytes, as well as the deposition of extracellular matrix (ECM) proteins to stabilize into a healthy vascular system [24-26]. Blood vessels of the brain are specialized to maintain homeostasis and controlled transport in the brain[14]. This semipermeable barrier is possible through the unique composition of the neurovascular unit. The neurovascular unit of endothelial cells that comprise blood vessel walls, astrocytic end-feet, and pericytes ensheathed in extracellular matrix, allows for the increase in tight junctions between endothelial cells and higher selectivity into the brain [14, 27, 28]. Together, the neurovascular unit evolves into the blood brain barrier, responsible for the regulation of homeostasis in the brain.

Within the blood brain barrier (BBB), the stages of vascular development must be carefully controlled by highly specific developmental programs with spatial-temporal cues [14, 29, 30]. When these cues become altered, effects upon the developing vessels can be observed at all subsequent stages and downstream impacts on tissue throughout the life cycle (i.e. hyperplasia vessels resulting in leaky vasculature and potential hemorrhage [30-32]). Previously, our research has shown that alterations in the vascular endothelial growth factor- A (VEGF-A) pathways can impact not only the endothelial cells composing the vessels, but the downstream maturation effects on

pericyte and ECM components *in vitro* and *ex vivo* [33]. Briefly, we disrupted VEGF signaling by inducing gain-of-function scenarios in sprouting angiogenesis and found pericyte coverage and migration, are compromised during VEGF-A perturbations, as well as significant transcriptional changes in endothelial cells and pericytes signaling pathways. To further clarify the effects of altered VEGF signaling *in vivo*, we sought a developmental tissue that naturally exhibited a normal and high growth factor environment simultaneously to characterize the development of the BBB.

During the third trimester of human pregnancies, there is an area of the brain that exhibits a high growth factor region undergoing rapid development [34, 35]. This region, called the germinal matrix (GM), lies centrally at the head of the caudate nucleus and underlies the ependymal lining of the lateral ventricles[36, 37]. The GM is a richly-vascularized region responsible for producing large numbers of glial and neuronal precursors during development. The GM remains relatively active through 32–34 weeks of gestation, but almost completely involutes by term [38, 39]. Levels of VEGF and angiopoietin-2, which induce endothelial proliferation and angiogenesis, are elevated in GM region [31, 34]. Due to the increased angiogenesis in this region, other aspects of the blood-brain barrier are altered in a way to increase the fragility of the vasculature, such as decreases in pericytes and glial fibrillary active protein (GFAP) in astrocyte endfeet[40, 41]. Studies have indicated changes in the germinal matrix of human fetus and have been recapitulated in several animal models[31, 42-44], thus the GM is ideal to study the altered physiology of the vasculature in high growth factor and simultaneous normal brain regions.

In the present study, we have characterized multiple aspects of the BBB in

normal murine brain subcortical region and the more active, germinal matrix vasculature. Analysis of these regions included verification of active proliferation and angiogenesis, as well as morphology of vessels, pericytes, astrocyte endfeet, and laminin, the extracellular matrix protein that is deposited first and potentially a marker of an immature vessel state. Murine brains of various ages were used to characterize the changes in maturation to these brain regions over time using postnatal days 1, 7 and 21 (P1, P7, and P21) pups. Through the careful analysis of the vessel wall, we hope to further understand the characteristics of developmental programs of the vasculature and potentially, how they can be manipulated to treat disease states and develop more relevant models to study these effects.

METHODS

Mice

All animal experiments were conducted with review and approval from the Virginia Tech Institutional Animal Care and Use Committee (IACUC). All protocols are reviewed and approved by the IACUC Board and Virginia Tech Veterinary Staff. The Virginia Tech NIH/PHS Animal Welfare Assurance Number is A-32081-01 (Expires: 7/31/2021).

Double reporter males expressing the DsRed fluorescent protein under control of the Ng2 promoter (i.e. Ng2-DsRed mice) [Tg(Cspg4-DsRed.T1)1Akik/J, JAX # 00824, The Jackson Laboratory, Bar Harbor, ME] and the green fluorescent protein (eGFP) under control of the Flk-1 (VEGF Receptor 2) promotor (ie Flk-1-eGFP) [*Kdr*$^{tm2.1Jrt}$/J, JAX #017006, The Jackson Laboratory] were bred with C57BL/6 females. Wild-type and fluorescent reporter pups (FlkeGFP, NG2dsRed, and double reporter) were euthanized

at P1, P7, and P21 by asphyxiation to isoflurane (NDC 13985-030-60, MWI Veterinary Supply Co) and thoracotomy. Cuts were made to the liver to improve cardiac perfusion with 4% paraformaldehyde (15713, Electron Microscopy Sciences) in Dubeco's phosphate buffer solution (PBS).

Following cardiac perfusion, the calvarium was exposed by sharp dissection and incised along the sagittal and lambdoid sutures using angled scissors. The resulting four cranial flaps were reflected away from the brain using forceps. Brains were severed from the spinal cord and cranial nerves using a spatula. Isolated brains were removed and fixed in 4% paraformaldehyde for 24 hours. Brains were then removed and stored in PBS.

Prior to sectioning, the olfactory bulbs and cerebellum were removed from the cerebrum using a single-edged razor blade (Garvey, 40475). Brains were then affixed caudally by superglue (Loctite, 1364076) to the vibratome dish with their ventral surface supported by a block of 4% agarose. They were then submerged in PBS and sectioned into 100 µm slices using half a double-edged razor blade (Electron Microscopy Sciences, 72000) in a vibratome (1000-Plus, Pelco 102, Ted Pella Inc.). Slices were transferred to a 24-well plate and then stored in PBS at 4 °C until processing for immunohistochemistry.

Immunostaining

Brain sections were blocked for 1 hour at room temperature in PBS and 0.1% Triton 100x (PBS-T) with 1.5% Normal Donkey Serum (Jackson ImmunoResearch, 017-000-121). Slices were then incubated at 4 °C overnight in 1.5% Normal Donkey Serum in

PBS-T with rat anti-PDGFR-β antibody (Affymetrix, 14-1402, 1:500), goat anti-CD31 antibody (R&D Systems, AF3628,1:500), rabbit anti-GFAP (Millipore Sigma, AB5804, 1:500), rabbit anti-laminin (Sigma, L9393, 1:200), and AlexaFluor 647-conjugated rabbit anti-phospho-histone H3 (PH3 Ser10, Cell Signaling, 9716, 1:200) on shaker. After incubation with primary antibodies, the slices were washed four times for 15 minutes at room temperature in PBS-T on shaker.

Brain slices were then incubated either 4 hours at room temperature or overnight at 4 °C in 1.5% Normal Donkey Serum in PBS-T with donkey anti-rat DyLight 550 (ThermoFisher, SA5-10029, 1:1000), donkey anti-goat AlexaFluor 488 (Jackson ImmunoResearch, 705-545-147, 1:500), donkey anti-rabbit AlexaFluor 647 (Jackson ImmunoResearch, 711-605-152, 1:1000), and 4',6-Diamidino-2-phenylindole (DAPI, Sigma, D9542, 1:1000). After incubation with secondary antibodies, the slices were washed four times for 15 minutes at room temperature in PBS-T, and then washed again 15 minutes at room temperature in PBS after final incubations of staining combinations.

Stained brain slices were mounted in 50% glycerol in PBS, a coverslip applied (22 mm x 22 mm – 1.5 thickness, ThermoFisher, 12-541-B), and sealed with clear nail polish (Electron Microscopy Sciences, 72180).

Microscopy

Images of stained brain sections were acquired with a Zeiss LSM 880 confocal microscope using a 20x objective and Zen Black software. Germinal matrix regions were identified using DAPI density in subventricular zones of brain hemispheres.

Subcortical regions were identified being above ventricles and included cortex and subcortical while matter. Images were collected in 2x2 tile scans with 10% overlap in 50-100 z-axis sections as determined by optimal z-axis distance. Using Zen's image processing capability, the original tile scans were stitched together. Crops of GM region of interest were outlined and saved as new image files for analysis.

Image Analysis

The germinal matrix region lies below the lateral ventricles (subventricular) and at the head or superior to the caudate nucleus. Our samples were cropped into the subventricular or the periventricular region we believed to be physiologically analogous to the GM.

Several methods were used to quantify vessel morphology. Using ImageJ/FIJI [45], vessel channel was separated and compressed to maximum intensity projections (MIPs). Images were converted to 8-bit TIFFs for quantification of vessel length and area, branch points, and lacunarity using AngioTool [46]. Outputs included average and total vessel lengths, number of endpoints, and mean lacunarity. Additional measures of total vessel area were divided by explant area to derive vessel density; and junction density was defined as the number of branch points per mm of total vessel length. Additional analysis using Image J Cell Counter to quantify angiogenic sprouts by marking the number of tip cells. The number of sprouts per vessel area was quantified.

Pericyte morphology was quantified using a MATLAB program, InSite (J.Darden and H. Patolia). Images were prepared for analysis by pseudocoloring pericyte or other targets of interest in red and vessels pseudocolored in green, then exported as 16-bit

TIFFs with both colors present in each z-slice. Once saved, images were loaded into the MATLAB program by folder selection for analysis. Briefly, red pericyte signal overlapping with green vessel signal was analyzed in all three dimensions for matches. Voxel by voxel analysis resulted in red channel over green channel percent colocalization, as well as percent proximity from dilated red signal over green signal. In this study, a dilation factor pf 1 was used for all proximity calculations. Pericyte distribution was analyzed using Image J Cell Counter for number of pericytes localized to specific vessel types. MIPs of images were used to mark pericytes in the following locales; vessel branch points, vessel sprouts with tip cells, vessel stalks, and vessels larger than capillary size (10μm).

Astrocyte end-feet and laminin coverage of the vasculature was quantified using MATLAB program with images prepared with red pseudocolor for astrocyte or laminin and green pseudocolored vasculature. Additionally, the metabolic activity of each image was quantified by counts of PH3 + cells in MIPs using Image J Cell Counter.

Statistics

Statistical analysis was conducted using one way ANOVA in GraphPad Prism software. Significance was determined as ≥ 0.05 with 95% confidence intervals.

RESULTS

The germinal matrix is a temporary, developmental region of the brain that involutes to a normal state by term in human fetuses [39]. Characterization of the BBB has been previously reported in other studies of germinal matrix hemorrhage or intraventricular

hemorrhage in premature neonates, which were taken into consideration for the validation of the germinal matrix region in the murine brain. Mouse pups ages P1, P7, and P21 were used to characterize and highlight changes in the germinal matrix and subcortical region vasculature over time. By confocal imaging, we were able to capture morphological changes in both regions in numerous biological replicates of each postnatal age (Figure 1). To characterize these regions, we analyzed multiple aspects of the vessel wall including; vessel morphology, angiogenesis activity, pericyte coverage and distribution, astrocyte endfeet-GFAP coverage, and a primary component of the ECM, laminin. To further verify the location of the germinal matrix in the murine brain tissue, analysis of metabolic activity via cell proliferation and observation of dense cellularity via DAPI were used as indicators of this actively robust zone (Figure 1).

The periventricular zone, found underneath the lateral ventricles, exhibited dense regions of DAPI next to the less dense region of the ventricle itself (Figure 1). This was utilized as a marker for the germinal matrix, along with analysis of metabolic activity. Phosphohistone-3 was used to visualize cells undergoing mitosis in both periventricular and subcortical brain regions. Analysis revealed significantly increased proliferation per area, nearly 3-fold, in the periventricular region compared to subcortical measures at earlier timepoints (P1 and P7) (Figure 1). Proliferation significantly decreased over time in both brain regions from P1 to P21, with periventricular regions maintain higher levels of proliferation than subcortical at all timepoints. This finding suggests a zone of high cell turnover congruent with observations of actively remodeling vasculature or stem cell niche, which further suggests that the periventricular zone is analogous to a germinal matrix region found in human and animal studies [35, 36, 38, 39].

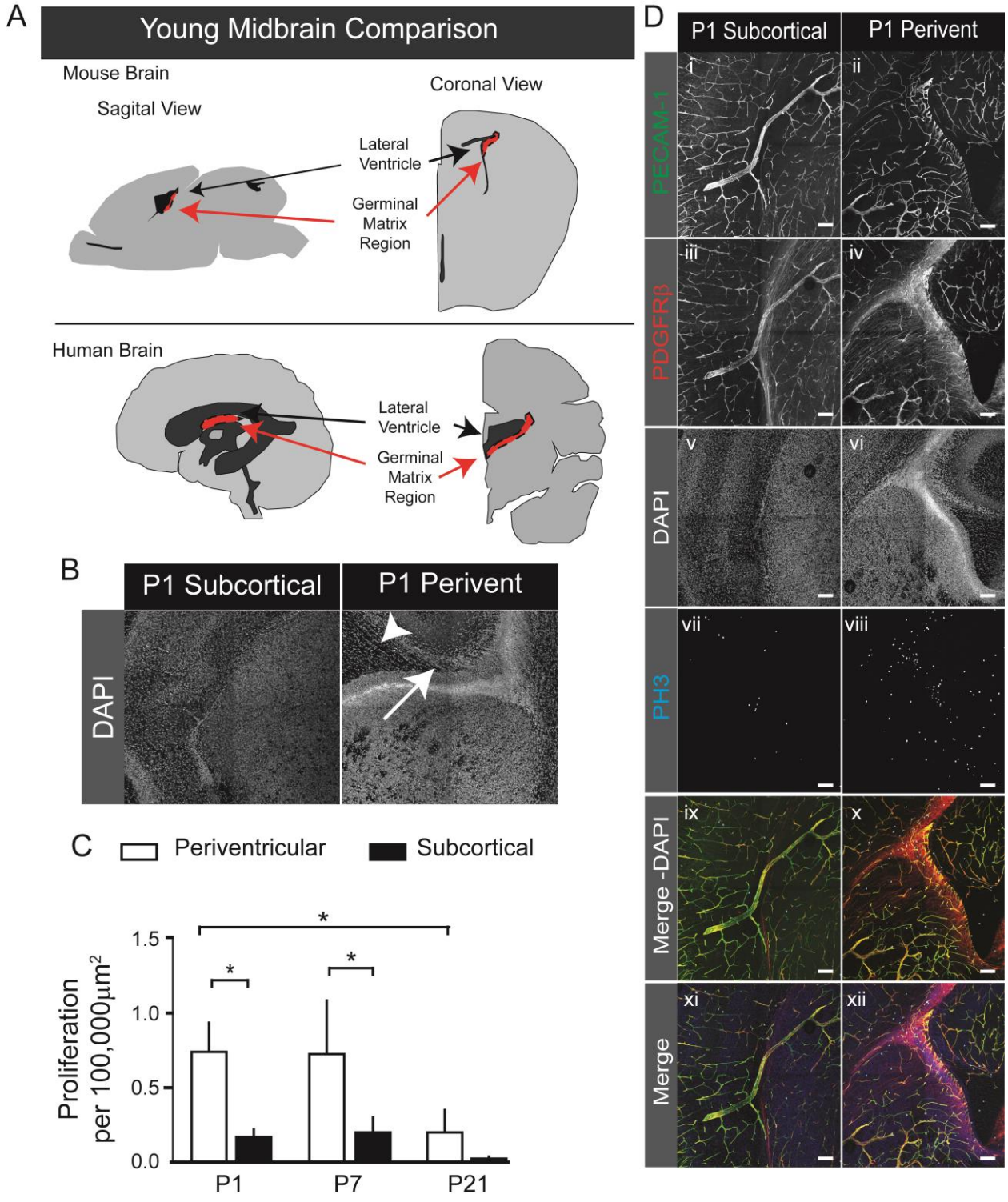
A
Young Midbrain Comparison
Mouse Brain
Sagital View
Coronal View
Lateral Ventricle
Germinal Matrix Region
Human Brain
Lateral Ventricle
Germinal Matrix Region
B
P1 Subcortical
P1 Perivent
DAPI
C
Periventricular
Subcortical
Proliferation per 100,000µm²
1.5
1.0
0.5
0.0
P1
P7
P21
D
P1 Subcortical
P1 Perivent
PECAM-1
PDGFRβ
DAPI
PH3
Merge -DAPI
Merge
i
ii
iii
iv
v
vi
vii
viii
ix
x
xi
xii

Figure 1: Validation of periventricular region as analogous to germinal matrix. **A** Schematic of murine and human midbrain with lateral ventricles (black region) and reported germinal matrix regions highlighted by red region. **B** Representative images of nuclear staining with DAPI illustrating differences in subcortical and periventricular structure. Lateral ventricle represented by arrowhead and dense region of nuclei highlighting germinal matrix region (arrow). **C** Average percentages of proliferation number per vessel area at increasing timepoints in brain regions Values are averages + Standard Deviation *P≤0.05 **D** Representative images of vessels morphology (PECAM-1), pericytes (PDGFRβ) and proliferation (PH3) subcortical and periventricular regions. Scale bars, 100μm.

Vessels

A hallmark of the germinal matrix is the increased vascular remodeling due to presence of growth factors, such as VEGF-A [31, 35]. Active remodeling includes the process of sprouting angiogenesis and the regression of unnecessary vessels to form a more uniform meshwork formation of vessels in the capillary beds [24, 47]. In this way, segments of longer vessel lengths are remodeled into smaller patches of interconnected vessels. To further support the notion that the periventricular region is analogous to the germinal matrix, angiogenesis activity was analyzed by observation of the number of sprouting events per vessel area. Sprouting events are defined with the presence of a "tip cell" with filopodia, and marked with Image J software (Figure 2). The number of events were divided over the vessel area to normalize measures between brain regions. The number of sprouting events in the periventricular region were trending higher at P1, but evened out (decreased) to subcortical measures at P7, and P21. There was a significant decrease from P1 to P21, indicative of a longer period of development/maturation than previously believed. This suggests a high level of angiogenesis at the beginning developmental stage of the germinal matrix region that resolves with time and further development, consistent with findings in multiple studies

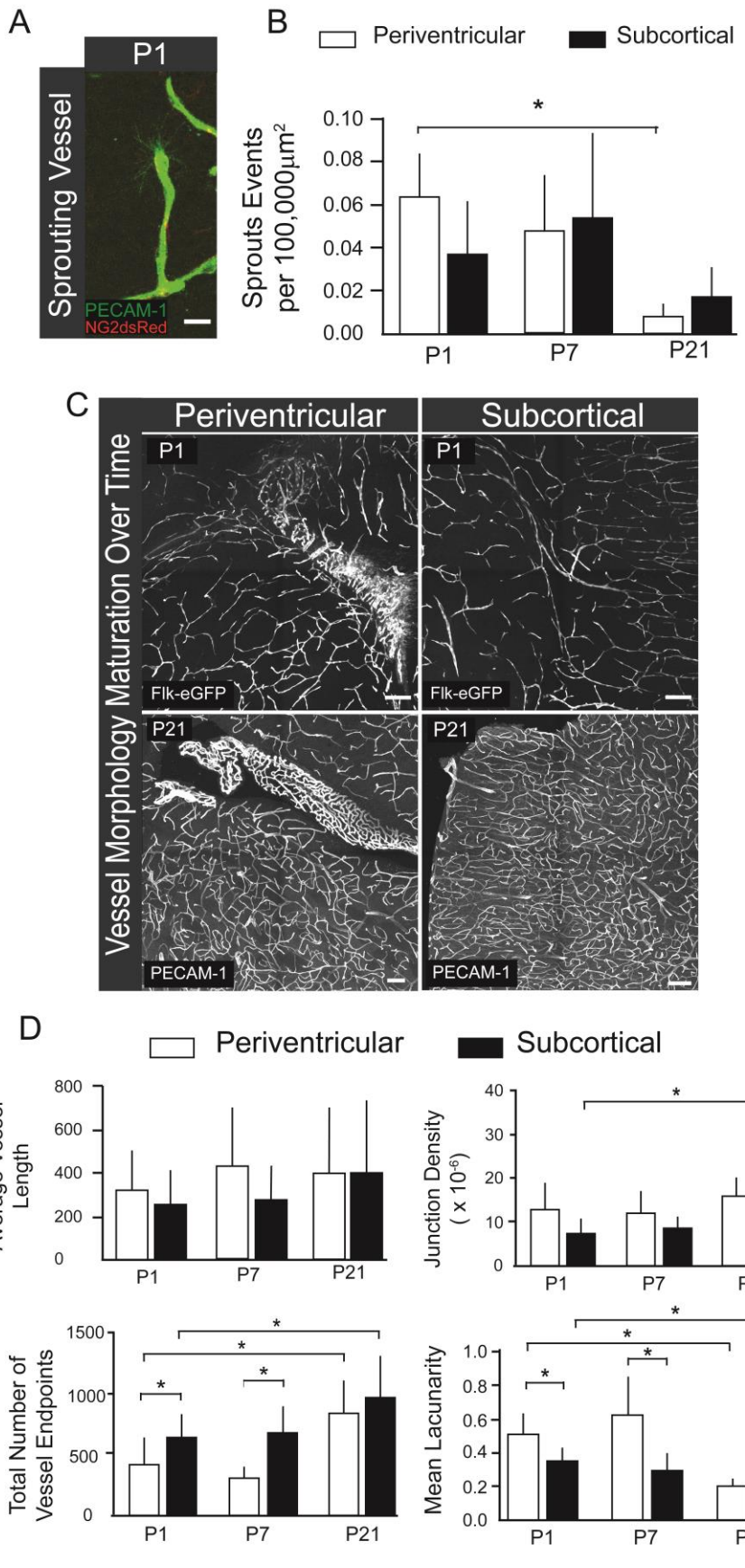
A
P1
Sprouting Vessel
PECAM-1
NG2dsRed
B
Periventricular
Subcortical
Sprouts Events per 100,000μm²
0.10
0.08
0.06
0.04
0.02
0.00
*
P1
P7
P21
C
Periventricular
Subcortical
Vessel Morphology Maturation Over Time
P1
P1
Flk-eGFP
Flk-eGFP
P21
P21
PECAM-1
PECAM-1
D
Periventricular
Subcortical
Average Vessel Length
800
600
400
200
0
P1
P7
P21
Junction Density (x 10⁻⁶)
40
30
20
10
0
*
P1
P7
P21
Total Number of Vessel Endpoints
1500
1000
500
0
*
*
*
*
P1
P7
P21
Mean Lacunarity
1.0
0.8
0.6
0.4
0.2
0.0
*
*
*
*
P1
P7
P21

Figure 2: Analysis of vessel morphology maturation over time. **A** Representative image of a sprouting vessel with tip cells and filopodial extensions. Scale bar, 10µm. **B** Average percentage of sprouting events per vessel area. Values are averages + Standard Deviation *P≤0.05 **C** Representative images of vessels maturation in normal (subcortical) and high growth factor (periventricular) regions at beginning and end timepoints of analysis. Scale bars, 100µm. **D** Average percentages of measures of vessel morphology, including patterning. Values are averages + Standard Deviation *P≤0.05

[39, 40]. The presence of sprouts is not the only indicator of vessel remodeling. Analysis of the capillary beds themselves with the brain regions was necessary to capture changes in vascular development.

Vessel morphology was analyzed to determine the size, density, and length of the capillary beds, as well as patterning of vessels as an indicator of maturity (Figure 2). AngioTool, a published tool of vessel analysis, allowed the computation of the number of branch points, end point, vessels lengths, and patterning of the vessel network in collected images of subcortical and periventricular regions. Analysis of vessel lengths and density showed no significant difference in vessel lengths at any timepoint between regions, remaining consistent across time and region. However, further analysis of the vessel morphology did reveal differences in vessel patterning between brain regions. Junction density remains higher in periventricular than subcortical regions across time. However, subcortical branching does significantly increase from P1 to P21. Another measure of vessel network patterning includes the total number of endpoints (open ended segments) present within the network. Endpoints within the capillary bed would be representative of any segments that are not between two branch points. There were significantly less endpoints in periventricular than subcortical regions at P1 and P7. Numbers were similar between regions at P21, and increased within both regions from

P1 to P21. Together this suggests that in the periventricular region, which we believe analogous to the germinal matrix, vessels have more branches, therefore less open segments, than the subcortical brain region, perhaps eluding to the high degree or rate of remodeling present in that region. The alterations to branching points and open segments from P1 to P21, indicated that these vessel networks can remodel and do at a slower rate or later point in development.

The final vessel morphology characterization was of vessel lacunarity, or the "holes" in the capillary network. Higher measures of lacunarity were representative of more space between the vessels, leaving a more heterogenic pattern. Lower measures would represent more uniformity of the network pattern. At earlier timepoints, the periventricular region had significantly higher measures of lacunarity than subcortical regions at P1 and P7. With maturation, from P1 to P21, both regions showed a significant decrease, becoming more consistently patterned over time (Figure 2). This suggests a more uniform or consistent vessel pattern is a mark of maturity and although the lacunarity decreases with age in the periventricular region, it maintains a more immature vessel pattern than control regions.

Pericytes

In addition to the vessels themselves, other aspects of the BBB contribute to functioning of healthy capillaries [14, 32]. Traditional pericytes have elongated processes that extend along the abluminal side of capillaries and make cell-cell contact with endothelial cells through peg and socket connections. It is suggested that gap junctions and adheren junctions are crucial components of the peg and socket contact to facilitate

direct cross-talk between endothelial cells and pericytes [48-51].These support cell aid in communication, ECM deposition, and even flow regulation [52, 53]. Pericyte are especially critical within the brain as recent research has shown that pericytes are the first to construct the blood brain barrier, previously attributed to astrocyte endfeet [54, 55]. Sprouting vessels recruit pericytes to stabilize the novel vessel segment and contribute to the maturation of the vessel network [56, 57]. Analysis of the pericyte colocalization and proximity, or close association with, vessels revealed an interesting trend in the periventricular region. Although at P1 there appears to be higher colocalization in both regions, there is increased measures of pericytes in the periventricular region. This is not unexpected as a region of high growth. At P7, however, the significantly higher number of pericytes in the periventricular region is contrary to reports on germinal matrix pericyte numbers in other studies [35, 40]. Looking at a further timepoint of development at P21, the pericyte association has decreased and is less than levels in the subcortical region. Additionally, both regions show decreased pericyte colocalization at P21 than at P1, indicative of pericyte recruitment and investment into the vessel network over time. Taken together, this perhaps suggests that although the germinal matrix is considered a developmental region that is highly variable and normalizes by term, the development may not be as stable or mature as previously believed at that timepoint and in fact needs more time to mature fully. Within the brain, maturity of the blood brain barrier should include tightly adhered endothelial cells, pericyte coverage over vessels, astrocyte endfeet contacting the vessels, and encasement within the extracellular matrix to regulate all matter flowing into and out of the immune-privileged brain.

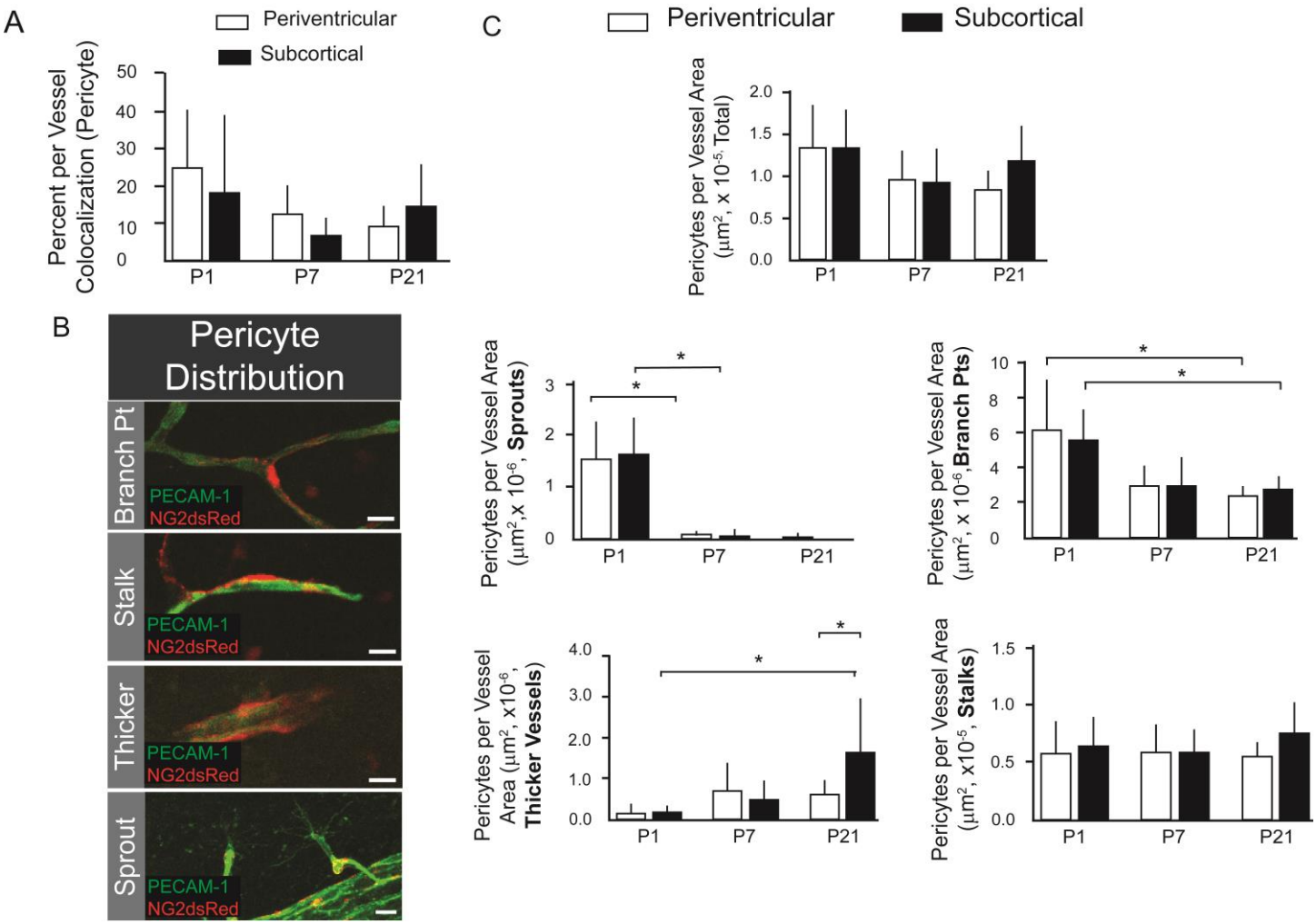

Figure 3: Analysis of pericyte morphology in normal and high growth brain regions. **A** Average percentage of pericyte colocalization with blood vessels with maturation over time. Values are averages + Standard Deviation **B** Representative images of specific locations of pericytes (red) on blood vessels (green) Scale bars, 10μm. **C** Average of pericyte distribution within the vasculature per vessel area. Values are averages + Standard Deviation *P≤0.05

Pericyte morphology and the degree of their density on vessels differs in specific tissues [52]. Traditionally pericytes are found along branch points and stalks, or quiescent vessels segments, within the microvascular network (Figure 3). Analysis of the distribution of pericytes within the capillary beds revealed a similar pattern of pericyte investment in the vessel wall. Comparing the total number of pericytes per vessel area revealed that at P1, P7, and P21, there were no significant differences in overall numbers (Figure 3). In regards to overall pattern of distribution, findings supported significantly higher pericyte recruitment activity at P1 along sprouts with tips cells, than the following timepoints within both brain regions. correlating with the increased sprouting of vessels at P1. Additionally, with increased timepoints from P1 to P21, there is significant decrease in the percentage of pericyte on branch points within both brain regions and an increase in the percentage of pericytes on thicker vessels (greater than 10um). This could indicate the remodeling of vessels into thicker, higher order vasculature or an increase of branch points (as suggested from Figure 2) without pericyte coverage. In summary, the vasculature recruits pericytes and pericytes distribute along the vessel at the same rate and in the same pattern within both brain regions. This suggests that in a high growth factor environment, pericyte migration is not impacted, however final pericyte number may change over time.

Other Components of BBB

Another component of the BBB that was characterized was the association of astrocyte endfeet. Astrocytes endfeet are crucial for the ion/ water transport and maintaining the BBB in part by inducing expression of tight junctions in endothelial cells [14, 58, 59].

Astrocytes were marked by the presence of GFAP+ structures (Figure 4). GFAP provides shape and structure to the endfeet [60, 61], and decreases may reveal a structural weakening of the BBB. In our analysis, we found the presence of GFAP+ cells colocalized and in proximity to vessels to be highly variable across both brain regions, with seemingly little to no correlation with capillary vessels of interest. At postnatal days 1 and 7, it appears that there is more GFAP+ cells in the subcortical region compared to the periventricular region. At P21, both regions have a higher presence of GFAP + astrocytes associated with vessels, however there is no significance across regions or time due to the high variability of this cell type.

The final aspect of the blood brain barrier that was characterized in these brain regions was the extracellular matrix. The ECM primary function within multicellular organisms is structural engineering [62]. The blood brain barrier is composed of four main molecules; collagen IV, laminin, nindogens, and heparan sulfate proteoglycans (HSPGs) [62]. Laminin is believed to be the primary foundation of sheet structure and is the main component seen in early development [63]. Therefore, we focused our efforts on analyzing the laminin molecules of various isoforms (Figure 5). By using the computational tool developed in our lab, analysis revealed a trend of higher percent of laminin colocalized, and in proximity, to the capillary vessels of the periventricular region. This trend maintained consistently over time for that region, suggesting that the periventricular region is composed of a more immature basement membrane than other regions of the brain, and is not just a hallmark of a high growth rate region. This finding could suggest that the basement membrane does not mature as quickly in this region even after a long period of developmental timeframe. It could also suggest that the

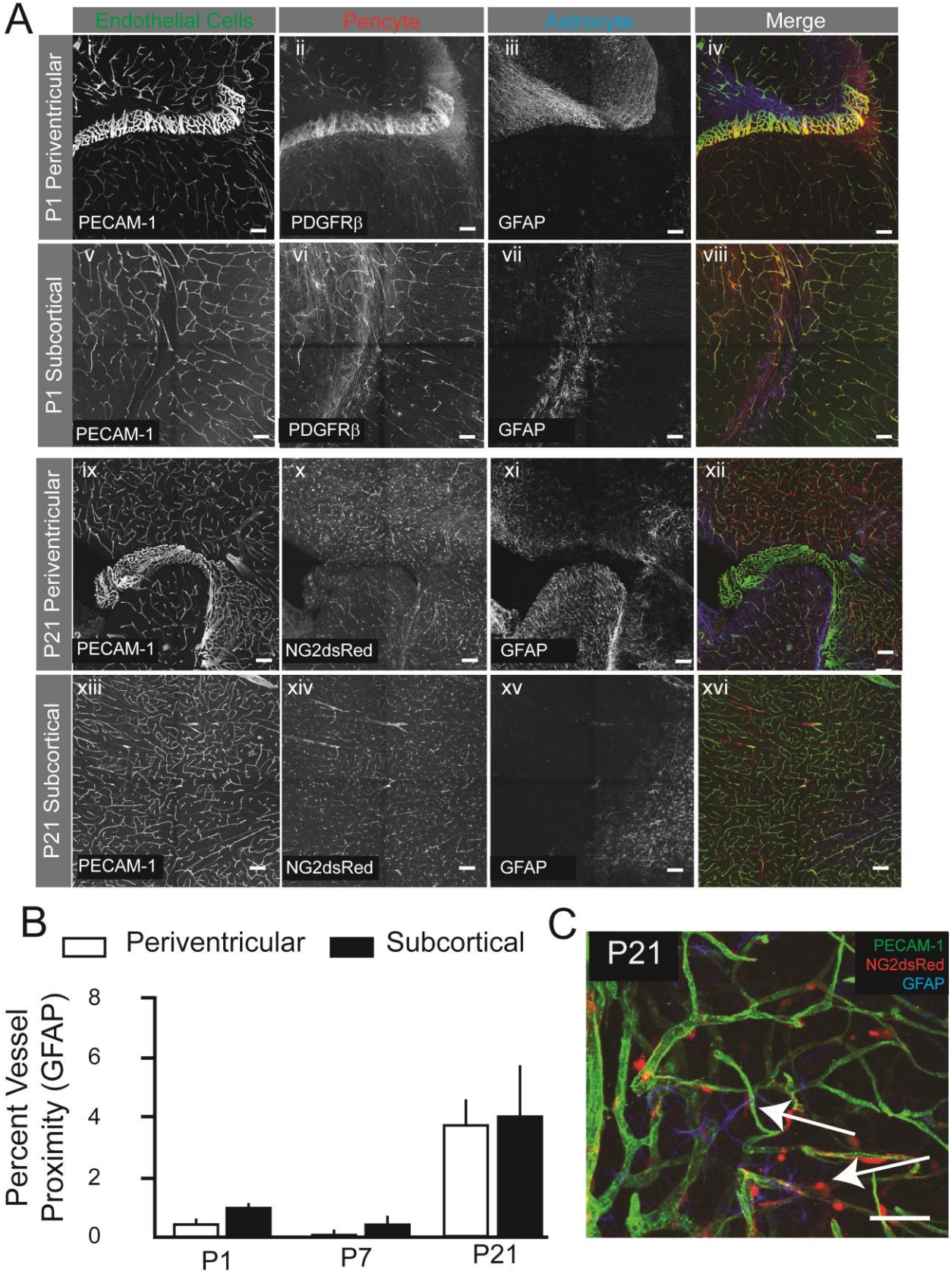
A
Endothelial Cells
Pericyte
Astrocyte
Merge
P1 Periventricular
P1 Subcortical
P21 Periventricular
P21 Subcortical
PECAM-1
PDGFRβ
GFAP
NG2dsRed
B
Periventricular
Subcortical
Percent Vessel Proximity (GFAP)
0
2
4
6
8
P1
P7
P21
C
P21
PECAM-1
NG2dsRed
GFAP

Figure 4: Astrocyte endfeet coverage in microcirculation. **A** Representative images of astrocyte endfeet association with vessels at postnatal days 1 and 21. Vessels are labeled with PECAM-1 (green), pericytes with PDGFRβ or NG2dsRed (red) genetic fluorescence, and astrocytic endfeet with GFAP (blue). Scale bars, 100μm. **B** Average percentages of GFAP+ astrocyte proximity with vessels at multiple timepoints. Values are averages + Standard Deviation *P≤0.05 **C** Representative image of close association (proximity) of astrocytic endfeet (blue) with the BBB, including vessels (green) and pericytes (red). Scale bar, 50μm.

periventricular region is significantly different and will remain so instead of experiencing an alteration in basement membrane proteins that are considered more mature and stable, potentially, collagens.

DISCUSSION

Understanding the development of blood vessel component is key to generating accurate models for studying disease. In high growth factor environments, such as high VEGF-A, endothelial cells present with a skewed morphology of hyperplasia and increased angiogenic sprouts in *in vitro* and *in vivo* models [33, 64-66]. In this study, the data show little differences in vessel morphology between subcortical and periventricular regions at the selected timepoints. P1 sprouting is similar between regions and decreases in both by P7. Vessel length, density, and area remain similar between regions and across timepoints, indicating a lack of dysmorphology contrary to what has been reported. Pericyte coverage of microvessels is also altered from reports of periventricular regions. Previous research indicated a lack of pericytes in this germinal matrix regions of the brain in animal and human tissues [31, 39, 40]. The data show a variability of pericyte colocalization of vessel at different timepoints, even higher in this region at P7 before decreasing below cortical regions at a mature age. Pericyte

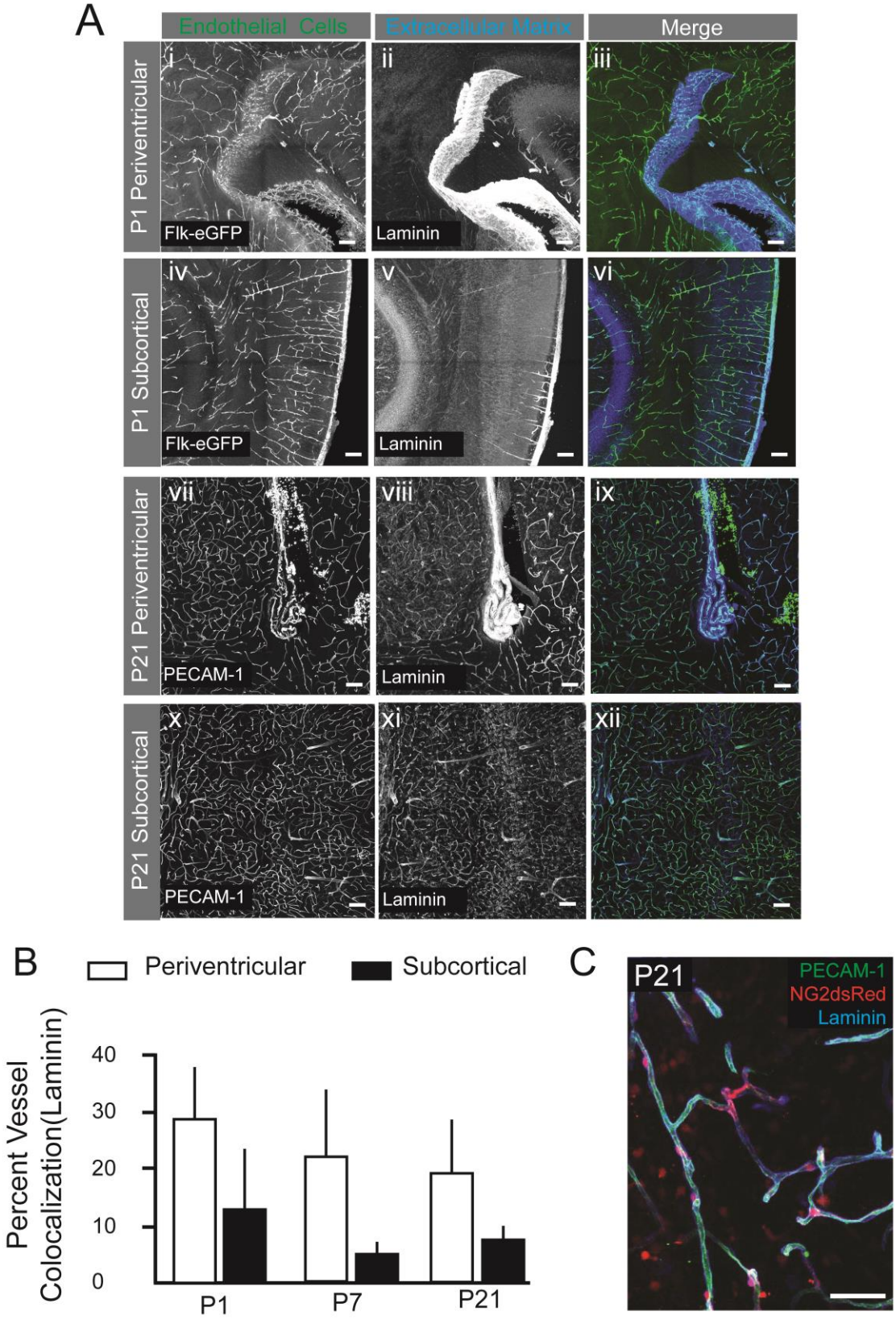
A
Endothelial Cells
Extracellular Matrix
Merge
P1 Periventricular
P1 Subcortical
P21 Periventricular
P21 Subcortical
Flk-eGFP
Laminin
PECAM-1
B
Periventricular
Subcortical
Percent Vessel Colocalization(Laminin)
40
30
20
10
0
P1
P7
P21
C
P21
PECAM-1
NG2dsRed
Laminin

Figure 5: Extracellular matrix association of BBB in microcirculation. **A** Representative images of laminin association with vessels at postnatal days 1 and 21. Vessels are labeled with Pecam-1 (green), and ECM with Laminin (blue). Scale bars, 100µm. **B** Average percentages of laminin colocalization with vessels at multiple timepoints. Values are averages + Standard Deviation *P≤0.05 **C** Representative image of close association (colocalization) of laminin (blue) with the BBB, including vessels (green) and pericytes (red). Scale bar, 50µm.

distribution within the microvasculature remained similar between both regions across timepoints, contrary to expectations and previous research. More research is needed to determine at why there is a lack of altered morphology and what mechanisms contribute to the normalization reported here.

The other component of the BBB studied was the maturation of the ECM via laminin. In normal environments of the subcortical region, laminin was not unexpectedly abundant, even with a trend of increased level in a high growth factor environment of the periventricular region as laminin remains a base component of the ECM. What is interesting is that the trend of increased laminin remains across timepoints in the periventricular region, suggesting a fundamental difference in the composition of BBB in that region compared to subcortical even when other components such as pericyte and vessel morphology largely unchanged between regions[25]. This suggests that an outside component contributes to laminin in a way that is altered in higher growth factor environments. Potentially further research could include genetic loss and gain of functions for VEGF or Angpt signaling to analyze what pathways may be altered downstream and how the effects of intact signaling mitigates any abnormal response.

In our study, data show a different timeframe for development than previously believed for brain blood vessels. Research indicates P0-P3 pups is analogous to premature human brains, and development of the vasculature should be complete by

P7 [67]. The data show that even at P7, vascular maturation is not complete. Perhaps this is not necessarily surprising because retina vessels undergo vascular remodeling at P7 and have been used for studies of vascular development [68, 69]. This indicates a need for models that investigate pathologies at younger timepoints to incorporate variability in vascular integrity for a longer timeframe, such as for germinal matrix hemorrhage or developmental vascular malformations.

Together our results indicate murine vasculature develops and matures in an unexpected timeframe. It is more interesting to note that even with a slower timeframe of maturation, vessel structure, and potentially integrity, of the BBB remains largely unchanged in normal and high growth factor environments. Research into why this is the case could reveal potential molecular cues for increasing stability in human vasculature. Additionally, understanding how and why murine vasculature is resistant to hemorrhage and other insults to the BBB is critical to developing advanced treatments for use in human disease.

REFERENCES

1. Reitz, C., J.A. Luchsinger, and R. Mayeux, *Vascular disease and cognitive impairment.* Expert Rev Neurother, 2008. **8**(8): p. 1171-4.
2. Owolabi, M., et al., *Behavioural and Cognitive Effects of Cerebrovascular Diseases.* Behav Neurol, 2018. **2018**: p. 7516032.
3. Vohr, B., et al., *Early-onset intraventricular hemorrhage in preterm neonates: incidence of neurodevelopmental handicap.* Semin Perinatol, 1999. **23**(3): p. 212-7.
4. Jiaquan Xu, S.L.M., Kenneth D. Kochanek, Brigham Bastian, Elizabeth Arias, *Deaths: Final Data for 2016*, in *National Vital Statistics Report*. 2018, National Center for Health Statistics: Hyattsville, MD.
5. DeWitt, D.S. and D.S. Prough, *Traumatic cerebral vascular injury: the effects of concussive brain injury on the cerebral vasculature.* J Neurotrauma, 2003. **20**(9): p. 795-825.

6. Dore-Duffy, P., et al., *Pericyte migration from the vascular wall in response to traumatic brain injury.* Microvasc Res, 2000. **60**(1): p. 55-69.
7. Monson, K.L., M.I. Converse, and G.T. Manley, *Cerebral blood vessel damage in traumatic brain injury.* Clin Biomech (Bristol, Avon), 2018.
8. Chaudhuri, J.D., *Blood brain barrier and infection.* Med Sci Monit, 2000. **6**(6): p. 1213-22.
9. Puntener, U., et al., *Long-term impact of systemic bacterial infection on the cerebral vasculature and microglia.* J Neuroinflammation, 2012. **9**: p. 146.
10. Croll, S.D., J.H. Goodman, and H.E. Scharfman, *Vascular endothelial growth factor (VEGF) in seizures: a double-edged sword.* Adv Exp Med Biol, 2004. **548**: p. 57-68.
11. Marchi, N. and M. Lerner-Natoli, *Cerebrovascular remodeling and epilepsy.* Neuroscientist, 2013. **19**(3): p. 304-12.
12. Ergul, A., et al., *Cerebrovascular complications of diabetes: focus on stroke.* Endocr Metab Immune Disord Drug Targets, 2012. **12**(2): p. 148-58.
13. Xu, R.S., *Pathogenesis of diabetic cerebral vascular disease complication.* World J Diabetes, 2015. **6**(1): p. 54-66.
14. Ballabh, P., A. Braun, and M. Nedergaard, *The blood-brain barrier: an overview: structure, regulation, and clinical implications.* Neurobiol Dis, 2004. **16**(1): p. 1-13.
15. Kisler, K., et al., *Pericyte degeneration leads to neurovascular uncoupling and limits oxygen supply to brain.* Nat Neurosci, 2017. **20**(3): p. 406-416.
16. Sagare, A.P., R.D. Bell, and B.V. Zlokovic, *Neurovascular dysfunction and faulty amyloid beta-peptide clearance in Alzheimer disease.* Cold Spring Harb Perspect Med, 2012. **2**(10).
17. Nelson, A.R., et al., *Neurovascular dysfunction and neurodegeneration in dementia and Alzheimer's disease.* Biochim Biophys Acta, 2016. **1862**(5): p. 887-900.
18. Hamilton, N.B., D. Attwell, and C.N. Hall, *Pericyte-mediated regulation of capillary diameter: a component of neurovascular coupling in health and disease.* Front Neuroenergetics, 2010. **2**.
19. Jellinger, K.A., *Prevalence and impact of cerebrovascular lesions in Alzheimer and lewy body diseases.* Neurodegener Dis, 2010. **7**(1-3): p. 112-5.
20. Arora, R. and V.E. Papaioannou, *The murine allantois: a model system for the study of blood vessel formation.* Blood, 2012. **120**(13): p. 2562-72.
21. Beck, L., Jr. and P.A. D'Amore, *Vascular development: cellular and molecular regulation.* FASEB J, 1997. **11**(5): p. 365-73.
22. Flamme, I., T. Frolich, and W. Risau, *Molecular mechanisms of vasculogenesis and embryonic angiogenesis.* J Cell Physiol, 1997. **173**(2): p. 206-10.
23. Poole, T.J. and J.D. Coffin, *Vasculogenesis and angiogenesis: two distinct morphogenetic mechanisms establish embryonic vascular pattern.* J Exp Zool, 1989. **251**(2): p. 224-31.
24. Jain, R.K., *Molecular regulation of vessel maturation.* Nat Med, 2003. **9**(6): p. 685-93.

25. Stratman, A.N., et al., *Pericyte recruitment during vasculogenic tube assembly stimulates endothelial basement membrane matrix formation.* Blood, 2009. **114**(24): p. 5091-101.
26. Udan, R.S., J.C. Culver, and M.E. Dickinson, *Understanding vascular development.* Wiley Interdiscip Rev Dev Biol, 2013. **2**(3): p. 327-46.
27. Armulik, A., et al., *Pericytes regulate the blood-brain barrier.* Nature, 2010. **468**(7323): p. 557-61.
28. Daneman, R., et al., *Pericytes are required for blood-brain barrier integrity during embryogenesis.* Nature, 2010. **468**(7323): p. 562-6.
29. Ballabh, P., et al., *Development of tight junction molecules in blood vessels of germinal matrix, cerebral cortex, and white matter.* Pediatr Res, 2005. **58**(4): p. 791-8.
30. Henshall, T.L., et al., *Notch3 is necessary for blood vessel integrity in the central nervous system.* Arterioscler Thromb Vasc Biol, 2015. **35**(2): p. 409-20.
31. Ballabh, P., et al., *Angiogenic inhibition reduces germinal matrix hemorrhage.* Nat Med, 2007. **13**(4): p. 477-85.
32. Sweeney, M.D., S. Ayyadurai, and B.V. Zlokovic, *Pericytes of the neurovascular unit: key functions and signaling pathways.* Nat Neurosci, 2016. **19**(6): p. 771-83.
33. Darden, J., et al., *Excess vascular endothelial growth factor-A disrupts pericyte recruitment during blood vessel formation.* Angiogenesis, 2018.
34. Yang, D., et al., *Overexpression of vascular endothelial growth factor in the germinal matrix induces neurovascular proteases and intraventricular hemorrhage.* Sci Transl Med, 2013. **5**(193): p. 193ra90.
35. Ballabh, P., *Intraventricular hemorrhage in premature infants: mechanism of disease.* Pediatr Res, 2010. **67**(1): p. 1-8.
36. Ballabh, P., A. Braun, and M. Nedergaard, *Anatomic analysis of blood vessels in germinal matrix, cerebral cortex, and white matter in developing infants.* Pediatr Res, 2004. **56**(1): p. 117-24.
37. Ment, L.R., et al., *Intraventricular hemorrhage in the preterm neonate: timing and cerebral blood flow changes.* J Pediatr, 1984. **104**(3): p. 419-25.
38. Donat, J.F., et al., *Intraventricular hemorrhages in full-term and premature infants.* Mayo Clin Proc, 1978. **53**(7): p. 437-41.
39. Whitelaw, A., *Intraventricular haemorrhage and posthaemorrhagic hydrocephalus: pathogenesis, prevention and future interventions.* Semin Neonatol, 2001. **6**(2): p. 135-46.
40. Braun, A., et al., *Paucity of pericytes in germinal matrix vasculature of premature infants.* J Neurosci, 2007. **27**(44): p. 12012-24.
41. Ballabh, P., *Pathogenesis and prevention of intraventricular hemorrhage.* Clin Perinatol, 2014. **41**(1): p. 47-67.
42. Ment, L.R., Stewart, W.B., Ardito, T.A., Huang, E., Madri, J.A., *Indomethain Promotes Germinal Matrix Microvessel Maturation in the Newborn Beagle Pup.* Stroke, 1992. **23**: p. 1132-1137.
43. Lekic, T., et al., *Rodent neonatal germinal matrix hemorrhage mimics the human brain injury, neurological consequences, and post-hemorrhagic hydrocephalus.* Exp Neurol, 2012. **236**(1): p. 69-78.

44. Chua, C.O., et al., *Effect of hyperoxic resuscitation on propensity of germinal matrix haemorrhage and cerebral injury.* Neuropathol Appl Neurobiol, 2010. **36**(5): p. 448-58.
45. Schindelin, J., et al., *Fiji: an open-source platform for biological-image analysis.* Nature Methods, 2012. **9**: p. 676.
46. Zudaire, E., et al., *A computational tool for quantitative analysis of vascular networks.* PLoS One, 2011. **6**(11): p. e27385.
47. Risau, W., *Mechanisms of angiogenesis.* Nature, 1997. **386**(6626): p. 671-4.
48. Hirschi, K.K. and P.A. D'Amore, *Pericytes in the microvasculature.* Cardiovasc Res, 1996. **32**(4): p. 687-98.
49. Li, A.F., et al., *High glucose alters connexin 43 expression and gap junction intercellular communication activity in retinal pericytes.* Invest Ophthalmol Vis Sci, 2003. **44**(12): p. 5376-82.
50. Gerhardt, H., H. Wolburg, and C. Redies, *N-cadherin mediates pericytic-endothelial interaction during brain angiogenesis in the chicken.* Dev Dyn, 2000. **218**(3): p. 472-9.
51. Cuevas, P., et al., *Pericyte endothelial gap junctions in human cerebral capillaries.* Anat Embryol (Berl), 1984. **170**(2): p. 155-9.
52. Armulik, A., A. Abramsson, and C. Betsholtz, *Endothelial/pericyte interactions.* Circ Res, 2005. **97**(6): p. 512-23.
53. Hill, R.A., et al., *Regional Blood Flow in the Normal and Ischemic Brain Is Controlled by Arteriolar Smooth Muscle Cell Contractility and Not by Capillary Pericytes.* Neuron, 2015. **87**(1): p. 95-110.
54. Bergers, G. and S. Song, *The role of pericytes in blood-vessel formation and maintenance.* Neuro Oncol, 2005. **7**(4): p. 452-64.
55. Lai, C.H. and K.H. Kuo, *The critical component to establish in vitro BBB model: Pericyte.* Brain Res Brain Res Rev, 2005. **50**(2): p. 258-65.
56. Gerhardt, H. and C. Betsholtz, *Endothelial-pericyte interactions in angiogenesis.* Cell Tissue Res, 2003. **314**(1): p. 15-23.
57. Lindblom, P., et al., *Endothelial PDGF-B retention is required for proper investment of pericytes in the microvessel wall.* Genes Dev, 2003. **17**(15): p. 1835-40.
58. Alvarez, J.I., T. Katayama, and A. Prat, *Glial influence on the blood brain barrier.* Glia, 2013. **61**(12): p. 1939-58.
59. Cabezas, R., et al., *Astrocytic modulation of blood brain barrier: perspectives on Parkinson's disease.* Front Cell Neurosci, 2014. **8**: p. 211.
60. Sofroniew, M.V. and H.V. Vinters, *Astrocytes: biology and pathology.* Acta Neuropathol, 2010. **119**(1): p. 7-35.
61. Hol, E.M. and M. Pekny, *Glial fibrillary acidic protein (GFAP) and the astrocyte intermediate filament system in diseases of the central nervous system.* Curr Opin Cell Biol, 2015. **32**: p. 121-30.
62. Bruce Alberts, A.J., Julian Lewis, Martin Raff, Keith Roberts, Peter Walter, *Molecular Biology of the Cell, 5th Edition*. 5 ed. 2007: Garland Science 5th edition. 1392.
63. Hamill, K.J., et al., *Laminin deposition in the extracellular matrix: a complex picture emerges.* J Cell Sci, 2009. **122**(Pt 24): p. 4409-17.

64. Carmeliet, P., *Angiogenesis in life, disease and medicine.* Nature, 2005. **438**(7070): p. 932-6.
65. Carmeliet, P., *Angiogenesis in health and disease.* Nat Med, 2003. **9**(6): p. 653-60.
66. Benjamin, L.E., I. Hemo, and E. Keshet, *A plasticity window for blood vessel remodelling is defined by pericyte coverage of the preformed endothelial network and is regulated by PDGF-B and VEGF.* Development, 1998. **125**(9): p. 1591-8.
67. Semple, B.D., et al., *Brain development in rodents and humans: Identifying benchmarks of maturation and vulnerability to injury across species.* Prog Neurobiol, 2013. **106-107**: p. 1-16.
68. Connolly, S.E., et al., *Characterization of vascular development in the mouse retina.* Microvasc Res, 1988. **36**(3): p. 275-90.
69. Stahl, A., et al., *The mouse retina as an angiogenesis model.* Invest Ophthalmol Vis Sci, 2010. **51**(6): p. 2813-26.

CHAPTER 5

SUMMARY

Pericytes are essential to blood vessel networks. While contributing to blood flow regulation, removal of toxic materials, and communication, their most important role is maturation of the developing vascular network. Many mechanisms underlying initial vascular development can re-emerge to enable the vasculature to adapt in response to various pathologies, injuries, and aging [1, 2]. Understanding how developmental programs “push” pericytes, and other blood vessel components, into a healthy, functional network can lead to potential therapies in a spectrum of diseases.

During and after the remodeling stage of development, pericytes are recruited into the microvasculature by multiple pathways to coordinate endothelial cell-pericyte dynamics. Transforming growth factor-β (TGFβ) signaling promotes the differentiation of pericytes, downstream of gap junction formation between pericytes and endothelial cells [3]. Reports indicate sphingosine-1-phosphate (S1P) signaling promotes the trafficking of N-cadherin in both endothelial cells and pericytes to support the formation of peg-and-socket contacts between cells [4]. The Angiopoietin (Angpt)-Tie signaling pathway has also been described as an important mediator of pericyte-endothelial cell interactions for determining vessel quiescence. Angiopoietin-2 (Angpt2) over-expression can induce pericyte migration off existing and remodeling vasculature [5], while Angpt1 promotes stable interactions of pericytes with endothelial cells [6-8]. The Angpt-Tie pathway may also intersect with heparin-binding EGF-like growth factor (HB-EGF) signaling [9] to coordinate pericyte recruitment and subsequent migration along

developing vessels. However, one of the most important signaling cascades for the recruitment, migration, and proliferation of pericytes is the PDGF-BB (PDGF-B) pathway [10-12]. PDGF-B is synthesized and released by endothelial cells, especially in endothelial tip cells, to create a migration gradient for pericyte recruitment [13, 14]. PDGF-B anchors to perlecan/HSPG-2 within the ECM to be presented to pericytes for binding PDGF Receptor-β (PDGFRβ) on their cell surface [14]. Normal maturation of the vasculature depends on these multiple pathways of paracrine signaling between endothelial cell and pericytes.

Studies examining the mechanisms for pericyte recruitment and migration focus on genetic manipulations of the pathway being investigated. In general, pathologies are not necessarily derived from mutation of these particular pathway components. Typically, a larger system is detrimentally affected, such as a high growth factor environment (i.e. increased VEGF). In this work, I focused on the impact of an altered growth factor environment on endothelial cell-pericyte interactions to further understand the effects of high VEGF on pericytes during vascular maturation.

Summary and future directions of Chapter 2: Excess Vascular Endothelial Growth Factor-A Disrupts Pericyte Recruitment during Blood Vessel Formation

Pericyte investment into new blood vessels is essential for vascular development such that mis-regulation within this phase of vessel maturation can contribute to numerous pathologies of vessel dysmorphogenesis, including arteriovenous and cerebrovascular malformations [2, 15]. It is therefore critical to clarify how angiogenic signaling

pathways combine to regulate pericyte migration and investment. Here, we disrupted vascular endothelial growth factor-A (VEGF-A) signaling in *ex vivo* and *in vitro* models of sprouting angiogenesis, and found pericyte coverage to be compromised during VEGF-A perturbations [16]. Our data show pericytes had little to no expression of VEGF receptors, suggesting VEGF-A signaling defects affect endothelial cells directly but pericyte indirectly.

In this study, we demonstrate that mis-regulated VEGF-A signaling in endothelial cells indirectly compromises pericyte distribution and coverage along developing embryonic vessels by limiting pericyte migration. Pericyte coverage of developing vessels require precision spatio-temporal coordination of endothelial VEGF-A signaling, as this pathway provides important downstream regulation of pericyte distribution via PDGF-B-PDGFRβ activity. Our data show significantly increased *pdgfb* in endothelial cells and decreased *pdgfrβ* in pericytes by gene expression analysis. The decreased signaling is validated by protein analysis of PDGFRβ, showing a 1/3 decrease from wild-type controls versus *flt1*$^{-/-}$ pericyte populations. Interestingly, the data also indicated the presence of an isoform that was previously unknown in these ESC-derived populations. Sequence analysis suggested that this PDGFRβ isoform is presumably not the product of alternative splicing on the mRNA level, but rather from post-translational modification such as proteolytic cleavage, consistent with previous studies [17]. Receptor isoforms, particularly soluble ones, are a conserved element of numerous signaling pathways, including the VEGF-A axis [18-20], often functioning to regulate overabundant ligands and spatial distribution. It is exciting to speculate that this PDGFRβ isoform might also act in this way to modulate pericyte signaling, thereby fine-tuning vessel growth and

maturation in certain contexts. Further studies should be conducted to test this hypothesis by enriching the PDGFRB protein with co-immunnoprecipitation and isolate the resulting bands for analysis by mass spectrometry. Once the results from this are analyzed, recombinant proteins could be developed to test their functionality as a ligand sink in *in vitro* or *ex vivo* models.

The downregulation of *pdgfrβ* was an unexpected finding in our initial data. The next step to investigate this finding was to identify the mechanism that governed the regulation of *pdgfrβ* in pericytes. In Chapter 2, our data identified altered Notch signaling as a downstream consequence of a gain of function for VEGF-A. Research indicates that the Notch pathway has emerged as a convergence point for many signaling pathways, most notably the crosstalk with VEGF-A signaling in endothelial cells phenotype during angiogenesis [19, 21, 22]. Notch cues such as Jagged1 and Notch3 can compromise smooth muscle cell differentiation and investment [23-25]. Pericytes also appear to experience Notch signaling, though the downstream effects of Notch perturbations on pericytes are somewhat unclear, with pericyte *Pdgfrβ* expression and vessel coverage being affected in certain contexts [15, 26, 27] but not others [24, 25, 28, 29]. Our experimental model of embryonic pericytes stimulated by the Notch ligands Dll4 and Jag1 did not up-regulate *pdgfrβ* expression, suggesting that the reduced expression of *pdgfrβ* in pericytes was not directly downstream of the decreased endothelial expression of *Jag1* (as suggested by Jin et al (2008) [26]) in the *Flt1*$^{-/-}$ ESC-derived vessels. In addition, pericyte coverage of ESC-derived vessels was not altered from baseline studies by the addition of the Notch inhibitor DAPT. These observations are consistent with other embryonic vascular development studies in which loss of

Notch signaling did not compromise pericyte PDGFRβ production or pericyte coverage within the microcirculation [24, 25]. Collectively, our data suggest that pericyte *pdgfrβ* expression is Notch-independent in certain contexts. It may be that Notch signaling only plays a role in higher order vasculature with the inclusion of vascular smooth muscle cells. Notch cues such as Jagged1 and Notch show compromised smooth muscle cell differentiation and investment [23-25] in other studies of vessel maturation. Additionally, PDGFRβ activity in the microvasculature may depend on alternate signaling regulation such as through other pathway (e.g. Wnt or Transforming Growth Factor-β (TGFβ)) signaling [30, 31]. Further studies into the mechanism of *pdgfrβ* regulation in the microvasculature are needed to clarify the role of Notch or other pathway convergence in governing pericyte coverage in early developmental context.

To investigate the possible inclusion of other altered pathways in pericyte-endothelial cell interactions, additional transcriptional profiling of candidate molecules was conducted. Of particular note, VEGF-A mis-regulation disrupted synthesis of important extracellular matrix (ECM) components such as Type IV Collagen in our ESC-derived vessel model which may play a critical role in pericyte migration dynamics. Image analysis revealed thickening and dysmorphology in collagen IV over both vessels and pericytes (J.Darden, unpublished data). Other studies of ECM arrays indicated pericytes, from a cell line developed in our lab [32], did not adhere or migrate along collagen IV (H. Zhao, manuscript in preparation) Future studies planned to clarify the relationship of collagen IV in pericyte coverage and migration included the culturing of pericyte cells of multiple models on collagen IV coated plates, as well as the live imaging of pericyte migration on collagen IV arrays. Overall, findings in the disruption of

normal pericyte-endothelial cell interactions via upregulated VEGF-A in an early developmental context lead to the formation and testing of several new hypothesis in pericyte recruitment.

Summary of Chapter 3: InSite: A High Throughput Image Analysis Platform for Resolving Multi-signal Proximity

After investigation of pericyte-endothelial cell dynamics in *in vitro* models, the next logical step was to expand our findings with *in vivo* studies. With this expansion came the need to develop a more robust method of analyzing pericyte interactions on a much larger scale. In Chapter 3, we developed a MATLAB program designed to analyze the colocalization of two signals images via immunostaining, as well as a newly developed measure of proximity that would consider the clearance between cells that were in close association, but were not truly colocalized.

Imaging technologies have rapidly changed since their invention, allowing greater resolution in observing biological specimen on the microscopic level while maintaining spatial relationships between cells and molecules. Confocal and multi-photon imaging systems have evolved to capture high resolution, high magnification images in three dimensions along the X, Y, and Z planes. Newer technologies such as light-sheet fluorescence microscopy also allow for visualization of larger, more complete volumes of tissue (such as heart [33], brain, and entire animal [34]) through digital reconstruction of scanned fields of view. Accumulation of these larger and more complex volumetric renderings generate enormous data files that present several computational challenges

in terms of quantitative analysis [35, 36]. Majority of studies using image quantification compress volumetric data captured in all three dimensions, yielding a 2D image. More specifically, individual “slices” from an image stack are superimposed on each other to yield a maximum intensity projection (MIP). A MIP compression algorithm projects voxel onto the same Z plane in the X-Y visualization field. MIP images are then analyzed manually or via an automated platform using software packages such as ImageJ [20, 37-39]. MIPs for large volumes of light microscopy imaging will likely introduce compression artifacts. In these more comprehensive datasets, signals in discrete and separate Z-planes may appear in close proximity or even colocalized in MIPs, when these signals may in fact be significantly distant from one another. Thus, there is a need to develop computationally inexpensive methods to analyze larger 3D imaging datasets on a slice-by-slice basis to avoid artificially superimposing signals. Commercially available software platforms exist that will analyze volumetric data (e.g. Imaris©); however, in the case of investigating closely associated cells, such as pericyte on endothelial cells, this software is insufficient. Automated software platforms will analyze image colocalization, therefore will not truly capture the association of pericyte coverage of vessels. These options are also monetarily expensive and require intensive user training for confident implementation. In contrast, manually analyzing image stacks using software such as ImageJ introduces bias for thresholding images within and between users. Additionally, to manually analyze images in a slice-by-slice manner to account for volumetric analysis may introduce bias in “forcing” signals to be present when not actually valid resulting in higher variability, as well as being time intensive.

We developed the alternative, largely automated InSite to reduce user variability and bias, and enhances reproducibility by recording the exact threshold value and dilation factor used for each image. InSite uses one threshold value for the entire image for every Z-stack (i.e. no within-image heterogeneity) for consistent and rigorous quantification of colocalization and proximity. Also, this program was designed to present the user with threshold values that “adapts” to the signal-to-noise ratio throughout the entire Z-stack. This information provides a more accurate estimate of the threshold values to use, as well as indicating any changes that occur for each channel. Adjusting threshold values for the deeper Z-stack images (and larger number of slices), InSite employs a depth-based threshold (DBT) to compensate for signal loss with image depth. If the threshold values drop severely at more superficial slices within the Z-range, it will be important for the user consider restructuring and/or reacquiring an image stack so that there will be more confidence in the analysis and accuracy for threshold values applied.

Setting an accurate threshold can be difficult in some types of images due to the manner of acquisition, resulting in high variation within the results that users must be cognizant. There are several reasons for differences in colocalization and proximity in a similar type of image. Common differences in image acquisition settings (e.g. objective magnification, laser power, master gain, signal offset, and Z-range) contribute to variance in threshold values used for analysis. Other factors such as the excitation wavelength used (i.e. 488 nm vs. 568 nm vs. 633 nm) and whether an image was acquired in tile-mode or one single field-of-view also account for variations in threshold values. During program validation, we observed that imaging with the 568 and 633 nm

laser yielded a more robust signal with a more constant intensity through the Z-depth, even in imaging the same cell type but with a different excitation wavelength. Across imaging modalities, end-users will need to consider these details to maximize the output from InSite analysis. It is also imperative that users familiarize themselves with InSite output metrics, as this is vital for more accurate interpretations of the biology from resulting data.

Summary and future directions of Chapter 4: Characterization and Comparisons of Vascular Maturation in Areas of Early Postnatal Mouse Brain

In Chapter 3, we developed a method of rigorous and high throughput manner of analyzing complex multidimensional datasets for expansion of pericyte-vessel interaction studies in normal and upregulated VEGF environments. Previously, our research has shown that alterations in the vascular endothelial growth factor- A (VEGF-A) pathways can impact not only the endothelial cells composing the vessels, but the downstream maturation effects on pericyte and ECM components *in vitro* and *ex vivo* [16]. To further elucidate the effects of altered VEGF signaling *in vivo*, we sought a developmental tissue that naturally exhibited a normal and high growth factor environment simultaneously to characterize the development of the BBB. One such region of the brain is the “germinal matrix” (GM), present in the third trimester of human development [40, 41]. Research has indicated changes in the germinal matrix of human fetus and have been recapitulated in murine models [42, 43], thus marking the GM as

an ideal region to study the altered physiology of the vasculature in high growth factor and simultaneous normal brain regions.

Through the careful analysis of the vessel wall, including vessel morphology, pericyte morphology, astrocyte endfeet, and extracellular matrix component, laminin, our study indicated the slower maturation progression of the microvasculature contrary to reported models. In this study, the data show little differences in vessel morphology between subcortical and periventricular regions at the selected timepoints. P1 sprouting is similar between regions and decreases in both by P7. Vessel length, density, and area remain similar between regions and across timepoints, indicating a lack of dysmorphology contrary to what has been reported. Future studies of exacerbated VEGF signaling could be conducted to further validate or negate these findings by the genetic loss of *flt1*$^{-/-}$ already being studied in murine retinal tissue or genetic upregulation of VEGF-A.

Additionally, pericyte coverage and distribution remained similar in both periventricular and subcortical regions over time, contrary to my original hypothesis of altered pericyte distribution and number. It could be that the rate of growth factor "pushing" for angiogenesis and vessel remodeling/maturation was not high enough to negatively impact the ability of pericytes to migrate in succession with endothelial cells. It is also possible the lack of significant alteration to ECM that was present with Flt-1 loss enabled the other components of the vessel wall to compensate for delayed pericyte migration until such time as pericyte coverage normalized.

In our study, data show a different timeframe for development than previously believed for brain blood vessels. Together our results demonstrate that understanding

how murine vasculature is different from human development, being more structurally stable and potentially resistant to perturbations; as well as, why murine vasculature is resistant to hemorrhage, and other insults to the BBB, is critical to developing advanced treatments for use in human disease and more relevant models to study these effects.

Significance and application of research

While the work shared in this dissertation contributes to the knowledge of pericyte-endothelial cell interaction in altered growth factor environments, it also opens the possibility for new avenues of research. Our results indicating a soluble isoform of pdgfrb could crucial to understanding a new facet of pericyte “fine-tuning” to specific microenvironments and essential to developing targeted therapeutics. Additionally, our finding on the variation of morphology alterations seen *in vitro* and *in vivo* developmental models indicates a discrepancy in murine vascular development that will be key to investigating mechanistically, how this vasculature is different, and why it can be more stable at earlier timepoints than human vascular development. Although murine models have been used for researching therapeutic targets in human diseases, it is exciting to speculate that there is an altered control pathway in mice that allow for the rapid or perhaps, more layered, development of vessels that could have implications in not only vascular disorders, but drug delivery in general.

REFERENCES

1. Whitehead, K.J., M.C. Smith, and D.Y. Li, *Arteriovenous malformations and other vascular malformation syndromes.* Cold Spring Harb Perspect Med, 2013. **3**(2): p. a006635.
2. Leblanc, G.G., et al., *Biology of vascular malformations of the brain.* Stroke, 2009. **40**(12): p. e694-702.
3. Hirschi, K.K., et al., *Gap junction communication mediates transforming growth factor-beta activation and endothelial-induced mural cell differentiation.* Circ Res, 2003. **93**(5): p. 429-37.
4. Paik, J.H., et al., *Sphingosine 1-phosphate receptor regulation of N-cadherin mediates vascular stabilization.* Genes Dev, 2004. **18**(19): p. 2392-403.
5. Hammes, H.P., et al., *Angiopoietin-2 causes pericyte dropout in the normal retina: evidence for involvement in diabetic retinopathy.* Diabetes, 2004. **53**(4): p. 1104-10.
6. Patan, S., *TIE1 and TIE2 receptor tyrosine kinases inversely regulate embryonic angiogenesis by the mechanism of intussusceptive microvascular growth.* Microvasc Res, 1998. **56**(1): p. 1-21.
7. Suri, C., et al., *Requisite role of angiopoietin-1, a ligand for the TIE2 receptor, during embryonic angiogenesis.* Cell, 1996. **87**(7): p. 1171-80.
8. Jeansson, M., et al., *Angiopoietin-1 is essential in mouse vasculature during development and in response to injury.* J Clin Invest, 2011. **121**(6): p. 2278-89.
9. Iivanainen, E., et al., *Angiopoietin-regulated recruitment of vascular smooth muscle cells by endothelial-derived heparin binding EGF-like growth factor.* FASEB J, 2003. **17**(12): p. 1609-21.
10. Benjamin, L.E., I. Hemo, and E. Keshet, *A plasticity window for blood vessel remodelling is defined by pericyte coverage of the preformed endothelial network and is regulated by PDGF-B and VEGF.* Development, 1998. **125**(9): p. 1591-8.
11. Gaengel, K., et al., *Endothelial-mural cell signaling in vascular development and angiogenesis.* Arterioscler Thromb Vasc Biol, 2009. **29**(5): p. 630-8.
12. Hellstrom, M., et al., *Role of PDGF-B and PDGFR-beta in recruitment of vascular smooth muscle cells and pericytes during embryonic blood vessel formation in the mouse.* Development, 1999. **126**(14): p. 3047-55.
13. Abramsson, A., P. Lindblom, and C. Betsholtz, *Endothelial and nonendothelial sources of PDGF-B regulate pericyte recruitment and influence vascular pattern formation in tumors.* J Clin Invest, 2003. **112**(8): p. 1142-51.
14. Lindblom, P., et al., *Endothelial PDGF-B retention is required for proper investment of pericytes in the microvessel wall.* Genes Dev, 2003. **17**(15): p. 1835-40.
15. Kofler, N.M., et al., *Combined deficiency of Notch1 and Notch3 causes pericyte dysfunction, models CADASIL, and results in arteriovenous malformations.* Sci Rep, 2015. **5**: p. 16449.
16. Darden, J., et al., *Excess vascular endothelial growth factor-A disrupts pericyte recruitment during blood vessel formation.* Angiogenesis, 2018.

17. Hutter-Schmid, B. and C. Humpel, *Platelet-derived Growth Factor Receptor-beta is Differentially Regulated in Primary Mouse Pericytes and Brain Slices.* Curr Neurovasc Res, 2016. **13**(2): p. 127-34.
18. Chappell, J.C., et al., *Flt-1 (VEGFR-1) Coordinates Discrete Stages of Blood Vessel Formation.* Cardiovasc Res, 2016. **111**(1): p. 84-93.
19. Chappell, J.C., K.P. Mouillesseaux, and V.L. Bautch, *Flt-1 (vascular endothelial growth factor receptor-1) is essential for the vascular endothelial growth factor-Notch feedback loop during angiogenesis.* Arterioscler Thromb Vasc Biol, 2013. **33**(8): p. 1952-9.
20. Chappell, J.C., et al., *Local guidance of emerging vessel sprouts requires soluble Flt-1.* Dev Cell, 2009. **17**(3): p. 377-86.
21. Jakobsson, L., K. Bentley, and H. Gerhardt, *VEGFRs and Notch: a dynamic collaboration in vascular patterning.* Biochem Soc Trans, 2009. **37**(Pt 6): p. 1233-6.
22. Siekmann, A.F., L. Covassin, and N.D. Lawson, *Modulation of VEGF signalling output by the Notch pathway.* Bioessays, 2008. **30**(4): p. 303-13.
23. High, F.A., et al., *Endothelial expression of the Notch ligand Jagged1 is required for vascular smooth muscle development.* Proc Natl Acad Sci U S A, 2008. **105**(6): p. 1955-9.
24. Henshall, T.L., et al., *Notch3 is necessary for blood vessel integrity in the central nervous system.* Arterioscler Thromb Vasc Biol, 2015. **35**(2): p. 409-20.
25. Volz, K.S., et al., *Pericytes are progenitors for coronary artery smooth muscle.* Elife, 2015. **4**.
26. Jin, S., et al., *Notch signaling regulates platelet-derived growth factor receptor-beta expression in vascular smooth muscle cells.* Circ Res, 2008. **102**(12): p. 1483-91.
27. Wang, Y., et al., *Notch3 establishes brain vascular integrity by regulating pericyte number.* Development, 2014. **141**(2): p. 307-17.
28. Pedrosa, A.R., et al., *Endothelial Jagged1 promotes solid tumor growth through both pro-angiogenic and angiocrine functions.* Oncotarget, 2015. **6**(27): p. 24404-23.
29. Liu, H., S. Kennard, and B. Lilly, *NOTCH3 expression is induced in mural cells through an autoregulatory loop that requires endothelial-expressed JAGGED1.* Circ Res, 2009. **104**(4): p. 466-75.
30. Cohen, E.D., et al., *Wnt signaling regulates smooth muscle precursor development in the mouse lung via a tenascin C/PDGFR pathway.* J Clin Invest, 2009. **119**(9): p. 2538-49.
31. Peng, Y., et al., *Pdgfrb is a direct regulatory target of TGFbeta signaling in atrioventricular cushion mesenchymal cells.* PLoS One, 2017. **12**(4): p. e0175791.
32. Zhao, H., J. Darden, and J.C. Chappell, *Establishment and Characterization of an Embryonic Pericyte Cell Line.* Microcirculation, 2018: p. e12461.
33. Ding, Y., et al., *Light-sheet fluorescence imaging to localize cardiac lineage and protein distribution.* Sci Rep, 2017. **7**: p. 42209.

34. Cai, R., et al., *Panoptic imaging of transparent mice reveals whole-body neuronal projections and skull-meninges connections.* Nat Neurosci, 2019. **22**(2): p. 317-327.
35. Paddock, S.W. and K.W. Eliceiri, *Laser scanning confocal microscopy: history, applications, and related optical sectioning techniques.* Methods Mol Biol, 2014. **1075**: p. 9-47.
36. Nathan S. Claxton, T.J.F., & Michael W. Davidson. *Laser Scanning Confocal Microscopy*. in
. 2005.
37. Kappas, N.C., et al., *The VEGF receptor Flt-1 spatially modulates Flk-1 signaling and blood vessel branching.* J Cell Biol, 2008. **181**(5): p. 847-58.
38. Nesmith, J.E., et al., *Blood vessel anastomosis is spatially regulated by Flt1 during angiogenesis.* Development, 2017. **144**(5): p. 889-896.
39. Rueden, C.T., et al., *ImageJ2: ImageJ for the next generation of scientific image data.* BMC Bioinformatics, 2017. **18**(1): p. 529.
40. Duncan, C.C. and L.R. Ment, *Intraventricular hemorrhage and prematurity.* Neurosurg Clin N Am, 1993. **4**(4): p. 727-34.
41. Whitelaw, A., *Intraventricular haemorrhage and posthaemorrhagic hydrocephalus: pathogenesis, prevention and future interventions.* Semin Neonatol, 2001. **6**(2): p. 135-46.
42. Lekic, T., et al., *Rodent neonatal germinal matrix hemorrhage mimics the human brain injury, neurological consequences, and post-hemorrhagic hydrocephalus.* Exp Neurol, 2012. **236**(1): p. 69-78.
43. James, M.L., D.S. Warner, and D.T. Laskowitz, *Preclinical models of intracerebral hemorrhage: a translational perspective.* Neurocrit Care, 2008. **9**(1): p. 139-52.

APPENDIX: InSite MATLAB Code

Pericyte Coverage Tool

```
%% InSite v1.4 Last modified 1/2019 by Harsh Patolia, Chappell Lab at FBRI

%%InSite is a Matlab tool designed to analyze 3D microscopy data sets
%%acquired on imaging modalities such as confocal and two photon excitation
%%microscopy. The focus of this program is on determining colocalization of
%%red and green voxels while maintaining the three dimensional nature of
%%these data sets. This program provides a computationally intensive
%%analysis of large data sets to determine colocalization and proximity
%%while maintaining ease and minimizcing bias for the user. If you have any
%%questions about the code in this program, please email Harsh Patolia at
%%patohh16@vt.edu.

% PERICYTE_COVERAGE_TOOL MATLAB code for Pericyte_Coverage_Tool.fig
%      PERICYTE_COVERAGE_TOOL, by itself, creates a new
PERICYTE_COVERAGE_TOOL or raises the existing
%      singleton*.
%
%      H = PERICYTE_COVERAGE_TOOL returns the handle to a new
PERICYTE_COVERAGE_TOOL or the handle to
%      the existing singleton*.
%
%      PERICYTE_COVERAGE_TOOL('CALLBACK',hObject,eventData,handles,...)
calls the local
%      function named CALLBACK in PERICYTE_COVERAGE_TOOL.M with the given
input arguments.
%
%      PERICYTE_COVERAGE_TOOL('Property','Value',...) creates a new
PERICYTE_COVERAGE_TOOL or raises the
%      existing singleton*.  Starting from the left, property value pairs are
%      applied to the GUI before Pericyte_Coverage_Tool_OpeningFcn gets called.  An
%      unrecognized property name or invalid value makes property application
%      stop.  All inputs are passed to Pericyte_Coverage_Tool_OpeningFcn via varargin.
%
%      *See GUI Options on GUIDE's Tools menu.  Choose "GUI allows only one
%      instance to run (singleton)".
%
% See also: GUIDE, GUIDATA, GUIHANDLES

% Edit the above text to modify the response to help Pericyte_Coverage_Tool
```

```
% Last Modified by GUIDE v2.5 01-Mar-2018 08:10:44

% Begin initialization code - DO NOT EDIT
gui_Singleton = 1;
gui_State = struct('gui_Name',       mfilename, ...
                   'gui_Singleton',  gui_Singleton, ...
                   'gui_OpeningFcn', @Pericyte_Coverage_Tool_OpeningFcn, ...
                   'gui_OutputFcn',  @Pericyte_Coverage_Tool_OutputFcn, ...
                   'gui_LayoutFcn',  [] , ...
                   'gui_Callback',   []);
if nargin && ischar(varargin{1})
    gui_State.gui_Callback = str2func(varargin{1});
end

if nargout
    [varargout{1:nargout}] = gui_mainfcn(gui_State, varargin{:});
else
    gui_mainfcn(gui_State, varargin{:});
end
% End initialization code - DO NOT EDIT


% --- Executes just before Pericyte_Coverage_Tool is made visible.
function Pericyte_Coverage_Tool_OpeningFcn(hObject, eventdata, handles, varargin)
% This function has no output args, see OutputFcn.
% hObject    handle to figure
% eventdata  reserved - to be defined in a future version of MATLAB
% handles    structure with handles and user data (see GUIDATA)
% varargin   command line arguments to Pericyte_Coverage_Tool (see VARARGIN)

% Choose default command line output for Pericyte_Coverage_Tool
handles.output = hObject;

% Update handles structure
guidata(hObject, handles);

% UIWAIT makes Pericyte_Coverage_Tool wait for user response (see UIRESUME)
% uiwait(handles.figure1);


% --- Outputs from this function are returned to the command line.
function varargout = Pericyte_Coverage_Tool_OutputFcn(hObject, eventdata, handles)
% varargout  cell array for returning output args (see VARARGOUT);
% hObject    handle to figure
% eventdata  reserved - to be defined in a future version of MATLAB
```

```
% handles    structure with handles and user data (see GUIDATA)

% Get default command line output from handles structure
varargout{1} = handles.output;


% --- Executes on button press in pushbutton1.
function pushbutton1_Callback(hObject, eventdata, handles)
% hObject    handle to pushbutton1 (see GCBO)
% eventdata  reserved - to be defined in a future version of MATLAB
% handles    structure with handles and user data (see GUIDATA)

%The handles are passed through the loadimages.m subroutine. Refer to the
%executable file loadimages.m for code and comments.
answer = questdlg('Would you like to run a batch analysis? Please note that ROI
selection is not permitted and analysis parameters are preset and only accessible in the
file "batch_analyze.m."','Select an option to proceed','Yes','No','Yes');
switch answer
    case 'Yes'
        option = 1;
    case 'No'
        option = 2;
end
%The user is asked whether or not they are interested in running a batch
%analysis prior to proceeding.
if option == 2
handles=loadimages(handles);
set(handles.stackslider,'SliderStep',[(1/handles.numberimages)
1/handles.numberimages]);
end

if option == 1
    selpath = uigetdir('Select the folder containing all of the image files you want to
run...');
    handles.batchfilepath=ls(selpath);
    limit = size(handles.batchfilepath,1);
    handles.batchfilepath = handles.batchfilepath(3:limit,:);
    handles.selpath = selpath;
    guidata(hObject, handles);
    handles=batch_analyze(handles);

end
guidata(hObject, handles)


% --- Executes on slider movement.
```

```
function stackslider_Callback(hObject, eventdata, handles)
% hObject    handle to stackslider (see GCBO)
% eventdata  reserved - to be defined in a future version of MATLAB
% handles    structure with handles and user data (see GUIDATA)

% Hints: get(hObject,'Value') returns position of slider
%        get(hObject,'Min') and get(hObject,'Max') to determine range of slider
%% Image Slider for GUI
%Last edited 2/22/2018 by Harsh Patolia
% The slider bar must be discretized to access specific slices of the image
% stack. This is performed by rounding the decimal value of the slider to
% the nearest whole number. If the user selects one of the extremes of the
% slider bar, the value must be forced to be 1 or the maximum number of
% image slices. This prevents errors on the command line.
axes(handles.imagestackaxes);
slidervalue=get(handles.stackslider,'Value');
roundslidervalue = (round(slidervalue/3))*3;
if roundslidervalue == 0
   roundslidervalue = 1;
end
if roundslidervalue > handles.numberimages
   roundslidervalue = handles.numberimages;
end

roundslidervalue_original = roundslidervalue;
imshow(uint16((handles.shownimage(:,:,:,roundslidervalue_original))));
pause(0.1)
guidata(hObject, handles);

% --- Executes during object creation, after setting all properties.
function stackslider_CreateFcn(hObject, eventdata, handles)
% hObject    handle to stackslider (see GCBO)
% eventdata  reserved - to be defined in a future version of MATLAB
% handles    empty - handles not created until after all CreateFcns called

% Hint: slider controls usually have a light gray background.
if isequal(get(hObject,'BackgroundColor'), get(0,'defaultUicontrolBackgroundColor'))
   set(handles.stackslider,'BackgroundColor',[1 0 0]);

   %s = uicontrol('Style','Slider','Min',0,'Max',1,'SliderStep',[0.01 0.10]);
end
guidata(hObject, handles);


% --- Executes on button press in load_single_image.
function load_single_image_Callback(hObject, eventdata, handles)
```

```
% hObject    handle to load_single_image (see GCBO)
% eventdata  reserved - to be defined in a future version of MATLAB
% handles    structure with handles and user data (see GUIDATA)

%DO NOT USE THESE FUNCTIONS THEY ARE NULLED AND NO LONGER
CURRENTLY
%OPERATING
%Lasted edited by Harsh Patolia 2/22/2018

% --- Executes on button press in run_correlation_analysis.
function run_correlation_analysis_Callback(hObject, eventdata, handles)
% hObject    handle to run_correlation_analysis (see GCBO)
% eventdata  reserved - to be defined in a future version of MATLAB
% handles    structure with handles and user data (see GUIDATA)
%DO NOT USE THESE FUNCTIONS THEY ARE NULLED AND NO LONGER
CURRENTLY
%OPERATING
%Lasted edited by Harsh Patolia 2/22/2018

% --- Executes on button press in run_point_analysis.
function run_point_analysis_Callback(hObject, eventdata, handles)
% hObject    handle to run_point_analysis (see GCBO)
% eventdata  reserved - to be defined in a future version of MATLAB
% handles    structure with handles and user data (see GUIDATA)

%DO NOT USE THESE FUNCTIONS THEY ARE NULLED AND NO LONGER
CURRENTLY
%OPERATING
%Lasted edited by Harsh Patolia 2/22/2018

% --- Executes on button press in masking_analysis.
function masking_analysis_Callback(hObject, eventdata, handles)
% hObject    handle to masking_analysis (see GCBO)
% eventdata  reserved - to be defined in a future version of MATLAB
% handles    structure with handles and user data (see GUIDATA)
%% Colocalization/Coverage Analysis
%Last edited by Harsh Patolia 3/2/2018

%This code determines red channel colocalization and proximity over the
%green channel. Colocalization and proximity are distinguished in the sense
%of this program by whether or not the filtered red channel has been
%dilated using the strel command. Colocalization is a measure of the degree
%of overlap of filtered red voxels over filtered green voxels in the native
%image stack. Proximity is a measure of the degree of overlap of dilated
%filtered red voxels (using the strel command) over the filtered green
%voxels (which are specifically not dilated). The red channel is dilated to
```

```
%expand its volume and thus calculate proximity.

clc
set(handles.stackslider2,'Value',1);
set(handles.stackslider2,'Max',handles.numberimages);
set(handles.stackslider2,'Min',1);
set(handles.stackslider2,'SliderStep',[1/handles.numberimages
1/handles.numberimages])

handles.proceed_analysis = 0;
xdimension=size(handles.croppedredimagestack,1);
ydimension=size(handles.croppedredimagestack,2);
depth=handles.numberimages;

%In this block, a thresholding factor is determined as a function of depth
%(in terms of number of slices). This factor accounts for the loss of
%signal intensity with larger depths. The maximum intensity values for the
%red and green image stacks the topmost and bottommost slice are
%determined. The rate of change in brightness intensity (intensity
%gradient) is determined per slice as a line of best fit between these two
%data points. This slope is multiplied by a modification factor (assumed to
%be 0.9 in this code) and utilized in the threshold code as a factor that
%is multiplied by the depth of analysis to generate a depth-dependent
%brightness thresholding value. The underlying assumption here is that
%brightness changes linearly with image depth.
red_max = squeeze(max(max(handles.redimagestack)));
green_max = squeeze(max(max(handles.greenimagestack)));
upper_red_max = max(max(handles.redimagestack(:,:,1)));
lower_red_max = max(max(handles.redimagestack(:,:,depth)));
upper_green_max = max(max(handles.greenimagestack(:,:,1)));
lower_green_max = max(max(handles.greenimagestack(:,:,depth)));
red_modification_factor = 0.9;
green_modification_factor = 0.9;
red_slope =red_modification_factor*((upper_red_max - lower_red_max)/(depth - 1));
green_slope =green_modification_factor *((upper_green_max -
lower_green_max)/(depth - 1));

%A maximum intensity profile is generated by slice number to visualize
%signal loss for the user.
figure(1)
plot((1:depth),red_max,'r',(1:depth),green_max,'g')
title('Maximum Brightness Intensity Profile by Slice')
xlabel('Image Slice Number')
ylabel('Brightness')

handles.binarycroppedredimagestack=zeros(xdimension,ydimension,depth);
```

```
handles.binarycroppedgreenimagestack=zeros(xdimension,ydimension,depth);
redlist=reshape(handles.croppedredimagestack,xdimension*ydimension*depth,1);
greenlist=reshape(handles.croppedgreenimagestack,xdimension*ydimension*depth,1);
handles.shownimage2 = zeros(xdimension,ydimension,3,depth);
guidata(hObject, handles);
%The user can input an 16-bit intensity threshold (as a percentage of 63556
%bits) that serves as a voxel threshold for both red and green channels.
uiwait(msgbox('Modify green and red threshold values on the interface by pressing
"Enter" after they have been typed in. The right panel will update with your selected
threshold values. When the proper threshold values have been selected, please click
"Proceed with analysis". After this message has been read, please click "OK" to
proceed.', 'Warning','warn'))
%The while loop below allows the user to visualize thresholded pixels in a
%real-time fashion. The user is ability to modify the red and green channel
%thresholds and visualize these changes. These thresholds are percentages
%out of the maximum possible intensity.
pause(0.01);
axes(handles.imagestackaxes2);
%The image will be displayed on the second set of axes on the GUI

%This while loop permits the user to be provided live feedback as they
%select red and green intensity thresholds.
while handles.proceed_analysis == 0
pause(.08)
handles=guidata(hObject);
slidervalue2=get(handles.stackslider2,'Value');
roundslidervalue2 = (round(slidervalue2/3))*3;
if roundslidervalue2 == 0
    roundslidervalue2 = 1;
end
if roundslidervalue2 > handles.numberimages
    roundslidervalue2 = handles.numberimages;
end

%% Selection of Thresholds
%This section of the code will generate red and green threshold variables
%based on the user's selection in the prior while loop. Depth-based
%thresholding (DBT) is also implemented in this portion of the code. This
%threshold assumes that loss of signal intensity in the Z-axis is linearly
%dependnet on the depth (in the Z-axis). This mechanism provides the user
%with the ability to automatically filter and account for voxels that may
%be lost to biased intensity-based thresholding that do not consider signal
%loss. Note that the rule in this code assumes that the images acquired are
%16-bit (hence the maximum intensity is 65336). The modification factor
%(red_fudge_factor and green_fudge_factor) is a user adjustable rate of
%change of the adjusted maximum intensity value for each depth, providing
```

```
%the user with the ability to weight the effect of increasing Z-depth on
%the variability of the threshold).
percent_red=str2num(get(handles.red_intensity_threshold,'String'));
red_intensity_threshold=round(((65536-red_slope *
roundslidervalue2)/100)*percent_red,0);
percent_green=str2num(get(handles.green_intensity_threshold,'String'));
green_intensity_threshold=round(((65536-green_slope *
roundslidervalue2)/100)*percent_green,0);
redthreshold=red_intensity_threshold;
greenthreshold=green_intensity_threshold;
showI3 = zeros(xdimension,ydimension);
showI = imbinarize(handles.croppedredimagestack(:,:,roundslidervalue2),redthreshold);
showI2 =
imbinarize(handles.croppedgreenimagestack(:,:,roundslidervalue2),greenthreshold);
rgbImage = cat(3,showI,showI2,showI3);
%An RGB image must be generated from the resulting thresholding procedure,
%and a new image for display is shown.
guidata(hObject, handles);
pause(0.08)
axes(handles.imagestackaxes2);
imshow(uint8(rgbImage*256));
if handles.proceed_analysis == 1
break
end
end
%% Implentation of Selected Thresholds
%Once the user has selected thresholds that are appropriate for their
%analysis, the parameters are implemented in the resulting analysis.
pause(0.1)
percent_red=str2num(get(handles.red_intensity_threshold,'String'));
red_intensity_threshold=round(((65536-red_slope *
roundslidervalue2)/100)*percent_red,0);
percent_green=str2num(get(handles.green_intensity_threshold,'String'));
green_intensity_threshold=round(((65536-green_slope *
roundslidervalue2)/100)*(percent_green),0);
redthreshold=red_intensity_threshold;
greenthreshold=green_intensity_threshold;

%The degree of dilation in the x, y, and z planes is uniform (hence spherical dilation)
and can be
%modified by the user (neighborhoodwidth calls the dilation factor that is
%input by the user).
neighborhoodwidth=get(handles.dilation_factor,'String');
neighborhoodwidth=str2num(neighborhoodwidth);
SE = strel('sphere',neighborhoodwidth) ;
```

```
%RAM space is allocated once again with zero matrices.
matcher=zeros(xdimension,ydimension,depth);
modifymatcher=zeros(xdimension,ydimension,depth);

disp('Masking analysis in progress...')
%Image slices are scanned in a voxel-wise manner to bin pixels that meet
%the intensity threshold criteria in both the red and green channels. If
%the threshold is met, then the voxel is binned in a binary matrix as a 1.
%If the threshold is not met, then the voxel is binned in the binary matrix
%as a 0. Lastly, if there is overlap (colocalization) in the binary red and binary green
%image stacks, then a match is listed in a separate 3D matrix in the
%appropriate coordinate location.
for intk=1:depth
    red_intensity_threshold=round(((65536-red_slope * intk)/100)*percent_red,0);
    green_intensity_threshold=round(((65536-green_slope *
intk)/100)*(percent_green),0);
    I = imbinarize(handles.croppedredimagestack(:,:,intk),red_intensity_threshold);
    I2 = imbinarize(handles.croppedgreenimagestack(:,:,intk),green_intensity_threshold);
    handles.binarycroppedredimagestack(:,:,intk) = I;
    handles.binarycroppedgreenimagestack(:,:,intk) = I2;
end
%The red channel is dilated using the strel routine
handles.modifyred =imdilate(handles.binarycroppedredimagestack, SE);
disp('Dilating image...')
h = waitbar(0, 'Please wait while colocalization and  proximity analysis is completed...');
for inti=1:xdimension
    for intj=1:ydimension
        for intk=1:depth
            %If a thresholded green voxel has the same coordinates as a
            %thresholded red voxel, this is considered a "match".
            if
handles.binarycroppedredimagestack(inti,intj,intk)+handles.binarycroppedgreenimagest
ack(inti,intj,intk)==2
                matcher(inti,intj,intk)=1;
            end
            %The same comparison is performed for the dilated red channel.
            if
handles.modifyred(inti,intj,intk)+handles.binarycroppedgreenimagestack(inti,intj,intk)==2
                modifymatcher(inti,intj,intk)=1;
            end
        end
    end
    waitbar(inti/xdimension)

end
```

```
close(h)

%To visualize the data that was filtered and processed, a new image stack
%is generated that incorporates the dilated pericyte channel (modifyred)
%and the filtered and binarized endothelial cell channel
%(binarycroppedgreenimagestack). This image stack is traversable using the
%GUI slide bar in the Z-dimension (in the same manner as the native image
%stack).
disp('Generating composite RGB images... ');

for intk=1:depth
   rgbImage = cat(3, handles.modifyred(:,:,intk),
handles.binarycroppedgreenimagestack(:,:,intk),showI3);
   handles.shownimage2(:,:,:,intk)=rgbImage;
end
guidata(hObject, handles);
axes(handles.imagestackaxes2);
imshow(uint8(256*handles.shownimage2(:,:,:,1)));
set(handles.stackslider2,'Value',1);
set(handles.stackslider2,'Max',handles.numberimages);
set(handles.stackslider2,'Min',1);
set(handles.stackslider2,'SliderStep',[1/handles.numberimages
1/handles.numberimages]);
%Lastly, the degree of colocalization and proximity is determined by
%calculating the number of overlapping voxels that meet the red and green
%brightness threshold over the total number of green/endothelial voxels
%that meet the green brightness threshold.

%The degree of proximity is determined by calculating the number of
%overalapping red and green thresholded voxels **AFTER** the pericyte
%channel has been dilated (using the user-selected dilation factor) over
%the total number of green/endothelial voxels that meet the brightness
%threshold.

disp('Thinking some more...')
numberofmatches=sum(sum(sum((matcher))));
modifynumberofmatches=sum(sum(sum(modifymatcher)));
%The number of matches using the colocalization and proximty algorithms are
summed.
redtogreen=100*numberofmatches/(sum(sum(sum(handles.binarycroppedgreenimagest
ack))));
greentored=100*numberofmatches/(sum(sum(sum(handles.binarycroppedredimagestac
k))));
modifyredtogreen=100*modifynumberofmatches/(sum(sum(sum(handles.binarycropped
greenimagestack))));
redtogreen_volume=100*numberofmatches/(handles.ROI_area*depth);
```

```
modifyredtogreen_volume=100*modifynumberofmatches/(handles.ROI_area*depth);
%The results of the analysis are exported to an Excel spreadsheet in the
%same folder as the Matlab code entitlted "Slice_analysis.xls). Note that
%each run of this program will overwrite an Excel spreadsheet from a prior
%analysis.
batch_output_slice_by_slice = cell(depth + 1, 3);
batch_output_slice_by_slice(1,1) = cellstr('Slice No.');
batch_output_slice_by_slice(2:depth+1,1) = num2cell(transpose(1:depth));
batch_output_slice_by_slice(1,2) = cellstr('Colocalization');
batch_output_slice_by_slice(1,3) = cellstr('Proximity');

for intk=1:depth
   slice_match(intk,1) =
100*(sum(sum(matcher(:,:,intk)))/sum(sum(handles.binarycroppedgreenimagestack(:,:,i
ntk))));
   slice_modify_match(intk,1) =
100*(sum(sum(modifymatcher(:,:,intk)))/sum(sum(handles.binarycroppedgreenimagesta
ck(:,:,intk))));
end
batch_output_slice_by_slice(2:depth+1,2) = num2cell(slice_match);
batch_output_slice_by_slice(2:depth+1,3) = num2cell(slice_modify_match);
delete('Slice_analysis.xls')
pause(0.2)
msgbox('Slice-by-slice analysis is available in the file named "Slice_analysis.xls" in the
folder containing this Matlab code. After this message has been read, please click "OK"
to close this message box.', 'Your results are ready.','help')
xlswrite('Slice_analysis.xls',batch_output_slice_by_slice);

%The results of this slice analysis are also displayed on the command line
%of the Matlab software.
disp(['The red channel colocalization with the green channel is
',num2str(redtogreen),'%'])
disp(['The dilated red channel proximity with the green channel is
',num2str(modifyredtogreen),'%'])
disp(['The red channel colocalization with green channel (with respect to ROI volume) is
',num2str(redtogreen_volume),'%'])
disp(['The dilated red channel proximity with the green channel (with respect to ROI
volume) is ',num2str(modifyredtogreen_volume),'%'])
guidata(hObject, handles);


% --- Executes on button press in reset_analysis.
function reset_analysis_Callback(hObject, eventdata, handles)
% hObject    handle to reset_analysis (see GCBO)
% eventdata  reserved - to be defined in a future version of MATLAB
% handles    structure with handles and user data (see GUIDATA)
```

```
%% Reset and clear handle variables
%Last edited by Harsh Patolia 2/22/2018
% This command will clear all recyclable handle variables so that a new ROI
% can be selected in the user's atlas image. This removes the need for the
% user to have to close the window and re-import a .tif sequence. Note that
% the native image stack is never deleted from the handles and is always
% maintained, such that imported .tif data is not deleted from the handles.
% Once this button has been clicked, you can perform more image analyses on
% the native image stack (including cell count).
%

clear handles.shownimage
clear handles.croppedyellowimagestack
clear handles.croppedredimagestack
clear handles.croppedgreenimagestack
clear handles.croppednativeimagestack
clear handles.croppedblueimagestack
clear handles.newanalysisimagestack
clear handles.imagestackaxes
clear handles.imagestackaxes2
clear handles.binarycroppedgreenimagestack
clear handles.binarycroppedredimagestack
clear handles.shownimage2
clear handles.matcher
clear handles.modifyred
clear handles.cellcountstack
clear handles.ROI_area
%The image axes are reset so that the native image stack is viewable on the
%GUI again.
handles.shownimage = handles.nativeimagestack;
axes(handles.imagestackaxes);
imshow(uint16(handles.shownimage(:,:,:,1)));
set(handles.stackslider,'Value',1);
set(handles.stackslider,'Max',handles.numberimages);
set(handles.stackslider,'Min',1);
set(handles.stackslider,'SliderStep',[1/handles.numberimages
1/handles.numberimages]);
guidata(hObject, handles);

% --- Executes on button press in runcellcounter.
function runcellcounter_Callback(hObject, eventdata, handles)
% hObject    handle to runcellcounter (see GCBO)
% eventdata  reserved - to be defined in a future version of MATLAB
% handles    structure with handles and user data (see GUIDATA)
%The handles are passed through the loadimages.m subroutine. Refer to the
%executable file cellcount.m for code and comments.
```

```
handles=cellcount(handles);
guidata(hObject, handles)

% --- Executes on button press in select_ROI.
function select_ROI_Callback(hObject, eventdata, handles)
%% Selection of ROI from Atlas Image
%Last edited by Harsh Patolia 3/2/2018

% The function of this command is to permit the user to select a relevant
% ROI in the atlas scan taken of a tissue scan. This features provides the
% program with the ability to accomodate morphological parameters in image
% acquisition and analysis. By using the roipoly command, the user can
% select an ROI in the XY plane and the program will automatically set
% voxels that do not fall within that plane in the Z-axis to 0.

% hObject    handle to select_ROI (see GCBO)
% eventdata  reserved - to be defined in a future version of MATLAB
% handles    structure with handles and user data (see GUIDATA)

slidervalue = get(handles.stackslider, 'Value');
slidervalue = (round(slidervalue/3))*3;
if slidervalue == 0
   slidervalue = 1;
end
handles.slidervalue=slidervalue;
handles.analysisimagestack = handles.nativeimagestack;
R = (handles.analysisimagestack(:,:,:,slidervalue));
axes(handles.imagestackaxes);
imshow(uint16(R))
[R, x_index, y_index] = roipoly(uint16(R));
x_index = round(x_index);
y_index = round(y_index);
imshow(uint16(R))
%The boundaries of the polygonal ROI are recorded as a matrix and referred
%to in the roipoly subroutine below.
for int = 1:handles.numberimages
   for channel = 1:3
      %For each channel, any voxel that does not fall within the range of
      %the selected ROI is forced to 0. This ensures that voxels that are
      %not of interest are not considered in further analyses.
   BW = roipoly(handles.analysisimagestack(:,:,channel,int),x_index,y_index);
   I2 = handles.analysisimagestack(:,:,channel,int);
   I2(~BW)=0;
   handles.analysisimagestack(:,:,channel,int)=I2;
   end
   disp(['Cropping image slice no. ',num2str(int)])
```

```
end
%For comparison to ImageJ, the volume of the ROI is calculated to give the
%amount of coverage over the total ROI volume. This is purely for the sake
%of comparison with ImageJ for performance testing.
I3 = handles.redimagestack(:,:,1);
I3(BW) = 1;
I3(~BW) = 0;
%Any voxels that are not contained within the polygonal ROI are converted
%to an intensity value of 0. Thus, this data is not utilized in further
%analysis. The native image stack, however, can be restored with the
%Resest_analysis subroutine.
handles.ROI_area = sum(sum(I3));
axes(handles.imagestackaxes);
handles.shownimage = handles.analysisimagestack;
imshow(uint16(handles.shownimage(:,:,:,slidervalue)));
%New image stacks are generated to reflect the selected ROIs. The "cropped"
%image is shown subsequently on the GUI.
handles.croppedimagestack = handles.analysisimagestack;
handles.croppedredimagestack = handles.analysisimagestack(:,:,1,:);
handles.croppedgreenimagestack = handles.analysisimagestack(:,:,2,:);
handles.croppedblueimagestack = handles.analysisimagestack(:,:,3,:);
disp(['The selected ROI is
',num2str(100*((handles.ROI_area)/((size(handles.analysisimagestack,1)*size(handles.
analysisimagestack,2))))),'% of the XY area of the image stack.'])
handles.croppedredimagestack = squeeze(handles.croppedredimagestack);
handles.croppedgreenimagestack = squeeze(handles.croppedgreenimagestack);
guidata(hObject, handles);



function dilation_factor_Callback(hObject, eventdata, handles)
% hObject    handle to dilation_factor (see GCBO)
% eventdata  reserved - to be defined in a future version of MATLAB
% handles    structure with handles and user data (see GUIDATA)

% Hints: get(hObject,'String') returns contents of dilation_factor as text
%        str2double(get(hObject,'String')) returns contents of dilation_factor as a double


% --- Executes during object creation, after setting all properties.
function dilation_factor_CreateFcn(hObject, eventdata, handles)
% hObject    handle to dilation_factor (see GCBO)
% eventdata  reserved - to be defined in a future version of MATLAB
% handles    empty - handles not created until after all CreateFcns called

% Hint: edit controls usually have a white background on Windows.
```

```
%       See ISPC and COMPUTER.
if ispc && isequal(get(hObject,'BackgroundColor'),
get(0,'defaultUicontrolBackgroundColor'))
    set(hObject,'BackgroundColor','white');
end


% --- Executes on slider movement.
function stackslider2_Callback(hObject, eventdata, handles)
% hObject    handle to stackslider2 (see GCBO)
% eventdata  reserved - to be defined in a future version of MATLAB
% handles    structure with handles and user data (see GUIDATA)

% Hints: get(hObject,'Value') returns position of slider
%        get(hObject,'Min') and get(hObject,'Max') to determine range of slider
axes(handles.imagestackaxes2);
slidervalue2=get(handles.stackslider2,'Value');
%The slider value must be forced to be a value between 1 and the number of
%image slices. This is a slider that permits the user to traverse the image
%stack in the Z-axis.
roundslidervalue2 = (round(slidervalue2/3))*3;
if roundslidervalue2 == 0
    roundslidervalue2 = 1;
end
if roundslidervalue2 > handles.numberimages
    roundslidervalue2 = handles.numberimages;
end
handles.slidervalue2=roundslidervalue2;
imshow(uint8(256*handles.shownimage2(:,:,:,roundslidervalue2)));
guidata(hObject, handles);


% --- Executes during object creation, after setting all properties.
function stackslider2_CreateFcn(hObject, eventdata, handles)
% hObject    handle to stackslider2 (see GCBO)
% eventdata  reserved - to be defined in a future version of MATLAB
% handles    empty - handles not created until after all CreateFcns called

% Hint: slider controls usually have a light gray background.
if isequal(get(hObject,'BackgroundColor'), get(0,'defaultUicontrolBackgroundColor'))
    set(hObject,'BackgroundColor',[.9 .9 .9]);
end



function red_intensity_threshold_Callback(hObject, eventdata, handles)
```

```
% hObject    handle to red_intensity_threshold (see GCBO)
% eventdata  reserved - to be defined in a future version of MATLAB
% handles    structure with handles and user data (see GUIDATA)

% Hints: get(hObject,'String') returns contents of red_intensity_threshold as text
%        str2double(get(hObject,'String')) returns contents of red_intensity_threshold as a
double
guidata(hObject, handles);


% --- Executes during object creation, after setting all properties.
function red_intensity_threshold_CreateFcn(hObject, eventdata, handles)
% hObject    handle to red_intensity_threshold (see GCBO)
% eventdata  reserved - to be defined in a future version of MATLAB
% handles    empty - handles not created until after all CreateFcns called

% Hint: edit controls usually have a white background on Windows.
%       See ISPC and COMPUTER.
if ispc && isequal(get(hObject,'BackgroundColor'),
get(0,'defaultUicontrolBackgroundColor'))
    set(hObject,'BackgroundColor','white');
end


% --- Executes on selection change in listbox1.
function listbox1_Callback(hObject, eventdata, handles)
% hObject    handle to listbox1 (see GCBO)
% eventdata  reserved - to be defined in a future version of MATLAB
% handles    structure with handles and user data (see GUIDATA)

% Hints: contents = cellstr(get(hObject,'String')) returns listbox1 contents as cell array
%        contents{get(hObject,'Value')} returns selected item from listbox1
guidata(hObject, handles);


% --- Executes during object creation, after setting all properties.
function listbox1_CreateFcn(hObject, eventdata, handles)
% hObject    handle to listbox1 (see GCBO)
% eventdata  reserved - to be defined in a future version of MATLAB
% handles    empty - handles not created until after all CreateFcns called

% Hint: listbox controls usually have a white background on Windows.
%       See ISPC and COMPUTER.
if ispc && isequal(get(hObject,'BackgroundColor'),
get(0,'defaultUicontrolBackgroundColor'))
    set(hObject,'BackgroundColor','white');
```

```
end


function green_intensity_threshold_Callback(hObject, eventdata, handles)
% hObject    handle to green_intensity_threshold (see GCBO)
% eventdata  reserved - to be defined in a future version of MATLAB
% handles    structure with handles and user data (see GUIDATA)

% Hints: get(hObject,'String') returns contents of green_intensity_threshold as text
%        str2double(get(hObject,'String')) returns contents of green_intensity_threshold as
a double
guidata(hObject, handles);


% --- Executes during object creation, after setting all properties.
function green_intensity_threshold_CreateFcn(hObject, eventdata, handles)
% hObject    handle to green_intensity_threshold (see GCBO)
% eventdata  reserved - to be defined in a future version of MATLAB
% handles    empty - handles not created until after all CreateFcns called

% Hint: edit controls usually have a white background on Windows.
%       See ISPC and COMPUTER.
if ispc && isequal(get(hObject,'BackgroundColor'),
get(0,'defaultUicontrolBackgroundColor'))
    set(hObject,'BackgroundColor','white');
end


% --- Executes on button press in proceed_analysis.
function proceed_analysis_Callback(hObject, eventdata, handles)
% hObject    handle to proceed_analysis (see GCBO)
% eventdata  reserved - to be defined in a future version of MATLAB
% handles    structure with handles and user data (see GUIDATA)
handles.proceed_analysis = 1;
pause(0.1);
guidata(hObject, handles);
```

APPENDIX: InSite Code

Importation of Image Stacks into MATLAB

```
%% Importation of Image Stacks Into MATLAB
%Last edited 2/22/2018 by Harsh Patolia

%The function of this executable command is to important .tif sequences
%from a target folder (chosen at the user interface on the GUI). This
%program requires that the imported files are 16 bit .tif files (RGB). If the user
%has imaged a large region of interest (ROI) with multiple image stacks in
%the XY plane, ZEN must be used to stitch the XY images together. The
%composite image stack must then be exported from ZEN as a .tif sequence.
function handles=loadimages(handles)
uiwait(msgbox('Please select the folder containing your stitched image sequence (in
.TIF format). After this message has been read, please click "OK" to proceed.',
'Warning','warn'))
handles.directory = uigetdir(pwd, 'Select a folder with your image sequence'); %Images
are imported from the user-specified directory
h = waitbar(0,'Please wait while images are loaded...');
files=dir(fullfile(handles.directory,'*.tif'));
handles.numberimages=size(files,1);
numberimages=handles.numberimages;
handles.files_cell=struct2cell(files);
sampleimage = imread(char(strcat(handles.directory,'\',handles.files_cell(1,1))));
handles.ximagedimension = size(sampleimage,1);
handles.yimagedimension = size(sampleimage,2);
%Ram is now allocated by generation of 3D zero matrices. This is considered
%best practices for image processing
handles.redimagestack =
zeros(handles.ximagedimension,handles.yimagedimension,numberimages);
handles.greenimagestack =
zeros(handles.ximagedimension,handles.yimagedimension,numberimages);
handles.nativeimagestack =
zeros(handles.ximagedimension,handles.yimagedimension,3,numberimages);
handles.blueimagestack =
zeros(handles.ximagedimension,handles.yimagedimension,numberimages);
%As images are imported, they are filtered via the wiener 2D filter, which
%despeckles images and have been shown to remove noise. This is preliminary
%filter that every image must be processed through. The program will import
%native 16 -bit images.
for int=1:handles.numberimages
    I =imread(char(strcat(handles.directory,'\',handles.files_cell(1,int))));
    %I = uint16(I / 65536);
    handles.nativeimagestack(:,:,:,int) = I(:,:,:);
    handles.redimagestack(:,:,int)=wiener2(I(:,:,1),[5 5]);
```

```
    handles.greenimagestack(:,:,int)=wiener2(I(:,:,2),[5 5]);
    handles.blueimagestack(:,:,int)=wiener2(I(:,:,3),[5 5]);
    disp(['Loading image slice no. ',num2str(int)])
    waitbar(int/(handles.numberimages))
end
%By this point, all of the image files should be fully imported to the
%handle workspace. We can now run our image analysis in 3 dimensions (XY,
%XZ, and YZ)
close(h)
handles.shownimage=handles.nativeimagestack;
axes(handles.imagestackaxes);
imshow(uint16((handles.shownimage(:,:,:,1))))
set(handles.stackslider,'Value',1);
set(handles.stackslider,'Max',handles.numberimages);
set(handles.stackslider,'Min',1);
set(handles.stackslider,'SliderStep',[1 1]);
%The above code will discretize the slider for the user such that bar is
%parametrized for the image stack in question.


end
```

APPENDIX: InSite Code

3D Cell Counting Program

```
%% 3D Cell Counting Program
% Last edited 2/22/2018 by Harsh Patolia

%This function implementats a segmentation analysis of the blue channel
%(which is assumed to be PH3-stained dividing nuclei in our lab). Rather
%than intensity, segmentation of the nuclei are based on continuity after
%image dilation through the implementation of the bwconncomp command. This
%is due to the heterozygous nature of staining of these dividing nuclei. By
%dilating, The heterogenous intensities of stained nuclei can be made
%continuous. Once the nuclei are dilated, the program counts only
%continuous volumes of blue voxels. The threshold for this analysis is 30
%voxels. This means that a volume must take up 30 voxels to be counted as a
%"nucleus." If this size requirement is not met, then the volume is not
%counted and is considered "noise." The value of 30 voxels was chosen
%because based on prior analysis, I found that counts seemed to become
%steady around a given value for cell counts at a threshold of 30 voxels.

function handles=cellcount(handles)
xdimension=size(handles.croppedredimagestack,1);
ydimension=size(handles.croppedredimagestack,2);
depth=handles.numberimages;
handles.binarycroppedblueimagestack=zeros(xdimension,ydimension,depth);
threshold = 60; %THIS IS JORDAN's LINEEEEEEEEEEE FROM HARSSSHH
%The nuclei are dilated in the x and y dimensions for each slice.
%Alternatively, they could be dilated in 3 dimensions using the "sphere"
%subcommand in the strel command
se90 = strel('line', 3, 90);
se0 = strel('line', 3, 0);

for intk=1:depth

    BW2 = bwareaopen(handles.croppedblueimagestack(:,:,intk),threshold);
    BWsdil = imdilate(BW2, [se90 se0]);
    %The cellcountstack contains the dilated pixels for each image slice.
    handles.cellcountstack(:,:,intk) = BWsdil;
end
cellcount1 = bwconncomp(handles.cellcountstack(:,:,:));
cellcount=cellcount1.NumObjects;

%The commented block below can be used to email a notification that the
%program has completed its analysis.
```

```
% mail = '[Insert sending email address here]'; %Your GMail email address
% password = '[Insert password for sending email address here]';  %Your GMail
password
% setpref('Internet','SMTP_Username',mail);
% setpref('Internet','SMTP_Password',password);
% props = java.lang.System.getProperties;
% props.setProperty('mail.smtp.auth','true');
% props.setProperty('mail.smtp.socketFactory.class', 'javax.net.ssl.SSLSocketFactory');
% props.setProperty('mail.smtp.socketFactory.port','465');
% setpref('Internet','SMTP_Server','smtp.gmail.com');
%sendmail('[Insert receiving email address here]','Analysis finished',['The number of
blue cells is ',num2str(cellcount), ' for threshold of ',num2str(threshold)])
%disp(cellcount);
disp(['The cell count for the blue channel is ',num2str(cellcount),' cells',' for a continuity
threshold of ',num2str(threshold), ' voxels.']);
end
%end
```

APPENDIX: InSite Code

Importation of Image Stacks for Batch Analysis

```
%% Importation of Image Stacks Into MATLAB for Batch Analysis
%Last edited 9/30/2018 by Harsh Patolia

%The function of this executable command is to important .tif sequences
%from a target folder (chosen at the user interface on the GUI). This
%program requires that the imported files are .tif files (RGB). If the user
%has imaged a large region of interest (ROI) with multiple image stacks in
%the XY plane, ZEN must be used to stitch the XY images together. The
%composite image stack must then be exported from ZEN as a .tif sequence.
%All images undergo pre-filtering prior to import into Matlab with the
%Wiener despeckling filter. This filter is applied to each image slice.

%Note that this program is only for use for importation of image stacks
%under a specified folder. This feature enables the user to perform a rapid
%batch analysis of multiple image files.

function handles=loadimages_batch(handles)
%Images are imported from the user-specified directory
h = waitbar(0,'Please wait while images are loaded...');
files=dir(fullfile(char(handles.directory),'*.tif'));
handles.numberimages=size(files,1);
numberimages=handles.numberimages;
handles.files_cell=struct2cell(files);
sampleimage = imread(char(strcat(handles.directory,'\',handles.files_cell(1,1))));
%A sample filepath is created and utilized to recursively import images in
%a folder containing the appropriate image sequence.
handles.ximagedimension = size(sampleimage,1);
handles.yimagedimension = size(sampleimage,2);
%Ram is now allocated by generation of 3D zero matrices. This is considered
%best practice for image processing on Matlab.
handles.redimagestack =
zeros(handles.ximagedimension,handles.yimagedimension,numberimages);
handles.greenimagestack =
zeros(handles.ximagedimension,handles.yimagedimension,numberimages);
handles.nativeimagestack =
zeros(handles.ximagedimension,handles.yimagedimension,3,numberimages);
handles.blueimagestack =
zeros(handles.ximagedimension,handles.yimagedimension,numberimages);
%As images are imported, they are filtered via the wiener 2D filter, which
%despeckles images and have been shown to remove noise. This is preliminary
```

```
%filter that every image must be processed through. The program will import
%native 16 -bit images.
for int=1:handles.numberimages
    I =imread(char(strcat(handles.directory,'\',handles.files_cell(1,int))));
    handles.nativeimagestack(:,:,:,int) = I(:,:,:);
    handles.redimagestack(:,:,int)=wiener2(I(:,:,1),[5 5]);
    handles.greenimagestack(:,:,int)=wiener2(I(:,:,2),[5 5]);
    handles.blueimagestack(:,:,int)=wiener2(I(:,:,3),[5 5]);
    disp(['Loading image slice no. ',num2str(int)])
    waitbar(int/(handles.numberimages))
end
%By this point, all of the image files should be fully imported to the
%handle workspace. Image analysis in now performed all 3 dimensions (XY,
%XZ, and YZ). There is no feature in the batch analysis that permits the
%user to tailor a red and green threshold for each image stack in the
%batch. Batch analysis implements standardized thresholds for each
%constituent image stackk.
close(h)
handles.shownimage=handles.nativeimagestack;
axes(handles.imagestackaxes);
imshow(uint16((handles.shownimage(:,:,:,1))))
set(handles.stackslider,'Value',1);
set(handles.stackslider,'Max',handles.numberimages);
set(handles.stackslider,'Min',1);
set(handles.stackslider,'SliderStep',[1 1]);
%The above code will discretize the slider for the user such that bar is
%parametrized for the image stack in question.
end
```

APPENDIX: InSite Code

Batch Analysis of Microscopy Images

```
%% Batch Analysis of Microscopy Images
%Last edited by Harsh Patolia 9/30/2018
%
%This purpose of this subroutine is to perform a rapid high-throughput
%analysis of multiple image files. This feature utilizes the same
%operations as those in the dilation analysis implemented in the Pericyte
%Coverage Tool. Due to the nature of file selection, this feature of the
%program does not provide users with the ability to select an ROI. This
%program also has pre-set parameters for analysis (e.g. dilation
%factor and thresholding for green and red channels).

%Currently the preset values for the analysis are the following: red
%channel threshold = 36 voxels, green channel threshold = 16 voxels,
%dilation factor = 1 voxel).

function handles=batch_analyze(handles)
handles.batchfilepath = cellstr(handles.batchfilepath);
total_number_stacks = size(handles.batchfilepath,1);
batch_output_table = cell(total_number_stacks,8);
Values = inputdlg({'Green Threshold (in percent)','Red Threshold (in percent)','Dilation
factor'},'Select your thresholds for voxel filtering and dilation factor');
Parameter_values = str2double(string(Values));
for int=1:total_number_stacks
    handles.directory = strcat(handles.selpath,'\',handles.batchfilepath(int,:));
    batch_output_table(int+1,1) = handles.directory;
    handles=loadimages_batch(handles);
    handles.proceed_analysis = 0;
    xdimension=size(handles.redimagestack,1);
    ydimension=size(handles.redimagestack,2);
    depth=handles.numberimages;
    total_volume = xdimension * ydimension * depth;
    red_max = squeeze(max(max(handles.redimagestack)));
    green_max = squeeze(max(max(handles.greenimagestack)));
    upper_red_max = max(max(handles.redimagestack(:,:,1)));
    lower_red_max = max(max(handles.redimagestack(:,:,depth)));
    upper_green_max = max(max(handles.greenimagestack(:,:,1)));
    lower_green_max = max(max(handles.greenimagestack(:,:,depth)));
    %The same procedure implemented for depth-based thresholding (DBT) in
    %the slice analysis is utilized in batch analysis. Refer to the slice
    %analysis subroutine in the Pericyte_Coverage_Tool.m file for more
    %information.
```

```
    red_modification_factor = 0.9;
    green_modification_factor = 0.9;
    red_slope =red_modification_factor *((upper_red_max - lower_red_max)/(depth - 1));
    green_slope = green_modification_factor *((upper_green_max -
lower_green_max)/(depth - 1));
    handles.binaryredimagestack=zeros(xdimension,ydimension,depth);
    percent_red=Parameter_values(1); %This is the red channel threshold that the user
selected
    percent_green=Parameter_values(2); %This is the green channel threshold that the
user selected
%Memory is allocated for RAM
handles.binarygreenimagestack=zeros(xdimension,ydimension,depth);
redlist=reshape(handles.redimagestack,xdimension*ydimension*depth,1);
greenlist=reshape(handles.greenimagestack,xdimension*ydimension*depth,1);
pause(.01)
neighborhoodwidth = Parameter_values(3); %This is the automated dilation factor for
the red channel
SE = strel('sphere',neighborhoodwidth) ;
matcher=zeros(xdimension,ydimension,depth);
modifymatcher=zeros(xdimension,ydimension,depth);
disp('Masking analysis in progress...')
%%The specified image stack is binarized based on  depth-based
%%thresholding
for intk=1:depth
    red_intensity_threshold=round(((65536-red_slope * intk)/100)*percent_red,0);
    green_intensity_threshold=round(((65536-green_slope *
intk)/100)*(percent_green),0);
    I = imbinarize(handles.redimagestack(:,:,intk),red_intensity_threshold);
    I2 = imbinarize(handles.greenimagestack(:,:,intk),green_intensity_threshold);
    handles.binaryredimagestack(:,:,intk) = I;
    handles.binarygreenimagestack(:,:,intk) = I2;
end
handles.modifyred =imdilate(handles.binaryredimagestack, SE);
disp('Dilating image...')
h = waitbar(0, 'Please wait while colocalization and  coverage analysis is completed...');
for inti=1:xdimension
    for intj=1:ydimension
        for intk=1:depth
            %If a thresholded green voxel has the same coordinates as a
            %thresholded red voxel, this is considered a "match".
            if
handles.binaryredimagestack(inti,intj,intk)+handles.binarygreenimagestack(inti,intj,intk)=
=2
                matcher(inti,intj,intk)=1;
            end
            %The same comparison is performed for the dilated red channel.
```

```
            if
handles.modifyred(inti,intj,intk)+handles.binarygreenimagestack(inti,intj,intk)==2
                modifymatcher(inti,intj,intk)=1;
            end
        end
    end
    waitbar(inti/xdimension)
end
close(h)
disp('Thinking some more...')
numberofmatches=sum(sum(sum((matcher))));
modifynumberofmatches=sum(sum(sum(modifymatcher)));
redtogreen=100*numberofmatches/(sum(sum(sum(handles.binarygreenimagestack))));
greentored=100*numberofmatches/(sum(sum(sum(handles.binaryredimagestack))));
modifyredtogreen=100*modifynumberofmatches/(sum(sum(sum(handles.binarygreenim
agestack))));
redtogreen_volume=100*numberofmatches/(total_volume);
modifyredtogreen_volume=100*modifynumberofmatches/(total_volume);
for intk=1:depth
    slice_match =
100*(sum(sum(matcher(:,:,intk)))/sum(sum(handles.binarygreenimagestack)));
    slice_modify_match =
100*(sum(sum(modifymatcher(:,:,intk)))/sum(sum(handles.binarygreenimagestack)));
end
%The results of the analysis are dexported to a cell table and are
%organized by each item that was analyzed in the selected batch.
slice_match = squeeze(slice_match);
slice_modify_match = squeeze(slice_modify_match);
disp(['The red channel colocalization of the green channel is(1)
',num2str(redtogreen),'%'])
disp(['The red channel proximity to the green channel is(2)
',num2str(modifyredtogreen),'%'])
disp(['The red channel colocalization of the green channel (with respect to ROI volume)
is(3) ',num2str(redtogreen_volume),'%'])
disp(['The red channel proximity to the green channel is (with respect to ROI volume) is
(4) ',num2str(modifyredtogreen_volume),'%'])
batch_output_table(1,2)= cellstr('Colocalization');
batch_output_table(1,3) = cellstr('Proximity');
batch_output_table(1,4) = cellstr('Colocalization(over ROI volume)');
batch_output_table(1,5) = cellstr('Proximity (over ROI volume)');
batch_output_table(int+1,2) = num2cell (redtogreen);
batch_output_table(int+1,3) = num2cell(modifyredtogreen);
batch_output_table(int+1,4) = num2cell(redtogreen_volume);
batch_output_table(int+1,5) = num2cell(modifyredtogreen_volume);
batch_output_table(1,6) = cellstr('Green Threshold (in %)');
batch_output_table(1,7) = cellstr('Red Threshold (in %)');
```

```
batch_output_table(1,8) = cellstr('Dilation Factor');
batch_output_table(2,6:8) = transpose(Values);
end
disp(batch_output_table)
delete('Analysis_Results.xls')
pause(0.1)
xlswrite('Analysis_Results.xls',batch_output_table);
msgbox('The results of the batch analysis are available in the Excel files "Analysis_Results.xls" in the folder containing the Matlab code for this program. After this message has been read, please click "OK" to close this message box.', 'Your results are ready.','help')
end
```